Effets des radiations de l'environnement spatial sur les mémoires spintroniques

Odilia Coi

▶ To cite this version:

Odilia Coi. Effets des radiations de l'environnement spatial sur les mémoires spintroniques. Micro and nanotechnologies/Microelectronics. Université de Montpellier, 2021. English. NNT : . tel-03772013

HAL Id: tel-03772013
https://hal-lirmm.ccsd.cnrs.fr/tel-03772013

Submitted on 7 Sep 2022

HAL is a multi-disciplinary open access archive for the deposit and dissemination of scientific research documents, whether they are published or not. The documents may come from teaching and research institutions in France or abroad, or from public or private research centers.

L'archive ouverte pluridisciplinaire **HAL**, est destinée au dépôt et à la diffusion de documents scientifiques de niveau recherche, publiés ou non, émanant des établissements d'enseignement et de recherche français ou étrangers, des laboratoires publics ou privés.

THÈSE
Pour obtenir le grade de
Docteur

Délivrée par **Université de Montpellier**

Préparée au sein de l'École doctorale I2S
Et des unités de recherche SPINTEC, CNES, LIRMM

Spécialité : **Systèmes Automatiques et Micro-électronique**

Présentée par : **Odilia Coi**

Effets des radiations de l'environnement spatial sur les mémoires spintroniques

Soutenue le 14 Octobre 2021 devant le jury composé de

Pr. Cristell Maneux, HDR, Université Bordeaux,	Rapporteure
Pr. Jean-Luc Autran, HDR , Université Aix Marseille,	Rapporteur
Pr. Laurent Dusseau, HDR, Université de Montpellier,	Examinateur
Pr. Giorgio Di Natale, HDR, Université Grenoble Alpes,	Examinateur
Mr. David Dangla, Ingénieur, CNES,	Examinateur
Pr. Lionel Torres, Université de Montpellier,	Directeur de Thèse
Dr. Di Pendina Gregory, IR CNRS, SPINTEC,	Co-encadrant
Mr. Robert Ecoffet, Ingénieur, CNES,	Invité
Dr. Nathalie Chatry, TRAD Tests & Radiations Enterprise,	Invitée

UNIVERSITÉ DE MONTPELLIER

Résumé

Depuis l'époque des plus anciennes civilisations, l'espace a toujours été une source inépuisable de d'émerveillement et de curiosité. Aujourd'hui, nous savons que l'environnement spatial représente un énorme défi pour l'espèce humaine. En effet, la présence de différentes sources de rayonnement en fait un endroit rude et dangereux pour l'homme et les appareils électroniques. Néanmoins, l'espace ne peut pas être considéré comme un écosystème indépendant puisque les satellites sont un facteur clé de notre vie quotidienne sur Terre. En pratique, ils permettent non seulement les communications, mais aussi la surveillance de la fonte des glaces, des champs de culture, des ressources naturelles, du changement climatique, de la prévision des tsunamis, etc. En outre, les résultats scientifiques importants des prochaines décennies dépendent fortement des projets de la Station Spatiale Internationale, où des expériences de microgravité sont menées régulièrement.

Au cours des deux dernières années, le regain d'intérêt pour les missions spatiales plus profondes, telles que l'exploration de la Lune et de Mars, a poussé les agences à se pencher sur la question de l'utilisation de l'espace et à investir massivement dans le secteur de la R&D à la recherche de technologies nouvelles et robustes. Cette attention pour le secteur spatial amène certains à rêver que l'espèce humaine devienne une espèce interplanétaire un jour dans le futur, dans des centaines d'années. Ou d'une manière plus prosaïque, elle a suscité l'intérêt du secteur privé et de la commercialisation pour marquer une transition de l'exploration à l'exploitation des ressources naturelles d'autres planètes, ou simplement pour faire du tourisme spatial. Bien qu'une réflexion éthique sur ce sujet représente un défi fascinant, dans ce travail scientifique nous cherchons à repousser les limites des moyens technologiques qui pourraient faire de certains de ces scénarios une réalité. En particulier, l'électronique traditionnelle étant basée sur le stockage de charges, elle est susceptible d'expérimenter de nombreux effets néfastes dans l'espace. C'est pour cette raison que des dispositifs non basés sur la charge ont fait l'objet de recherches intensives au cours de la dernière décennie, au point que la première génération de mémoires magnétiques ("FIMS-Toggle") a été embarquée sur le Rover Persévérance, qui a atterri avec succès sur Mars le 18 février 2021 afin de ramener sur Terre des échantillons de roche martienne. Orienté vers l'avenir, ce travail vise à contribuer à l'étude des effets de l'irradiation spatiale sur les dispositifs spintroniques de dernière génération. Le travail est organisé comme suit : le premier chapitre donne un aperçu des différentes familles de mémoires non volatiles émergentes, en soulignant les avantages et les inconvénients de chacune d'entre elles. Dans le deuxième chapitre, nous décrivons en détail l'environnement spatial, ses sources de radiation et les effets qu'elles ont sur les systèmes de communication et l'électronique associée.

Dans le troisième chapitre, nous explorons comment les dispositives spintroniques peuvent être utilisés au niveau de la conception du circuit pour améliorer la tolérance aux rayonnements. Dans le quatrième chapitre, nous réalisons une étude détaillée de l'effet des ions lourds sur les dispositifs à couplage de transfert de spin, tant d'un point de vue théorique qu'expérimental. En particulier, le rôle du pic thermique dans le mécanisme de défaillance est pris en compte pour la première fois. Ce chapitre représente une contribution importante à l'état de l'art, puisque les mécanismes de base dans de tels dispositifs n'ont pas encore été étudiés.

Dans le dernier chapitre, nous avons irradié la même famille de dispositifs avec des protons et nous avons également exposé à ce rayonnement la dernière technologie spintronique, pas encore commercialisée, le Spin-Orbit. Ces derniers représentent les premiers résultats sur ces dispositifs.

Summary

Since the time of the most ancient civilisations, space has always been an endless source of wonder and curiosity. Today, we know that space environment represents a huge challenge for human kind. Indeed, the presence of different radiation sources render it a rough and dangerous place for human and electronics devices. Nevertheless, Space could not be considered as an independent ecosystem since Satellite are key factor of our daily life on Earth. In practice, they allow not only communications, but also the monitoring of ice melt, crop field, natural resource exploitation, climate change, tsunami prediction and so on. Moreover, important next decade scientific results, heavily rely on International Space Station projects where micro-gravity experiments are restlessly carried out.

In the last couple of years, the renovate interest for deeper space missions such as Lunar and Mars exploration have driven agencies into a huge investment in the R&D sector looking for new, robust, technology. This attention for the space sector made somebody dreaming the human kind to become an interplanetary species one day in the future, hundreds of years from now. Or in a more prosaic way, it has sparked the interest of private sector and commercialization to mark a transition from exploration to exploitation of other planets natural resources; or simply to make money with space tourism. Although an ethical reflection on this topic represents a fascinating challenge, in this scientific work we aim to push the boundaries of technological means which could made some of these scenarios a reality. In particular, as traditional electronics is based on charge storage it is prone to experiment many harmful effects in Space. For this motivation non-charge based devices have been intensively investigated in the last decade, to the point that the first generation of Magnetic Memories (FIMS-Toggle) have been embedded on the Perseverance Rover, successfully landed on Mars on February 18th 2021 to carry back on Earth sample of Martian rock and regolith in ten years from now. Oriented towards the future, this work aims to contribute to the study of space irradiation effects on the last generation of spintronic devices.

The work is organized as follows: first chapter gives an overview on the different families of Emerging Non Volatile Memories highlighting the advantages and drawbacks in the use of each. In the second chapter we depict in detail the space environment, its radiation sources and the effects that they have on electronics. In chapter three we explore how spintronic devices could be used at design/circuit level to enhance the tolerance against irradiation. In the fourth chapter we conduct a detailed study on heavy ion effect on Spin-Transfer Torque devices both from a theoretical and experimental point of view. In particular the role of thermal spike in the failure mechanism is for the first time taken into

account. This chapter represents an important contribution to the state of the art, since basic mechanisms in such a device were not yet studied. In the last chapter we irradiated the same family of devices with proton and also, we exposed to this radiation the latest spintronic technology, not yet commercialized, the Spin-Orbit Torque Magnetic Tunnel Junction. The latter represents the first result on these devices.

Remerciements

The author would like to thank all people who made possible this research work; they are not all listed here, though.
First of all, thanks to Pr. Lionel Torres, my Ph.D. director, for his trust, guidance, support and patience since 2016, when I was still a master student. Thanks for valorising my interdisciplinary background, and thanks for the fruitful discussions we had about science and philosophy. Thanks for the time he dedicated in reviewing my papers during the first year, and teaching me how to write my first one in 2016. Thanks for the brainstorming and the wonderful time I spent at LIRMM; I treasured it. Thanks to LIRMM, which founded all my missions during this Ph.D.
Then, I would like to thank the CNES and SPINTEC, which both funded this thesis and thus have made this research possible. Thanks to SPINETC for hosting me during these three years, thanks to Gregory Di Pendina for overseeing this PhD. Thanks to Bernard Deny and Kevin Garello for the fruitful scientific discussion.
A special thank to the my supervisor at the CNES, David Dangla who funded all the irradiation experiments. Thanks for his smile and for showing that seriousness and sadness are not the same things.
This work could hot have been possible without the support that I received from Robert Ecoffet. Thanks for organising the first meeting with TRAD and for pushing everybody to have some experimental results in this work, as per my objective too. Thanks also for the invaluable time he spent to train me on Space environment and radiation effects at CNES; I treasured these memories. Thanks for his creativity, advice, support, his patience and humanity.
Thanks to TRAD Company for letting me use their tool. Thanks to dr. Nomena Adrianjohany for the endless calls we had during the Covid lockdown, after his normal work-time, trying to solve multiple issues in the simulation framework.
Thanks to the RADECS association for sharing his knowledge, humanity, and enthusiasm, particularly thanks to Philippe Paillet.
Many thanks to the Jury committee for the fruitful discussions during my PhD defence and their time to review this work. I was delighted to hear they felt this work was worth continuing.
Ad astra per aspera.

Contents

Introduction **1**

1 Emerging Non-Volatile Memories **4**

1.1 Introduction 4
1.2 Ferroelectric Memories 6
1.3 Resistive Memories 7
1.4 Phase change Memories 7
1.5 Magnetic Memories 8
1.5.1 Field Induced Magnetic Switching Toggle 11
1.5.2 Thermally Assisted Switching 13
1.5.3 Spin-Transfer Torque 14
1.5.4 Spin-Orbit Torque 21
1.6 Conclusion 23

2 Space environment **26**

2.1 Introduction 26
2.2 Solar event and solar particles 27
2.3 Radiation Belt 29
2.4 Trapped protons 30
2.5 Trapped Electrons 31
2.6 Galactic Cosmic Rays 31
2.7 Neutrons 32
2.8 The effect on electronics 32
2.8.1 Total Ionozing Dose 32
2.8.2 Single Event Effect 33
2.8.3 Displacement Damages and Non Ionizing Energy Loss 35
2.9 Means of prevention from radiation effects 38
2.10 Irradiation Testing and testing simulator 39
2.10.1 CubeSat 39
2.10.2 Irradiation facilities 40
2.10.3 Irradiation simulation 41
2.10.3.1 Stop and Range of Ions in Matter (SRIM) Software 41
2.10.3.2 OMERE 42
2.10.3.3 FASTRAD 42

2.10.3.4 TRADCARE® 43
2.11 Conclusion 44

3 Radiation Hardening by Design 46
3.1 Introduction 46
3.2 FDSOI 47
3.3 Error model using Cadence Virtuoso 48
3.3.1 Critical charge: considerations on MOSFET parameters dependence 49
3.4 C-element 50
3.5 Proposed Novel Circuit 53
3.5.1 Robustness evaluation 54
3.5.2 Radiation hardening enhancement 57
3.5.2.1 Impact of MTJ parameters on radiation hardening 57
3.5.2.2 Impact of the shunt path on radiation hardening 61
3.5.3 Performance evaluation 64
3.5.4 Asynchronous micropipeline 65
3.6 An SOT-STT hybrid model for error electrical injection 66
3.6.1 SOT NV C-element implementation 66
3.6.2 SOT proposed model 68
3.6.3 SOT robustness evaluation 70
3.6.3.1 Influence of the SOT channel parameters 70
3.6.3.2 Influence of the MTJ resistance 70
3.7 Conclusion 71

4 Heavy ion irradiation effects 73
4.1 Introduction 73
4.2 Critical parameters and basic mechanisms 74
4.2.1 Tradcare® Simulation 75
4.2.2 Single Event Effects originates in CoFeB 78
4.2.2.1 Spin-Transfer Torque Switching 78
4.2.2.2 Thermal Switching 80
4.2.3 Transient thermal Events 84
4.2.3.1 Magnetic properties degradation 84
4.2.3.2 Thermal stability and Retention time of the stored information 86
4.2.4 Permanent thermal effects 88
4.2.4.1 H_C degradation and the role of Synthetic Antiferromagnetic layer 88
4.2.4.2 Curie Temperature overtaking: Thermal Event Upset . . . 89
4.2.4.3 MgO Tunnel Barrier 91

4.3 Dynamic Irradiation Experiment . . . 92
4.3.1 Device Under Test . . . 93
4.3.2 Irradiation campaign set-up . . . 95
4.3.2.1 PCB and adaptation cards . . . 96
4.4 Static Irradiation Experiment . . . 98
4.5 Irradiation campaign . . . 100
4.5.1 Analysis of Heavy ion irradiation effects . . . 102
4.5.2 Test of read operation . . . 102
4.5.3 Test of Write operation . . . 104
4.5.4 Annealing of the reference circuit (control-group) . . . 107
4.6 Conclusion . . . 109

5 Proton irradiation effects **111**
5.1 Introduction . . . 111
5.2 Device under test . . . 111
5.3 Experimental result . . . 114
5.4 Machine Learning . . . 120
5.5 Conclusion . . . 124

6 Conclusion and perspectives **125**

Bibliography **126**

A Publications **140**

Introduction

When chances of solving a problem seem to be exhausted, a solution can be sought by changing the paradigm.

Since the advent of the first integrated circuits in the 1970s, integrated circuits have been based on the electrical charge of electrons to store the binary information. As the scaling reached unimaginable sizes, today this charge is often less than a femto Coulomb, namely less than a few thousand electrons. In constrained environments such as space or nuclear, radiation sensitivity is critical and circuits must be designed specifically for these environments. Indeed, the interaction of a single high-energy particle with a transistor can be enough to severely disrupt information, leading to failures. Indeed, a high-energy charged particle passing through a semiconductor material is likely to inject hundreds of electrons inducing perturbations of the charge quantity, large enough to create errors or even destroy electronic components.

After years of studies on the properties of ferromagnetic materials, which change their resistivity according to the orientation of the magnetic domains, we have seen the birth of spintronics, exploiting both the electrical and magnetic properties of the electron (Nobel Prize winners Albert Fert and Peter Grünberg). Today, the magnetic tunnel junction (MTJ) is a memory element made up of two layers of ferromagnetic material (CoFeB) separated by an insulating layer (MgO). The latter allows a current to pass from one layer to the other leveraging the tunnel effect. The storage of bit "1" and "0 " is achieved thanks to the mutual orientation of the spin (and no longer of the charge) in these two ferromagnetic alloy layers, allowing a parallel (0) or antiparallel (1) configuration. Once the bit is programmed, it is no longer necessary for the device to be connected to a power source to maintain the data: the information is therefore stored in a non-volatile manner. Several layers of different materials (Pl, Ru, Ta, Co...) are added to the ferromagnetic layers of the MTJ during its manufacture to increase the efficiency of the physical and quantum mechanisms it implements during its operation. The typical dimensions of an MTJ are around 30 nm in height and between 150 and 20 nm in diameter. By their nature, these devices have gained much interest due to their low power consumption. Moreover, they are excellent candidates for the realisation of hardened electronic circuits because they are not, a priori, sensitive to the charge variations induced by radiation.

To give scientific value to these intuitions, the Centre Nationale d'Études Spatiales (CNES) in Toulouse, the CNRS-CEA-UGA SPINTEC laboratory in Grenoble and the Laboratoire d'Informatique, de Robotique et de Microélectronique de Montpellier (LIRMM, UMR CNRS-UM) have founded this PhD research. Among the emerging spintronic tech-

nologies, the perpendicular anisotropy MTJ is the most promising form because of its easy miniaturisation (in diameter), an essential condition to satisfy the demand for high density memories. This study will allow us to enrich the literature in this field, which has not yet been exploited: these results will guide the industry in the near future. The project is organised in four fundamental points: a study at electrical/design level on the errors induced by CMOS transistors on the MTJ in hybrid circuits under irradiation; a study of the basic-mechanism induced by irradiation on the MTJ; the implementation of two test campaigns concerning the irradiation of different spintronic arrays: the first by means of heavy ion and the second by means of protons, both of them took place at the Synchrotron of the Catholic University of Louvain (UCL). An important part of this research is also dedicated to the analysis, interpretation and representation of the results and conclusions obtained from these studies.

In order to give a general background, the first and second chapters detail an overview on emerging non volatile technology and space environment, respectively.

The third chapter approaches the problem from an electrical point of view to determine under which conditions the transistors adjacent to the MTJs can be the source of the errors. In this framework, after an initial analysis, an innovative circuit design was proposed using 28 nm FDSOI technology provided by ST Microelectronics and 40 nm MTJ junctions. The originality of this circuit lies in the creation of an alternative path by the current induced by the errors during radiation, thus avoiding rewriting or breakdown of the junctions. Moreover a Spin Orbit Torque (SOT)-Spin Transfer Torque (STT) hybrid model was developed. This is an essential point in order to evaluate the switching probability of SOT devices under electrical fault injection.

In the fourth chapter theoretical study is conducted on basic mechanism which could be induced by the irradiation of MTJs. Several possible effects of irradiation on MTJs can be envisaged: localized defects and electric charge accumulation leading to electrostatic breakdown (ESD) of the barrier; structural changes at the ferromagnetic-insulator interface. To evaluate these effects, we used a dedicated tool, TRADCARE® provided in collaboration with the company TRAD. The detailed knowledge of the MTJ stack (order, thickness, density of the layers in the stack and their resistivity at the interfaces) was crucial for the construction of a physical and electrical model of the Junction. Then we dedicated to the preparation of the circuit irradiation campaigns. This work involved many technical tasks such as the definition of the wire bonding plan, the choice of packaging, the definition of the signals needed to write and read the MTJs and the design of two boards to drive them. To make all this possible, a rich exchange of information with colleagues from CNES and UCL was necessary. Part of the research concerned the interpretation of the simulation results, the consideration of the experimental aspects and the correlation with theoretical fundamentals. This is a crucial step in understanding and representing the radiation sensitivity of this technology and which led to study the

temperature's role in the MTJ failure mechanism. As the first irradiation campaign took place in July 2020, heavy ion irradiation result on STT devices are presented to conclude this chapter.

In the last chapter, we present proton irradiation result from the second experimental campaign, which took place at UCL in November 2020. SOT and STT parameters are largely analyzed and compared when possible. We also suggest the use of machine learning technique (on huge data-set) to predict parameter evolution after irradiation in order to optimize time and cost of the irradiation campaign.

Chapter 1

Emerging Non-Volatile Memories

1.1 Introduction

On April 1965, Gordon Moore, one of the founder of Intel, wrote an article on Electronics Magazine [90] where he made a prediction based on extrapolation from a few point graph: the price of integrated circuit will be halved each year while the processor performance would be doubled. Since then, the techno-economic model that has enabled the information technology industry to double the performance of electronics every 2 years within a fixed cost, was popularly known as Moore's law. The prediction, proven correct in 1975, had the incredible power to shape the trajectory of technology of the past 50 years, since designers and chip industry all around the word made the impossible to meet the "Moore Low" requirements, thus making possible the technological development as we know it.

The International Technology Roadmap for Semiconductors (ITRS) has been updated nearly every year since the first version in 1998. However the one titled ITRS 2.0 2015 Edition was the last one that has been published [1]. Indeed, in this one, they predicted the end of the Moore's Law by 2021 with a reached limited transistor size of 10 to 7 nm as depicted in Fig. 1.

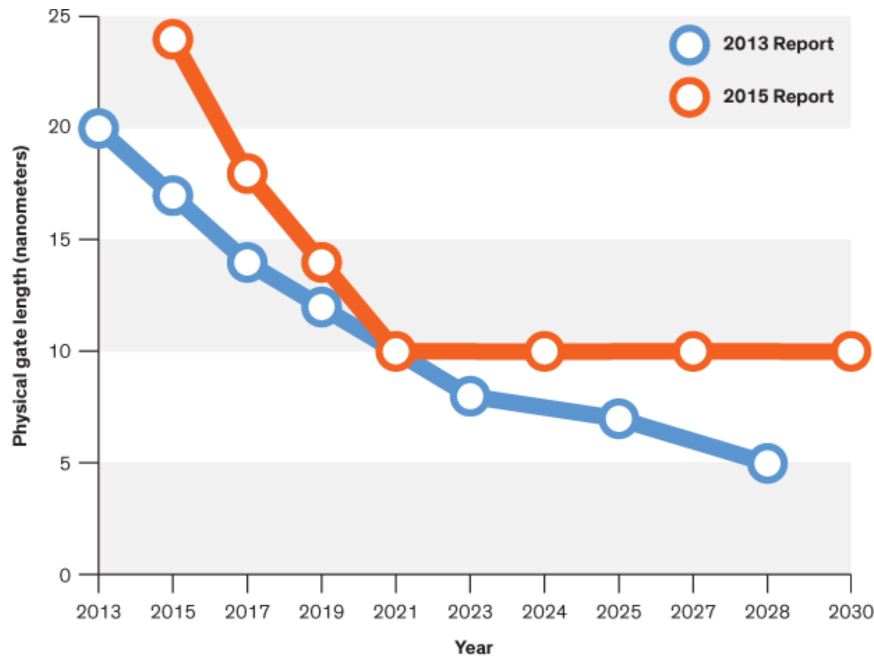

Figure 1: ITRS had previously predicted that the physical gate length of transistors would shrink until at least 2028. The last ITRS report predict this feature to be flat by 2021 [1].

Faced with ever-evolving research needs and technology challenges, industry leaders have decided to conclude the ITRS and transition to new ways to advance semiconductor research and bring about the next generation of semiconductor. Thence, more and more efforts in new transistor technology development have to be done by industry and academia. In particular, as memories remain the bottleneck of computer performance, new paradigms were investigated to stay in the power budget while achieving high performance. The expression " beyond Moore technology", is referred to unconventional electronics studies which explore atom's state variable other than electron charge to store the information as Magnetic Random Access Memory does. These devices belong to the wider family of Emerging Non-volatile memories. Fig. 2 shows the different technologies which we will review in the following sections.

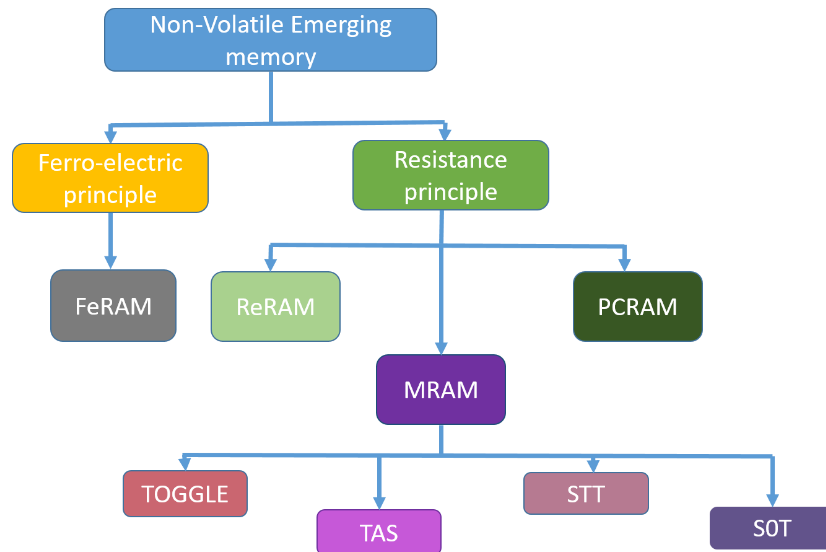

Figure 2: Representation of the different Non-Volatile Emerging memories.

1.2 Ferroelectric Memories

Ferroelectricity is known to arise from two stable polarization states that can be sustained in the absence of an applied electric field, and such spontaneous polarization can be produced by various arrangements of ions in the crystal structure of the material. The characteristic of symmetry-breaking distortion enables ferroelectric materials to ensure the presence of discrete states and, therefore, enhance the possibility of polarization switching between the states by applied electric field [34]. Indeed, ferro-electric materials consist of crystals that exhibit spontaneous polarization; they can be in one of two states, which can be reversed with a suitable electric field. For this reason, Ferroelcetric memory (FeRAM) uses a ferroelectric capacitor architecture that employs ferroelectric materials as storage elements [47]. Switching the ferroelectric polarization states requires the movement of the dipole located within an oxygen octahedron in response to an electric field. This movement can be impeded by a free electric charge or other ionic defects built-up over time and temperature. Such effects cause the dipoles to relax over time leading to fatigue and failure.

The research using ferroelectrics dates back to the 1950s with the first commercial memories coming to market in the early 1990s. However, the severe challenges of perovskite ferroelectric materias into a CMOS process and the fact that the reading operation are destructive lead to market disadvantages of FeRAM which also show storage capacity limitations and high cost. The recent discovery of a ferro-electric phase in HfO_2, a well-known and less complex material, has triggered a renewed interest in this memory concept. Indeed, unlike the conventional ferroelectrics based on the perovskite-type crystal structure, of which ferroelectric properties degrade at the thickness smaller than $\sim$

100 nm, the FE-HfO_2 thin films can exhibit excellent ferroelectric properties at extremely low thicknesses of $\sim$ 10 nm [97].

1.3 Resistive Memories

Resitive memories (ReRAM) technologies are based on a Metal/Insulator/Metal (MIM) structure: two metallic electrodes separeted by a thin resistive layer. By applying a voltage between these electrodes, a conductive path, called filament, is formed. This way, current is allowed to flow and leading to a low resistive state. This phenomenon can be reversed by applying another voltage drop on the cell, thence coming back to a high resistive state. Depending on the top electrode nature, this filament can be composed of various element leading to distinguish 2 type of ReRAM technology: Oxide RAM (OxRAM) and Conductive Bridge RAM (CBRAM). In CBRAM, filament is composed of metal ions coming from the top electrode. In OxRAM technology, filament is composed of oxygen vacancies created in the oxide resistive layer. They are both suffering from conductance variability and non-linear change of conductance upon identical programming pulses [10]. There are many small companies working to commercialize this technology, such as Crossbar and Weebit Nano, and there's also a lot of research work being done at LETI, a technology research institute of CEA Tech based in France.

1.4 Phase change Memories

The research activity on the operating principle of the Phase Change Memory (PCM) and its optimization find its roots in the original work by Ovshinsky, dated back in the late 1960s, discovering the existence of reversible switching effects of chalcogenide alloys [14]. In particular, he found that some chalcogenide-based glasses presented rapid and reversible transitions between a highly resistive and conductive state effected by an electric field and that, some of them, showed an unusual memory effect. Phase-Change Memory (PCM) is a non-volatile solid-state memory technology built around this large electrical contrast between the highly-resistive amorphous and highly-conductive crystalline states in the so-called phase change materials [59]. To SET the cell into its low-resistance state, an electrical pulse is applied to heat a significant portion of the cell above the crystallization temperature of the phase change material. This SET operation tends to dictate the write speed performance of PCM technology, since the required duration of this pulse depends on the crystallization speed of the phase change material. In the RESET operation, a larger electrical current is applied in order to melt the central portion of the cell. The described operation principle is depicted in Fig. 3. Since the RESET operation tends to be fairly power–hungry, the choice of an access device capable of delivering high current without requiring a significantly larger footprint than the PCM element remain the main

challenge. The read operation is performed by measuring the device resistance at low voltage, so that the device state is not perturbed.

This memory is considered today as the most mature and promising resistive memory technology, as demonstrated by recent commercialization for Storage Class Memory market, because of scalability and proven reliability of 3 D cross point architecture [16].

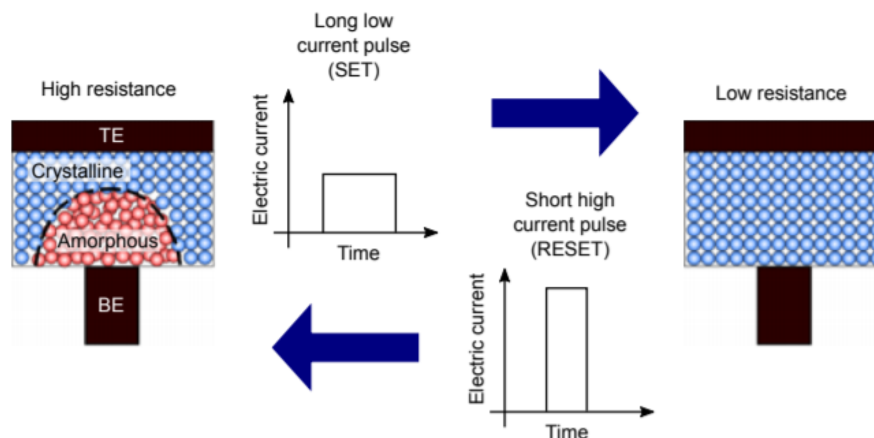

Figure 3: Operation principle of PCRAM. A long low current pulse (SET) is applied to bring the PCM device to the low-resistance crystalline state. A short high current pulse (RESET) is applied to bring the PCM device to the high-resistance amorphous state [36]

1.5 Magnetic Memories

Nanomagnetic systems provide unique opportunities to continuous advances in device performance and storage capacities since they are inherently non-volatile due to the magnetic order properties. Indeed, Magnetic Memories (MRAM) is a memory that uses the magnetism of electron spin to provide non-volatility, high endurance and near zero leakage. Actually, the magnetic polarization does not leak away with time like charge does, so the information is stored even when the power is turned off. MRAM stores information in a nano magnetic element, the Magnetic Tunnel Junction, which is integrated with silicon circuitry to deliver roughly the speed of SRAM with the non-volatility of Flash in a quasi-single unlimited-endurance device (10^{14} write cycle at 1 V).

The Magnetic Tunnel Junction (MTJ) is the basic element of every MRAM techonology. Present spintronic devices are complex hetero-structures that combine many layers of different materials, however, it is possible to group the MTJ multi-layer by their functionality as follows:

- a thin insulating barrier (usually Magnesium Oxide, MgO), which makes the passage of current possible by leveraging Tunnel Effect. The latter is based on the fact that the electron is a quantum particle and also behaves like a wave. If the wall is very thin, the wavefunction can propagate through the potential barrier. For these

motivation the thickness of the barrier ranges between 0.7 nm and 1.4 nm [50]. Moreover, particular importance is given to the crystallinity of the MgO in order to guarantee a coherent tunnel of the electrons.

- a ferromagnetic layer, called reference layer (RL) which, by construction has a pinned magnetization. Usually, it is made of CoFeB alloy due to the ferromagnetic properties of these materials and it has a thickness around 1.8 nm. To fix the magnetization direction in the reference electrode, an increase in thickness (volume) compared with the free layer can be used to achieve a higher stability of the magnetization. In practice, the pinning of the reference electrode is achieved through its coupling with a neighboring antiferromagnetic layer. The strength of this coupling is chosen to be much higher than the energy needed for the "free" layer to switch, allowing for an independent manipulation of the magnetic state of the free layer without perturbing the alignment of the pinned layer [78].

- a ferromagnetic layer, called free layer (FL) with a switchable magnetization. In a typical structure, its thickness varying between 1.1 nm and 1.4 nm made with the same RL materials.

Depending on the mutual orientation of the RL and FL (parallel or anti-parallel) the resistance changes being either low state (R_p) or high state (R_{ap}). Bit "0" or "1" are consequently stored. Indeed, the resistance of the MTJ cell depends on this relative magnetization alignment: as a result of the Tunnel Magnetoresistance (TMR) effect for ferromagnetic materials, R_{AP} will always be higher than R_P. By indicating with θ the angle between the reference and storage layer polarizations and with ΔR the resistance variations from antiparallel to parallel state, we can quantify the MTJ resistance as follow:

$$R(\theta) = R_p + \Delta R \frac{(1 - cos(\theta))}{2} \tag{1.1}$$

So that, it is easy to verify that in the parallel configuration θ=0 thus R=R_p, while in the antiparallel configuration $\theta = 180$ thence R=R_p+ΔR. The TMR gives a metric of the MTJ readability and it is expressed as [77]:

$$TMR = \frac{\Delta R}{R_p} = \frac{R_{ap} - R_p}{R_p} \tag{1.2}$$

The TMR effect was first discovered in 1970, but it was only 5 years later that Julliere observed this phenomenon at low temperature (300 K) allowing the development of these devices.

It is worth to underline that the ferromagnetic behaviour is guarantee only below a certain temperature, called Curie temperature (T_c). Over this limit the material has a transition to the paramegnetic state, where the magnetization has any preferred ori-

entation (disordered state). The Curie temperature, specific for each material, strongly depends on the thickness of the considered layer. More precisely, we can distinguish between blocking (T_b) and Curie temperature according to the following definition: below the blocking temperature, there is some net alignment of the particle spins, while above it, the spins are in random directions; below the Curie temperature, there is some net alignment of the atomic spins within a particle, while above it, they are randomized [83]. This is illustrated in Fig. 4.

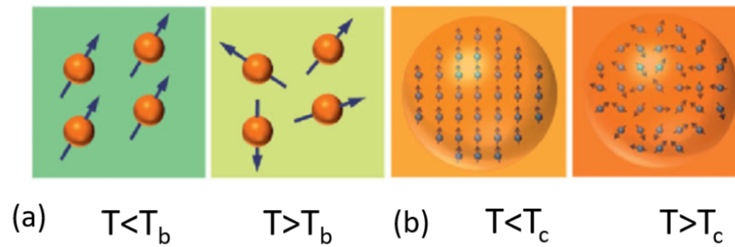

Figure 4: Particles' and atom's spin, below and above the threshold temperature of the paramagnetic transition [83].

The magnetization dynamic is describe by an hysteresis loop. The hysteresis loop of the FL is illustrated in Fig. 5 (a), where the coercive field (H_c) represents the field value needed to switch the magnetization from one stable state to the other. In a perfectly symmetrical situation, it corresponds to one half of the whole hysteresis loop width. Its value is considered as positive for the P to AP transition, and negative conversely. The magnetization loop is also characterized by another parameter, the offset field, H_{off}, which quantifies the hysteresis's center shift with respect to a symmetrical situation.

Anyhow, switching to one state to the other means writing in the MTJ the suitable bit value. This can be done in several ways depending on the MRAM technologies. Therefore, these latter can be grouped according to whether the writing mechanism is the field or the Spin Torque Effect. Accordingly, we can recognize 4 families of MRAM: Field Induced Magnetic Switching (FIMS), Thermally Assisted Switching (TAS), Spin Transfer Torque (STT) and Spin Orbit Torque (SOT).

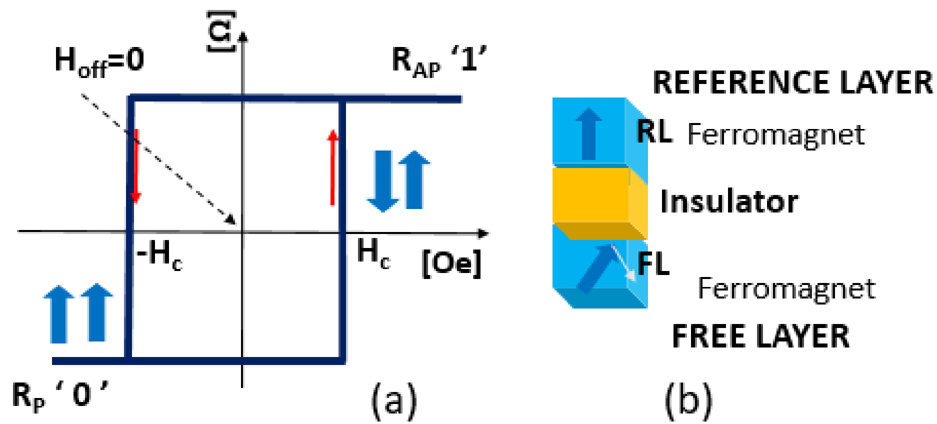

Figure 5: Hysteresis loop: switching the FL from one stable state to the other (a). Schematic view of the three main MTJ layers (b)

For these motivations, numerous market players are involved into the Emerging memories business as summarized in Fig. 6.

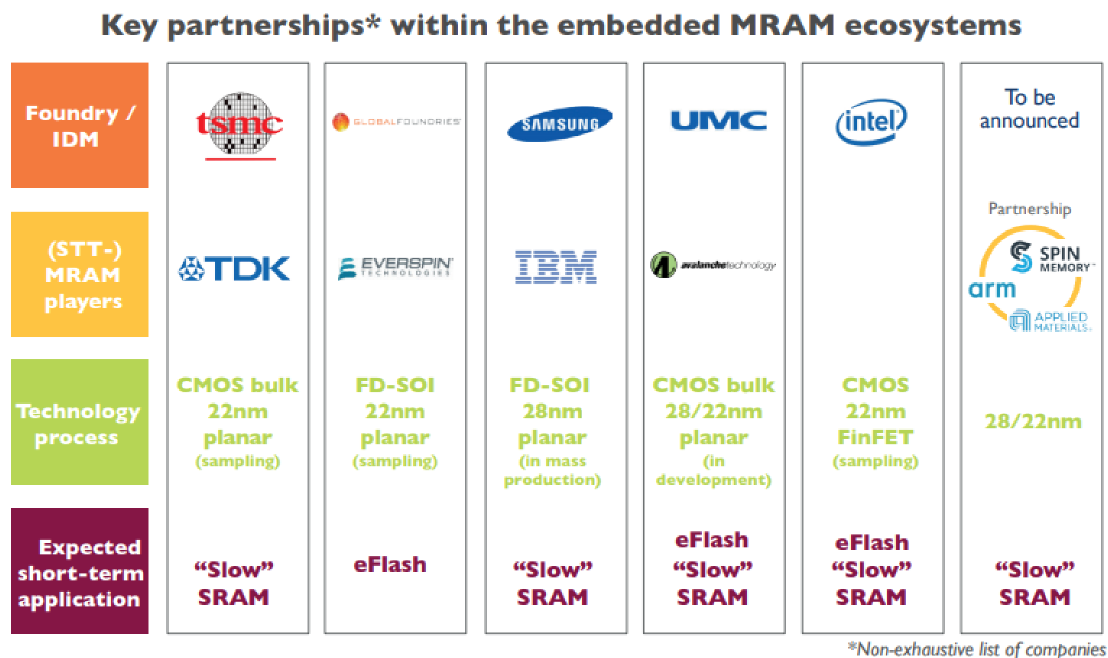

Figure 6: Key players in the MRAM ecosystem [124]

1.5.1 Field Induced Magnetic Switching Toggle

In the Field Induced Magnetic Switching (FIMS) MTJ, as the name suggest, a field is used to switch the FL configuration. For this reason, a large current (∼10 mA) is required in order to create the magnetic field pulses (∼10mT) [29]. Moreover two write lines are needed for this mechanism to take places successfully as shown in Fig. 7. Fig. 8 shows the specific write sequence of the FIMS Toggle MRAM, which is an improvement of the original FIMS writing mechanism. this technique has been developed by Everspin: a sequence of magnetic fields produced by two lines are used to gradually turn the magnetic

orientation by steps of 45°. These constrains lead to some evident drawbacks as huge size, writing complexity and poor scalability. Besides this, as Toggle represent the first generation of MRAM, they have reached a maturity of development such that these devices are commercialized by Everspin. Additionally, toggle MRAM are the only magnetic memory existing, at this moment, in an extraterrestrial environment: Mars. Designed for applications requiring extreme data reliability and speed, Everspin's 16-Megabit Toggle MRAM (MR4A16BMA35) has been embedded on board of Perseverance Rover, successfully landed on the Red Planet the 18th February 2021 (Fig. 9). It handles the memory functions for the motor controls by benefiting from symmetrical read/write performance and unlimited endurance.

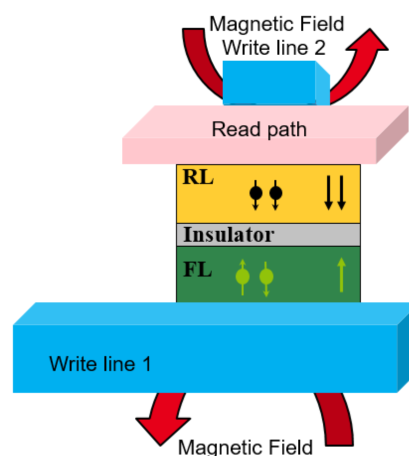

Figure 7: Schematic view of a Toggle MTJ.

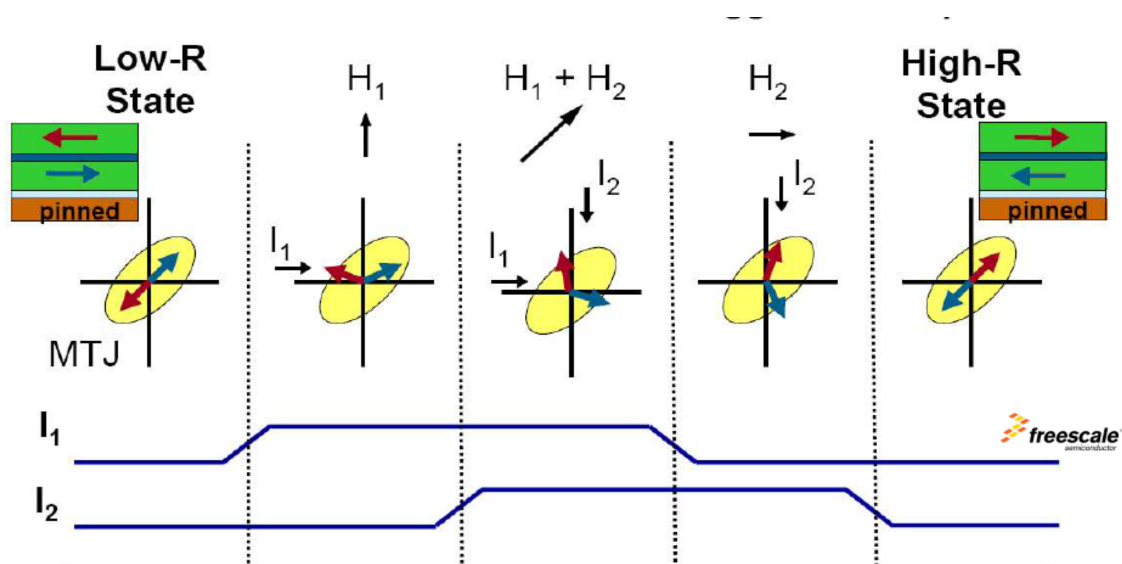

Figure 8: Write sequence of a Toggle MRAM [84]

Nevertheless, other important limitations in the use of Toggle MRAM technologies indicate that other technologies are needed for future, more extensive applications. According to Everspin specifications, these limitations can be summarized as follows [116]:

Figure 9: Perseverance rower on Mars. Inset: the space qualified Toggle MR4A16BMA35 from Everspin.

- Large cell size (30F^2)
- High power consumption (2x 16 mA / bit)
- Low speed (Read before write)
- Slow write: 35 ns R/W symmetric
- High sensitivity to disturb field <25 Oe in (shielded) package
- Downsize scalability limited by electromigration

1.5.2 Thermally Assisted Switching

Thermally assisted switching (TAS) was developed by Spintec [100]. The key idea of this technology is to heat the MTJ above the Blocking Temperature (T_b) thereby enabling the storage of the information thanks to the application of a reduced magnetic field (Fig. 10). This leads to to creation of the company Crocus Technology in 2006 [20]. The magnetic field needed to switch the FL is lowered with respect to Toggle MTJ. As a result, this technology shows a better scalability. Fig. 11 shows a typical TAS writing cycle. However, since writing method of the TAS-MRAM is based on the possibility to heat the junction to unlock the storage layer magnetization, without affecting the stability of the reference layer, this approach is largely influenced by the choice of materials and their blocking temperatures. In other words, the writing temperature should be higher than the T_b of the storage layer while remaining below the T_b of the reference layer. Hence, the operating

temperature range is limited to temperatures compatible with stability of the storage layer. If the memory point temperature increases, for example by increasing ambient temperature, two resistance states are possible at zero field and the stored information is lost. Another possible source of error could occur above T_b since in this phase the information can be reversed by any external magnetic fields.

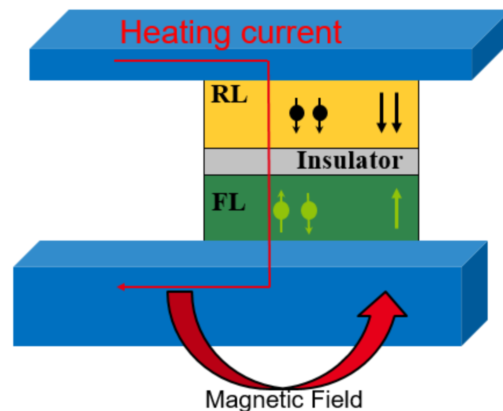

Figure 10: Schematic view of a TAS MTJ

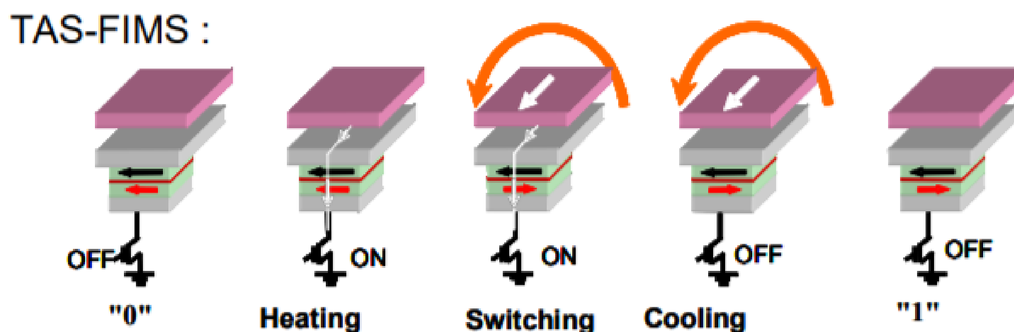

Figure 11: Writing operations sequence in a TAS-MTJ [100]

1.5.3 Spin-Transfer Torque

Conventionally, a Spin-Transfer Torque (STT) MTJ is composed of a free CoFeB ferromagnetic layer (FL), a pinned CoFeB ferromagnetic layer (RL) layer separated by an insulating MgO tunnel barrier. Below the RL is placed a synthetic antiferromagnetic layer (SAF) composed of [Co (0.50)/Pt (0.25]$_3$ antiferromagnetically coupled through a thin Ru spacer (0.9) to an other multi-layer [Co (0.50)/Pt (0.25]$_6$, where numbers in parentheses stand for layer thickness, expressed in nanometers. Indeed, the RL pinned magnetization leads to an unwanted magnetic field (stray field) that originates from the RL and results in only one possible resistance state. Since the SAF forms a flux closure structure, most of the flux from the reference layer is absorbed in the pinned layer and so two stable resistance states are possible [27]. Thus the magnetization curve is an hysteresis loop as

described in Fig. 5. It is worth to emphasize that the symmetry of the hysteresis loop (offset field equal to 0) is due to the SAF compensation effect. The SAF structure is important both to minimize the dipolar field that acts from the RL on the FL, by aligning them in the parallel configuration, and to increase the perpendicular magnetic anisotropy (PMA). This latter is the crucial effect responsible for the correct spin switching dynamics and it originates at CoFeB/MgO-MgO/CoFeB and Co/Pt-Pt/Co interfaces, as Fig. 12 clarifies.

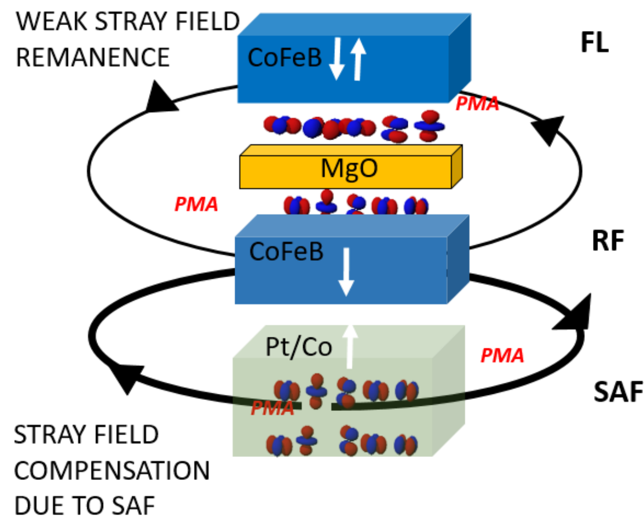

Figure 12: Compensation of stray field by means of SAF

The final magnetic orientation has to be perpendicular to the plane [48]. This is the result of an improvement with respect to the first STT-MTJ generation characterized by a parallel orientation of the magnetization regard to the plane as depicted in Fig. 13.

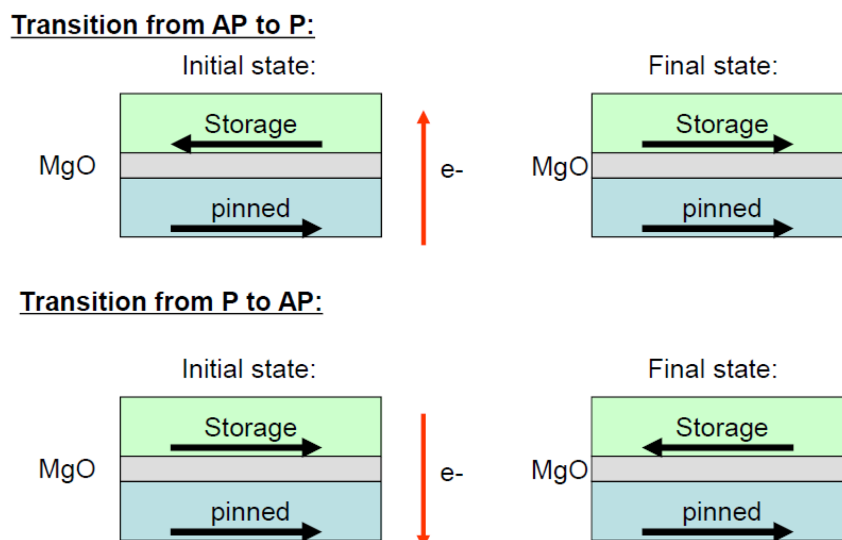

Figure 13: In plane STT-MTJ switching.

PMA-MTJ enhance reliability, power consumption and density by, respectively, im-

proving the thermal stability, reducing the switching current, and eliminating the elliptical shape constraint.

One of the important key properties important for spintronic materials is the high spin polarisation. Spin polarisation is the degree to which spins are oriented along a specific direction. Different types of materials can produce spin polarised currents as the electrons pass through them. Denoting with P the degree of spin polarisation of the conduction electrons at the Fermi energy level (EF) it is possible to write:

$$P = \frac{D_{up} - D_{down}}{D_{up} + D_{down}} \tag{1.3}$$

For a non-magnetic metal, the conduction bands are the same for spin-up and spin-down electrons. Hence the current passing through it has no spin polarisation at zero field, i.e. P = 0. In ferromagnetic materials the spin-up and spin-down are exchange split due to Coulomb interaction, hence, depending on the material, the current passing through it will be to some degree spin polarised, i.e. $0 < P < 1$. Fig. 14 shows the band population in the parallel and antiparallel states.

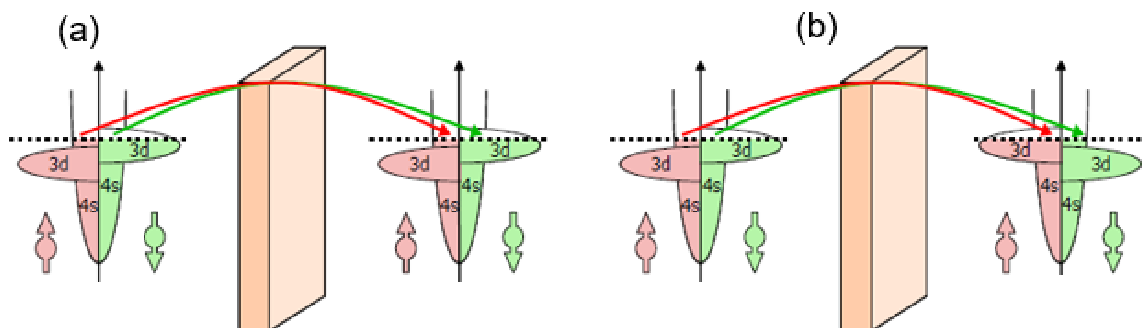

Figure 14: Schematic diagram of spin-polarised electron tunnelling: parallel(a), antiparallel (b) configuration. The involved atomic orbitals are the 4s and the 3d.

Thence, the transfer of spin acts as a torque (τ_{ST}) to destabilize either one of these positions by modifying the local magnetization direction. For this to happen, the current pulse must have a proper amplitude and intensity to overcome the damping factor, namely it has to be above the minimum switching required current (critical current) as illustrated in Fig. 15.

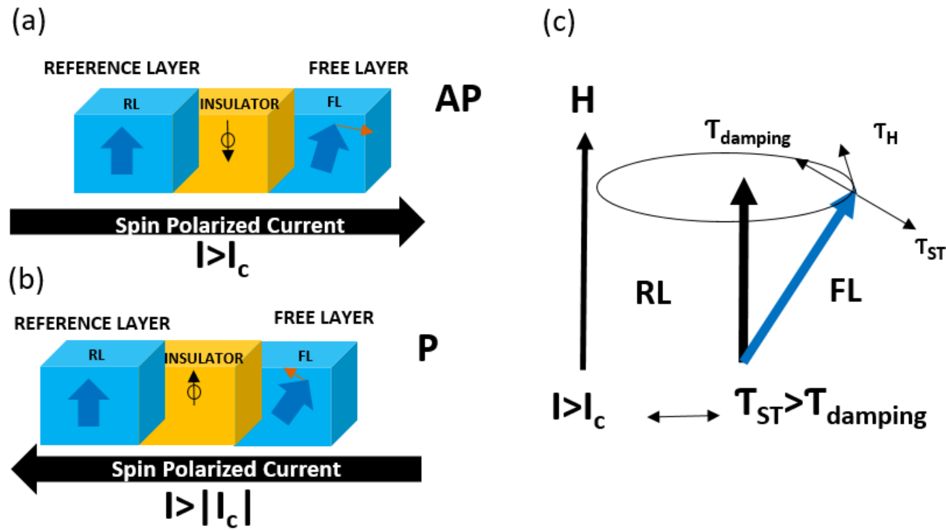

Figure 15: A spin polarized current flows from the RL to the FL to switch towards AP state (a). A spin polarized current flows from the FL to the RL to switch towards P state (b). Spin transfer torque dynamic (c).

This current is generate by a voltage pulse on the gate of the access transistor. It is important to highlight that the write and read voltage pulses should be properly chosen, to avoid to over stress the MgO barrier, otherwise it will eventually experience a breakdown, as detailed in Fig. 16. In particular:

- V_{write}<<$V_{breakdown}$, for good write endurance, typically V_{write}= 0.4 V and $V_{breakdown}$=0.9 V.
- V_{read}<< V_{write}, to avoid disturb during read, V_{read} = 0.15V
- V_{read} must be large enough (0.15 V) for reasonable read speed (10 ns)

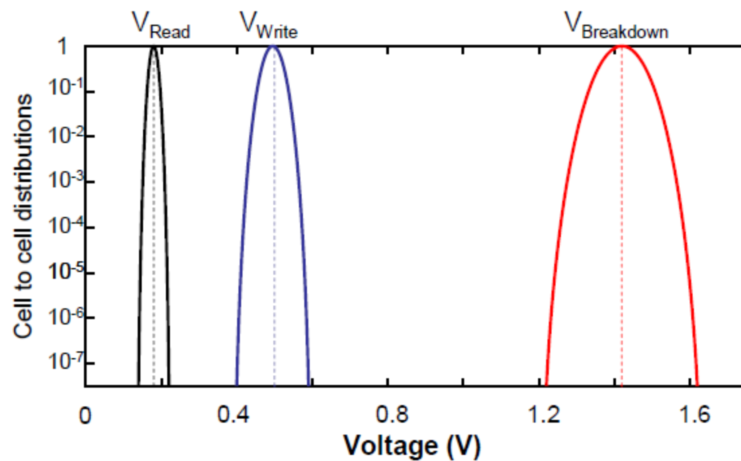

Figure 16: Typical read, write and breakdown voltages

Additionally, while the voltage to switch from one stable state to the other is the same, the current is not. This is understandable by the fact that:

- Ferromagnetic materials have an imbalance of spin up and spin down electrons.
- Electron spin conserved during tunneling.
- The total electron current in a given state is constrained by the minimum number of available states on both sides of the barrier.
- MTJ is a resistive element thus either in high state or low state when starting the writing phase.

Therefore the total current is greater when the magnetic materials on both sides of the barrier are aligned. In conclusion, the critical current, I_c to switch in both directions the magnetization state is given by:

$$I_c = \alpha \frac{\gamma e}{\mu_B g}(\mu_0 M_s) H_k V = 2\alpha \frac{\gamma e}{\mu_B g} \Delta E \quad (1.4)$$

Where α is the Gilbert damping factor, γ is the gyromagnetic factor, e is the electron charge, μ_B is the Bohr magneton constant, g is the spin polarization efficiency, $\mu_0 M_s$ is the saturation field of the free layer, H_k is the anisotropy field, V is the volume of the free layer and E is the barrier energy [128].

From Equation 1.4 it follows that low STT write current implies low Gilbert damping, high current polarization and low magnetization. Interestingly, Equation 1.4 has an alternative, equivalent, formulation which allows to define an other important parameter, the thermal stability factor (Δ):

$$I_c = 2\alpha \frac{\gamma e}{\mu_B g} \Delta K_B T \rightarrow \Delta = \frac{\Delta E}{K_B T} \quad (1.5)$$

The energy barrier, ΔE, which divides the two stable opposite states (AP, P), depends in a complex way on both M_s and K_u (and on the free layer volume, V) [73]:

$$\Delta E = V \frac{K_u - \mu_0 M s^2}{2} \quad (1.6)$$

Nonetheless, in macrospin regime (r<30 nm) the barrier height, could be approximated, in a simplified way, as:

$$\Delta E = K_u V \quad (1.7)$$

where K_u is the perpendicular anisotropy and V is the FL volume. Δ is directly related to the memory retention time by the following inequality:

$$\frac{K_u V}{K_B T} > ln(\frac{T}{\tau_0}), \tau_0 = 10^{-9} ns \quad (1.8)$$

where T is the desired retention time. For example, achieving a stability of 10 years at 80 C implies, for 1 bit, $K_u V > 40 K_B T$. It follows that a temperature rise, combined with the

radius scaling, will drastically reduce the thermal stability of the memory device, as the plot in Fig. 82 illustrates.

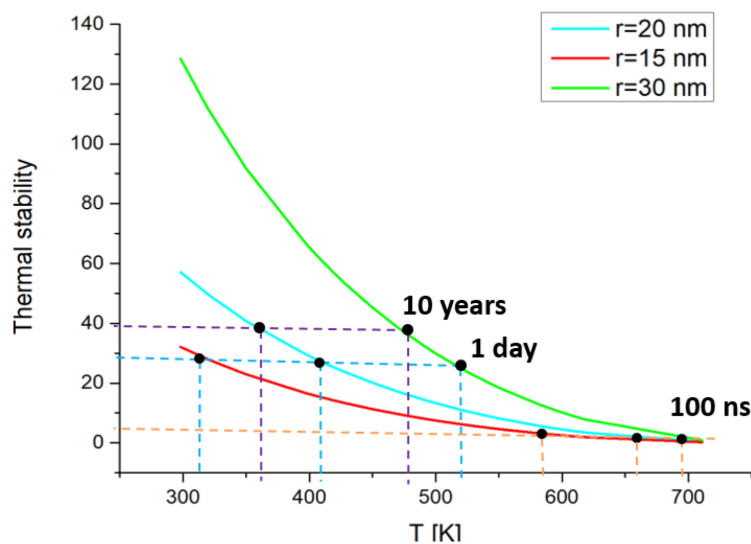

Figure 17: Thermal stability factor and retention time impacted from scaling and temperature rise. Three different MTJ's radii (r) are analysed.

A lot of research has gone into improving the multi-layered stucture with the aim to solve the retention/ writability dilemma: for example, the single MgO-based MTJ design has been changed to a double MgO-based p-MTJ design to enhance thermal stability and perpendicular magnetic anisotropy [72] [22]. Fig. 18 shows the complete stack of a double barrier PMA STT-MTJ. In addition, it has been shown that a p-MTJ incorporating a Tungsten (W) based seed bridging and capping layer instead of the Tantalum (Ta) enhances both the TMR ratio and thermal stability [71]. A thin layer of Tantalum has been inserted into the CoFeB FL to absorb the B away from the MgO interfaces during the annealing; this way allowing the crystallization of the CoFeB layers into body-centered cubic (bcc) structure thus further increasing the PMA at MgO/CoFe interfaces [27]. These distinctions in the multi-layer stack design have important consequences for the study of irradiation effects as we will detail in the next chapters. Fig. 12 (b) details the device stack of double MgO STT-MTJ. Fig. 19 summarized the key STT-MTJ parameters.

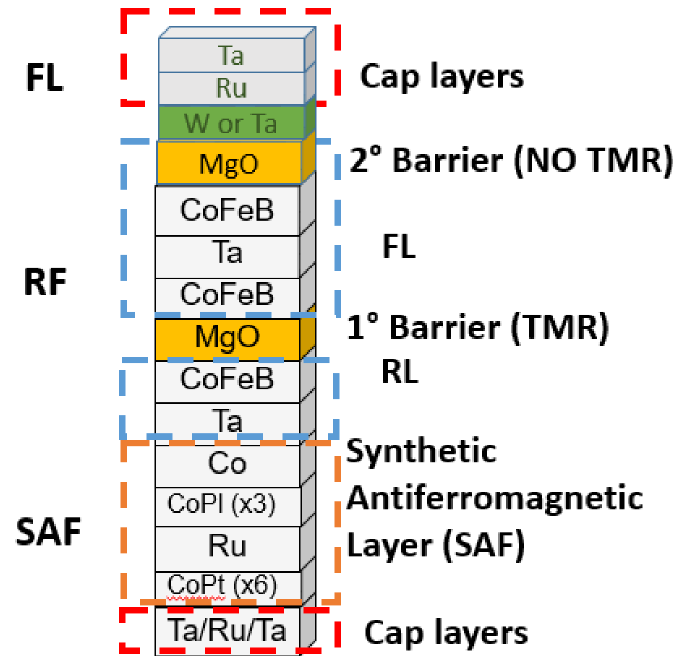

Figure 18: Advanced PMA-STT MTJ stack.

Parameter	Symbol	Unit	Value	Ideal value
Thermal stability factor	Δ	-	60-90	As high as possible
Tunnel Magneto Resistance	TMR	%	90-150	As high as possible
Current density	J0	A/cm2	$<10^6$	As low as possible
Polarisation	P		0.85	As high as possible
Breakdown voltage	Vbd	V	1.5 V for a pulse of 10 ns at V_{write} =0.5 V	As high as possible
Coercive field	Hc	Oe	1500-2000	Symmetrical
Offset field	Hoff	Oe	~80	As low as possible
Damping factor	α	-	0.01	As low as possible

Figure 19: Main STT-MTJ parameters.

This memory has very good properties today, allowing large companies, notably IBM, Samsung, Toshiba, TSMC and Everspin to develop STT-MRAM chips. It offers a programming speed of a few ns, an endurance up to 10^{16} cycles and a high density that can

reach 5 nm in diameter of the MTJ according to [103]. Additionally, STT-MTJ can be easily integrated into CMOS back-end of line process (BEOL). Typically, they are inserted between Metal 3 and Metal 4 as depicted in Fig. 20. Many works have also shown that the introduction of STT-MRAM in the cache levels or in the logic allows to decrease the standby power consumption. During the 2020 IEEE International Electron Devices Meeting (IEDM 2020), IBM announced that efficient and high-performance STT-MRAM systems will help to address memory-compute bottlenecks.

Additionally, due to its unique futures, STT-MRAM has attracted the attention of harsh environment application. Automative, space and military field of application are targeting for future products STT-MRAM, since this latter combines the benefit of Toggle-MRAM with higher endurance, scalability and lower power consumption. As an evidence of this, at the end of 2020, STT-MRAM has been selected for a NASA AI project titled "DNN Radiation Hardened Co-processor as companion chip to NASA's upcoming High-Performance Spaceflight Computing Processor" [94]. In this framework, STT-MRAM will be used to develop a reconfigurable Deep Neuronal Network (DNN) Engine with multiple compute units which can support a wide range of DNN models and frame rates.

According to Yole Development report of 2018 the STT will become the most used Emerging Non Volatile Memory by 2023 [124].

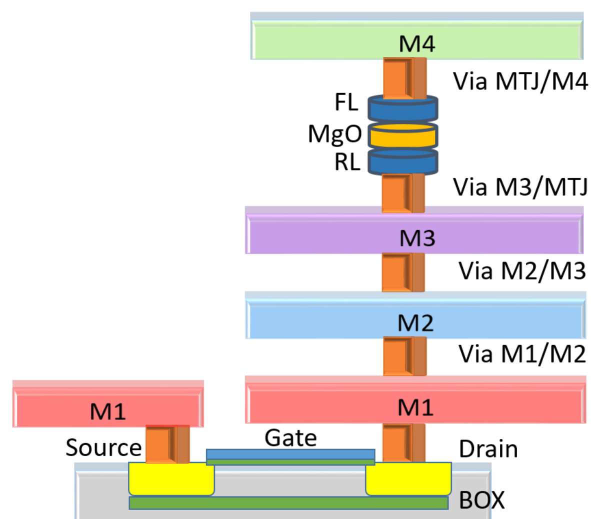

Figure 20: MTJ integration in the CMOS process.

1.5.4 Spin-Orbit Torque

The main drawback of STT-MRAM is the shared read/write path which can impair the MTJ reliability in two different ways. In the one hand, the write current can impose a severe stress over the insulating barrier leading to a possible time dependent degradation of the MgO and consequently compromise the MTJ endurance. On the other hand, if the reading current is too high, unwanted writing could occur during reading opera-

tions. Trying to go beyond these limits, a new proof of concept was presented in [4] and [75] hereby providing a new approach for controlling magnetic device: Spin-Orbit Torque (SOT) MTJ. The latter is a three terminal device where reading and writing paths are decoupled thereby enhancing the robustness of the simple STT-MTJ pillar. Indeed, it no longer needs to be traversed by a large write current, which instead passes through a strip of metal underneath the MTJ, called the SOT channel. This separation significantly enhances the reliability of the device [37] since the write current does not flow through the tunnel barrier, which is sensitive to electrical breakdown. Due to their write mechanism, SOT devices provide also faster switching (in the range of 350-500 ps) with respect to STT devices [21] [42]. Fig. 21 illustrates both STT and SOT MTJs reading and writing paths.

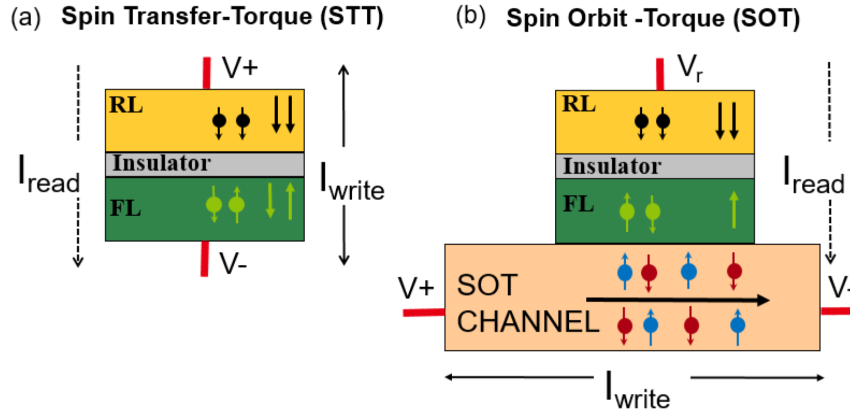

Figure 21: Comparison between STT-MTJ (a) and SOT-MTJ (b) writing and reading paths.

For this motivation SOT devices gained the attention of industry [5] and academia [3] confirming attractive qualities such as a very fast switching, a theoretically infinite endurance and the elimination of the read disturbance. Physically, two phenomena are understood to be at the origin of the spin-orbit torques: a bulk component, the Spin Hall Effect, and an interfacial component, commonly known as the Rashba-Edelstein Effect, as depicted in Fig. 22. In the Spin Hall effect (SHE), an applied charge current density flowing through a heavy metal (HM) such as Pt,Ta or W generates a transverse-flowing spin current density [130]. This leads to a spin accumulation at the SOT interfaces, which then diffuses into magnetic materials. In other words, the heavy metal layer converts the in-plane charge current J_c to an out-of-plane spin current J_s via the spin Hall effect as expressed by the equation:

$$J_s = \theta_{SHE} \cdot J_c \tag{1.9}$$

where θ_{SHE} is a material parameter called spin Hall angle.

The Rashba-Edelstein effect originates from the uncompensated electric field at the interface, resulting in an effective magnetic field directly acting on nearby magnetizations

(Fig. 21 b).It can be expressed as:

$$H_R = -\alpha_R(\sigma \times p) \cdot z \tag{1.10}$$

where, σ represents the Pauli matrix, p the isotropic bands of the orbital p, and α_R depends on electron magnetic moment and Electric field resulting from the inversion symmetry breaking in the direction perpendicular to the two-dimensional plane.

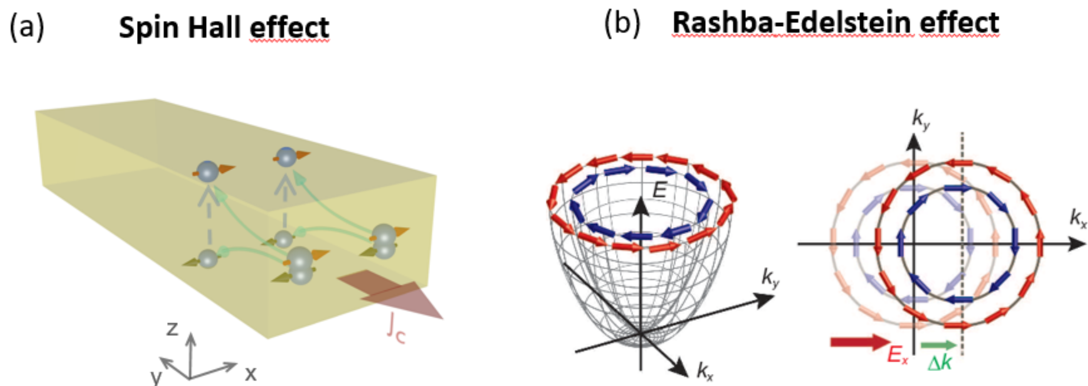

Figure 22: Current induced Spin Hall Effect (a) and Rashba-Edelstein effect (b).

The main drawback of this technology is that it needs high current density for switching and its three terminal structure takes up more space than STT, so it has a lower density of high scale integration. However, a lot of effort is being made at research level to optimise such devices. Indeed, a very attractive design for high density application was recently proposed in [81], where the SOT channel is shared among different device as depicted in Fig. 23.

As SOT-MRAM is the youngest technology compared to other MRAM technologies, further research is needed before launching it on the market.

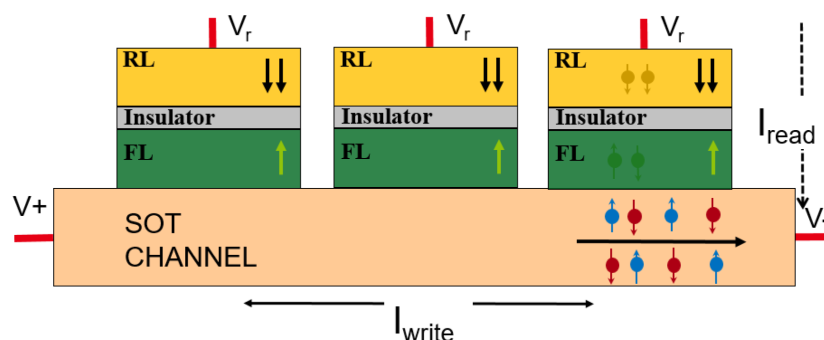

Figure 23: Common channel shared between various SOT-MTJ allowing a very dense integration.

1.6 Conclusion

In this chapter we have reviewed various emerging Non-Volatile memories.

A very recent study from Sydney University demonstrates FeRAM have limited life cycle. Indeed, with each polarisation cycle, small areas in the material grew in size, and these areas are unable to hold electric polarisation anymore [28].

ReRAM and PCM suffer from conductance variability and non-linear change of conductance upon identical programming pulses. However, recent study turn these disavantages in strengh points by demonstrating that they can be used as synaptic elements thanks to tunable conductivity. Indeed, certain properties of these devices, usually considered non-idealities for memories application, can improve the performance of Spiking Neural Networks [35].

Concerning the Magnetic memories, Toggle faces scalability and power consumption issues but they are very mature on market to the point that they have currently been used for space missions. TAS suffers from scalability problems and difficulty to operate in various temperature range. Moreover the power consumption is reduced with respect to the Toggle but it has still a remarkable value compared to STT. For all these reasons TAAS is not used fro memory/logic applications. However, Crocus Technology is commercializing its TAS devices fro magnetic sensor.

STT appears to be the best alternative combining ultra low power consumption, very high endurance, high speed and high scalability. Still, this technology could suffer from the read disturbance, due to the shared read and write paths. SOT, at their initial stage of developing, are capable to overcome this issue but they pay the penalty of being a 3 terminal devices so less scalable and a bit more power consuming. Fig. 24 summarized the main Emerging Non Volatile memories features.

It is thus clear that there is not silver bullet in the choice of the Emerging Non volatile memories. Depending on the application, one of these technologies could be more suitable than the other. However, what definitely made STT and SOT to stand out with respect to the other technologies is their low power consumption, endurance and cell size.

As an evidence of this, the Global MRAM market size was valued at USD 307.5 millions in 2016 and is presumed to gain traction over the forecast period. The increasing demand for wearable and flexible electronic products is expected to drive the growth for this sector. As depicted in Fig. 25 this market appears dominated by STT-MRAM.

	Cell size	Access time*[ns] Read/write latency	Power consumption	Endurance*	Maturity
FeRAM	10 F^2	20	Medium	10^{11}	Commercilized
PCRAM	6-12 F^2	20-50/50	Law	10^8	Commercilized
ReRAM	6-12 F^2	250	Medium	10^7	Commercialized
Toggle MRAM	30 F^2	35 /35	High	10^{15}	Commercialized
TAS MRAM	20 F^2	30/30	High	10^{15}	Test chip
STT MRAM	6 F^2	2-8/2-10	Medium	10^{12}-10^{15}	Commercialized
SOT MRAM	16 F^2	2-8 /0.35-0.5	Medium	> 10^{15}	Test chip

Figure 24: Comparison between Emerging Non Volatile memories technology, adapted from [124].(*) average values.

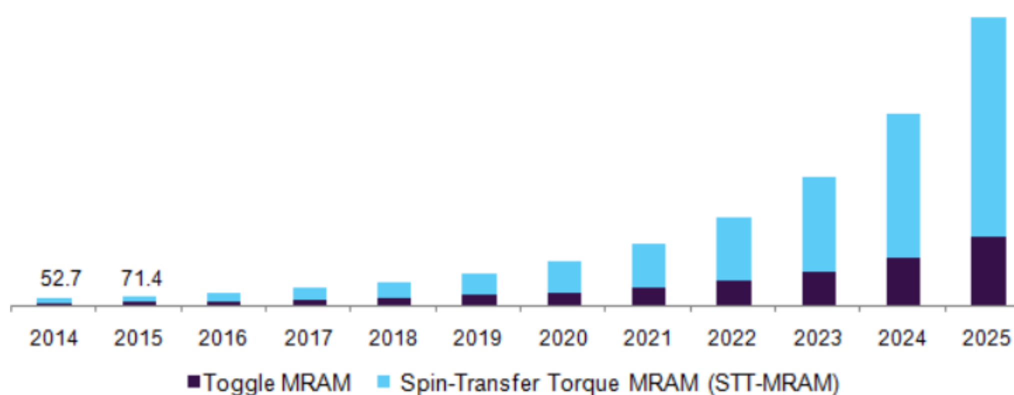

Figure 25: Asia Pacific Magneto Resistive RAM (MRAM) Market, by type, 2014 - 2025 (USD Million) [82]

Chapter 2

Space environment

2.1 Introduction

It was not until shortly after the beginning of the satellite era in 1958 that the presence of high energy charged particles around the Earth (Van Allen belts) was discovered. Since then, it has became evident that the space environment is a highly disruptive medium for space missions. Beyond the natural protection provided by a planet's atmosphere, various types of radiation can be encountered. Their characteristics (energy and nature), origins and distributions in space are extremely variable. Conventionally, the classification of orbit types relies on parameters such as altitude, speed, and period as detailed in Fig. 26 and intuitively shown in Fig. 27.

However this environment degrades electronic systems and on-board equipment in particular and creates radiobiological hazards during manned space flights.This naturally leads to a detailed study of the space environment and of the effects that it induces on space vehicles and astronauts.

Radiation conditions in the near-Earth's space are resulted from joint action of the three main factors: galactic cosmic rays, solar energetic particles and radiation belts. Energetic particles originated from radiation environment of the Earth can cause effects like ionizing dose and displacement damage, as well as electrostatic discharge and single event effects that damage spacecraft materials and electronic components. During geomagnetic disturbances, radiation conditions in some regions drastically changed and became much more dangerous for spacecraft.

Important terminology in the study of space environment and radiation-effects on electronic circuits are:

- Flux: the number of incident particles per surface unit and time [p/cm^2/s]
- Fluence: integration of the flux over the time [p/cm^2]
- Sensitive volume: the artificially defined geometry volume inside a device, which is supposed to be sensitive to radiations
- Critical charge: the minimum charge that must be deposited by a particle strike to cause a circuit to malfunction [fC]

- Cross section: a measure of the probability that an error occurs when a specific fluence intersects a localized circuit [cm^2]

Orbit	Meaning	Altitude [Km]	Speed [km/s]	Period [hours]
LEO	Low Earth Orbit	160-2000	8	1.5
MEO	Medium Earth Orbit	2000-35786	3-8	2-24
GEO	Geostationary Earth Orbit	35786	3	24
GSO	Geosynchronous Orbit	35786	3	24
HEO	Higly Elliptical Orbit	40000	1.5-10	12

Figure 26: Orbit types features.

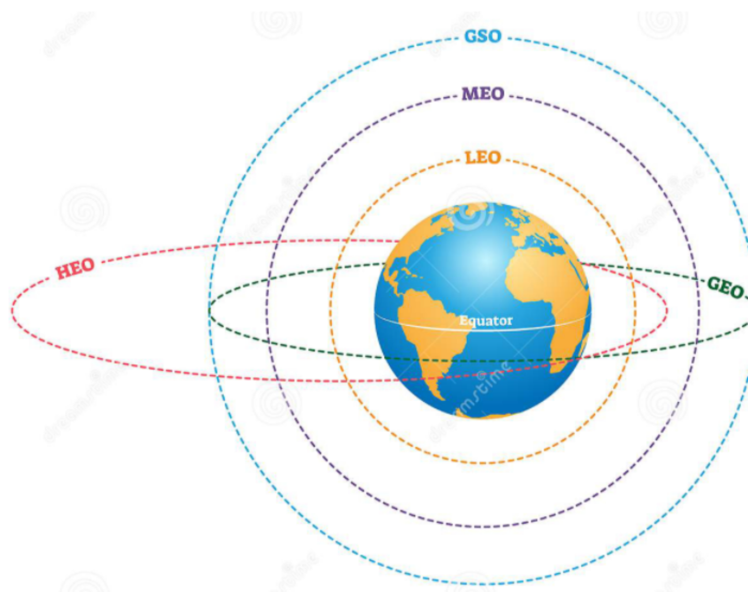

Figure 27: View of the different Orbit types.

2.2 Solar event and solar particles

The solar cycle is divided into two activity phases: the solar minimum and the solar maximum. An average cycle lasts about eleven years with the length varying from nine to thirteen years. When the most intense solar energetic particle events occur, so do a wide range of solar and interplanetary phenomena including optical, x-ray and gamma

ray emission, solar radio bursts, interplanetary radio bursts, coronal mass ejections, and interplanetary shocks. The energetic particles are only one manifestation of a complex sequence of events that begins with a large energy release at the Sun and involve also solar flares. A solar flare is a burst of electromagnetic radiation characterized by a sudden brightening.

The solar wind is a steady stream of plasma (a gas of free ions and electrons) consisting of protons, alpha particles and electrons in the eV to keV energy range and has an embedded magnetic field. Coronal Mass Enjection (CME) is a large eruption of plasma that carries an embedded magnetic field stronger than that of the solar wind. Its composition is detailed in Fig. 28. Energetic ions of all the most abundant elements in the solar system also arrived at Earth in this event. While they have been called "proton events", and it is the case that protons are the most abundant ion in the energetic population, ions up to and beyond iron in the periodic table are also present in all the energetic solar event.

Hadron composition	Energies	Integral Fluence	Peak Flux
96.4% protons 3.5% alphas 0.1% heavier ions	Up to GeV/amu	Up to 10^{10} cm^{-2}	Up to 10^{6} $cm^{-2}s^{-1}$

Figure 28: Coronal Mass Enjection features.

Solar energetic particle events can flood interplanetary space with protons and heavy ions (He to U) with energies up to 10s or even 100s of MeV[51]. Such events often begin with an eruption at the Sun: a solar flare and/or coronal mass ejection. A first wave of energetic particles arrives at Earth essentially at the speed of light. A second wave of energetic particles, often more intense, arrives along with the CME, especially if it has a shock front. It is believed that the shock itself also accelerates the particles. The mass of magnetized plasma ejected in extreme CMEs can be on the order of 10^{17} grams. CME speeds can vary from about 50 to 2500 km/s with an average speed of around 450 km/s. It can take anywhere from hours to a few days to reach the Earth. On rare occasions, when the proton spectrum extends to very high energies (i.e GeV) the events can even be detected by increases in neutron radiation counters at "ground level", thus being identified as ground level events (GLEs). shows an overview of Solar event.

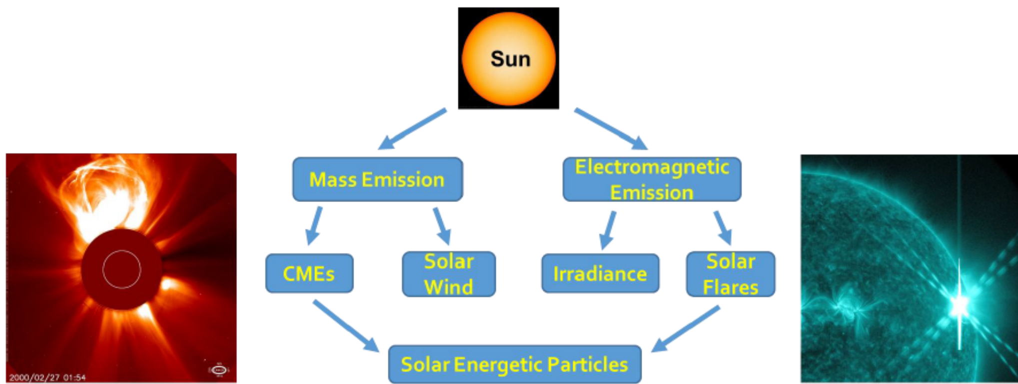

Figure 29: Solar event.

2.3 Radiation Belt

All charged particles immersed in an electromagnetic field will be subject to the Lorentz force:

$$\vec{F} = q(\vec{v} \wedge \vec{B} + \vec{E}) \tag{2.1}$$

where q is the particle's charge, $\vec{v}$ its speed, $\vec{B}$ the magnetic field and $\vec{E}$ the electric field. If the magnetic field is very strong and the energy of the particles is great (and therefore their speed too) then the effect of the electric field can be ignored and the Lorentz force is reduced to $\vec{F} = q(\vec{v} \wedge \vec{B})$. Under these conditions, the movement of the high-energy particles can be generally broken down into three basic periodic movements (the gyration around the field line, the bounce – a back and forth movement between two mirror points respectively in north and south hemisphere – and a drift around the planet). A charged particle submitted to these three basic and periodic movements then moves through torus shaped surfaces around the planet, which are commonly called drift shells as depicted in Fig. 30. These special conditions are thus favorable to the accumulation of high-energy charged particles in certain regions of space which creates the radiation belts. Given the trajectories of the particles, the radiation belts have a toroidal shape which surrounds the Earth. The planet's atmosphere is the lower limit of the radiation belts since it causes the loss of all trapped particles. The upper limit, however, is less clear and is defined by the minimum intensity in the presence of disturbances of the magnetic field such that the particles are always trapped. The particles trapped in the Radiation Belts (or Van Allen belts) are essentially protons and electrons. The energy ranges commonly encountered go from some keV up to some tens or even hundreds of MeV.

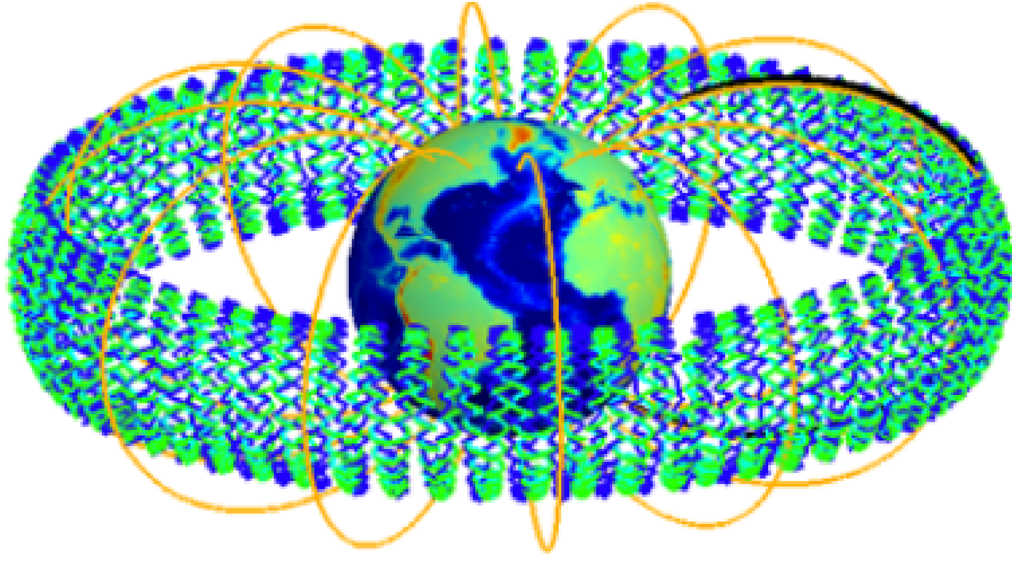

Figure 30: Composition of a charged particle's three periodic movements: gyration, bounce and drift in the Radiadion Belt.

2.4 Trapped protons

Trapped protons, with energies up to a few GeV, are found in the Earth's inner radiation belt with intensity peaking near the magnetic equator at altitudes of about 3000 km (depending on energy). The inner belt is more commonly observed as the South Atlantic Anomaly (SAA), which is a consequence of the offset of the Earth's geomagnetic field relative to its center of mass. For altitudes up to about 2000 km, the radiation is systematically more intense over the South Atlantic and southeastern Pacific Oceans, and less intense or absent over the Indian Ocean. Above 8000 km, the intensity episodically changes in response to solar particle and geomagnetic activity. The energetic trapped proton population with energies > 10 MeV is confined to altitudes below 20000 km, while protons with energies of a few MeV or less are observed at geosynchronous altitudes and beyond. The maximum flux of > 10 MeV protons exceeds 105 p/cm^2/s. summarizes trapped protons features.

The radiation belt protons originate from two sources: cosmic ray albedo neutron decay (CRAND) and trapping of solar energetic protons. CRAND is a slow and steady process that varies by no more than about a factor of 2 over the solar cycle, on account of heliospheric modulation of the cosmic ray input. Solar energetic protons can be trapped in the inner belt when a geomagnetic storm coincides with a solar particle event.

L-Shell Values	Energies	Fluxes (>10 MeV)
1.14-10	Up to GeV	Up to 10^5 cm^{-2}s^{-1}

Figure 31: Trapped protons features

2.5 Trapped Electrons

Electrons with energies above about 100 keV are typically treated separately from the electron component of the energetic plasma. This distinction is for two reasons: first, at energies above about 100 keV, the electron trajectories are dominated by magnetic forces, and the far more dynamic electric forces can be neglected; second, at energies below about 100 keV, the electrons cannot penetrate anything but the thinnest shielding, such as thermal blankets. Thus 100 keV, or thereabouts, becomes a natural dividing point between plasma electrons and radiation belt electrons.

Trapped electrons are found routinely in the inner magnetosphere, and are often found in two or more belts. Typically, there are two belts, the inner one having somewhat lower energies and intensities than the outer one. The region between the belts is known as the slot, but its location and size depend on energy and magnetic activity. In fact, toward the lower end of the energy range (100 keV), it is quite common for the slot region to fill in during geomagnetic activity – particularly geomagnetic storms. Fig. 32 sum up trapped electrons features.

	L-Shell Values	**Energies**	**Fluxes (>1 MeV)**
Inner zone	1-2	Up to 5 MeV	Uncertain
Outer zone	3-10	Up to 10 MeV	Up to 3 10^6 $cm^{-2}s^{-1}$

Figure 32: Trapped Electrons features.

2.6 Galactic Cosmic Rays

Galactic Cosmic Rays (GCR) are high-energy charged particles that originate outside of our solar system. Indeed, GCRs are found primarily in interplanetary space and, in fact, interstellar space (for a review, see[36]). Like solar energetic particles, GCR access to the Earth's magnetosphere is limited by geomagnetic cutoffs. However, GCR are different from solar particles because they extend to much higher energies (>TeV), have a different ionic composition, are much less intense over the energy range at which solar and GCR particles overlap, and exhibit much less dynamic variability. They are composed of protons and ions with energy spectra distributed around a maximum in the order of 1 GeV/nucleon. GCRs are a major issue in future long term manned missions in deep space, like travels to Mars. GCRs general characteristics are listed in Fig. 33

Hadron composition	Energies	Flux
90% protons 9% alphas 1% heavier ions	Up to 10^{20} eV	1 to 10 $cm^{-2}s^{-1}$

Figure 33: Galactic Cosmic Rays features.

2.7 Neutrons

When GCRs reach the Earth's atmosphere, they collide with atomic nuclei in air and create cascades of interactions and reaction products, including neutrons. Some of these neutrons reach the ground. At terrestrial altitude the particle flux is composed predominantly of electrons, muons, neutrons and a smaller fraction of protons and pions. Even if neutrons are non directly ionized, depending on the incident angle different nuclear reactions can be triggered.

A significant source of neutron-induced SEU is due to very low energy neutrons («1 Mev) interacting with boron (commonly used as a dopant)in the dielectric layers close to the active devices' area. The ^{10}B isotope (abundance 20%) is unstable when exposed to low energy neutrons and breaks into ionizing fragments. The other isotope ^{11}B also reacts with neutrons; however, its reaction cross-section is nearly a million times smaller, and its reaction products, gamma rays, are much less damaging.

The package-level radiation in the terrestrial environment is the sum of three mechanisms: directly ionizing alpha particles emitted from the radioactive impurities in the device materials, terrestrial cosmic radiation (mostly high-energy neutrons), and thermal neutron reaction with ^{10}B in devices. In advanced devices where boron-doped glass is not used anymore, and care has been taken to select all chip materials ultra-low alpha, still the high-energy neutrons are the dominant cause of SEE.

In conclusion, neutrons are present in the atmosphere and their are responsible of on ground SEE, we include them for the sake of completeness. Since our study focuses on the radiation source in space environment and its effects on electronics we are not going to detail further on them. However, secondary neutrons as products of nuclear interaction of protons, heavy ions and so on, are of course pertinent with this study.

2.8 The effect on electronics

2.8.1 Total Ionozing Dose

As a high-energy particle passes through a material, it loses energy by excitation and ionization of atoms, creating a high density electron-hole plasma along its path. The

amount of energy deposited per unit depth in a material (from ionization processes) is given by its electronic stopping power The mass-stopping power is defined as the linear energy transfer (LET), and is given by [87]:

$$LET = \frac{1}{\rho}\left(\frac{dE}{Dx}_{nucl} + \frac{dE}{Dx}_{el}\right) \tag{2.2}$$

where ρ is the density of the material and $\frac{dE}{DX}_{\mathrm{el}}$ is the rate of energy loss in the material from ionizing processes. The LET for a given particle (electron, proton, heavy ion) depends on the target material and on the particle's energy. The TID associated with an exposure to a given particle beam can then be calculated by multiplying the LET of the particle with its total fluence delivered [13].

$$TID = LET(E) \cdot \Phi(E) \tag{2.3}$$

Where Φ is the total fluence of particle at energy E with LET(E).

2.8.2 Single Event Effect

Ionizing radiation mainly generates electron-hole pairs, which impact semiconductor materials, such as silicon (Si), by generating a transient parasitic current. In this section, we will see how one single particle (either neutron or proton or heavy ion) interacting with the semiconductor material can trigger different effects at device level as illustrated in Fig. 34.

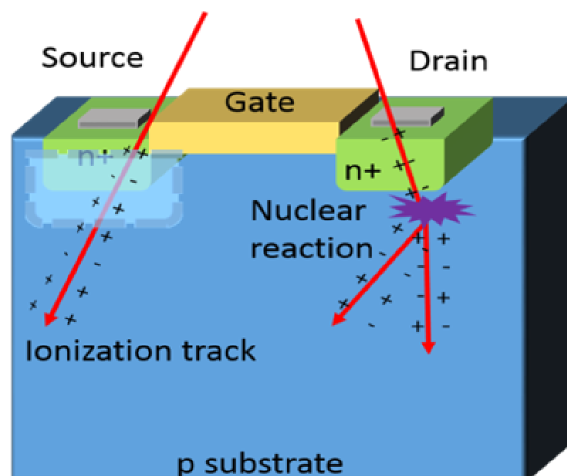

Figure 34: A single particle interacting with transistor sensitive volume creates a cascade of concerning effects.

The manner in which the parasitic single-event-induced current evolves within semiconductor devices depends on the LET of the particle, on the location of the particle hit, on the device being struck, and on the bias applied to the device.

For a single particle interaction with a microelectronic device, there are typically two types of ionizing mechanisms:

- a direct ionization by the particle itself, if its LET is large enough to induce a perturbation of the device;
- an indirect ionization, coming from secondary particles created by nuclear reactions between the incident particle and the target material.

Light particles such as protons and neutrons usually do not generate enough charge by direct ionization to cause SEEs (although this tends to change with device scaling). However, high energy protons and neutrons can both still impact SEE sensitivity via indirect ionization mechanisms. Indeed, when a high-energy proton or neutron enters the semiconductor lattice, it can trigger an atomic displacement, especially after an inelastic collision with a target nucleus. Different nuclear reactions may occur, including elastic collisions that produce Si recoils, emission of alpha or gamma particles and the recoil of a daughter nucleus, and spallation reactions in which the target nucleus is broken into two recoiling fragments. All of these reaction's byproducts can then deposit energy along their paths by direct ionization: basically, these particles will then behave as "regular" heavy ions with a given LET and range, and will deposit charge along their path. Being much heavier than the original proton or neutron, they can deposit higher charge densities and may thus trigger single-event effects.

It is possible to classify the type of Single Events Effects as follow:

Non-destructive effects

- Single Event Transient (SET): a particle generates a transient parasitic current in one transistor; As scaling is aggressive it is possible to have also Single Event multi upset (SEMU)
- Single Event Upset (SEU): a SET that exiced Q_{critic}; If multiple cell are involved it is called Multi cell Upset (MCU) or Multi bit Upset (MBU).
- Single Event Functional Interrupt (SEFI). A particle strike causes the loss of normal operation of a component.

Destructive effects:

- Single Event Latchup (SEL): conduction of parasitic PNPN structure usually a thyristor (Silicon Controlled Rectifier,SCR) results in a sharp increase in current leading to destruction
- Single Event Burnout (SEB): a current that causes the destruction in a power transistor.

- Single Event Gate Rupture (SEGR): destruction of the gate oxide by the creation of a conductive path.

Fig. 35 summarizes the various SEE types.

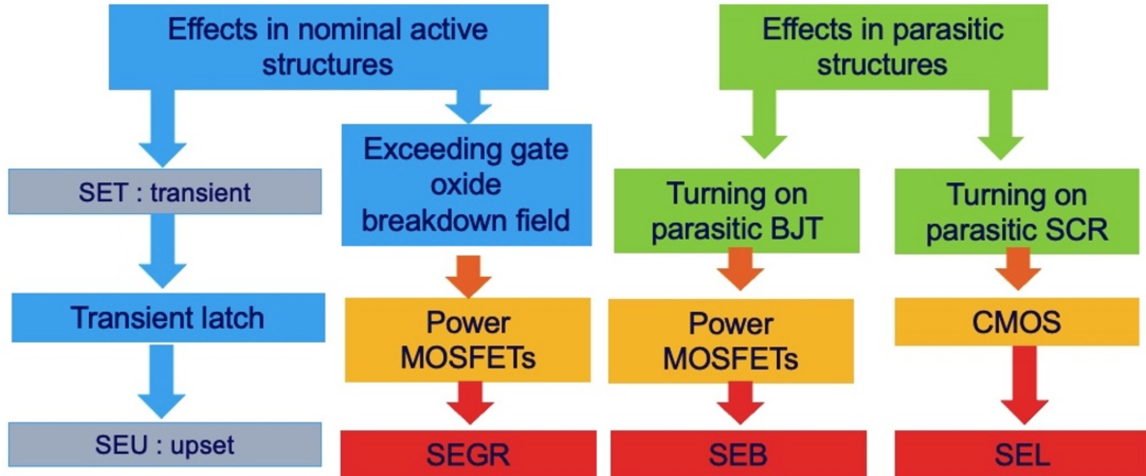

Figure 35: Overview of the various SEE types and their effects on electronic devices

2.8.3 Displacement Damages and Non Ionizing Energy Loss

In addition to ionization effects, high-energy electrons, protons, neutrons, and heavy ions can also cause displacement damage [111] in silicon and other semiconductor materials, when the particle interacts with the nucleus of the atom, instead of the electron cloud. With non-ionizing processes, the energy loss causes the atoms to be displaced from their equilibrium sites, and can lead to lattice disorder. This is the primary interaction process for neutrons, which are charged neutral and do not interact with the electron cloud of an atom. This is also the case for part of the energy lost by electrons, protons, and heavy ions. The amount of energy deposited per unit length in a material (from non-ionization processes) is given by its nuclear stopping power.The mass-stopping power is defined as the non-ionizing energy loss (NIEL), and is given by:

$$NIEL = \frac{1}{\rho}\frac{dE}{Dx}_{nucl} \tag{2.4}$$

where ρ is the density of the material and $\frac{dE}{DX}_{nucl}$ is the rate of energy loss in the material from non-ionizing processes. NIEL is expressed in units of MeV cm^{2}g^{-1}. The NIEL for a given particle (electron, proton, heavy ion) depends on the target material and on the particle's energy. The Displacement Damage Dose (DDD) associated with an exposure to a given particle beam can then be calculated by multiplying the NIEL of the particle with its total fluence delivered.

$$DDD = NIEL(E) \cdot \Phi(E) \tag{2.5}$$

Where Φ is the total fluence of particle at energy E, with NIEL(E). An incident particle may collide with a semiconductor nucleus and displace it from its site, producing a primary knock-on atom (PKA). This initial recoil can be produced by any of the following processes: Rutherford (i.e. Coulomb) scattering, nuclear elastic scattering, and nuclear inelastic scattering. Once any of those basic interaction processes produces a PKA, that ion subsequently can introduce further displacement damage by Rutherford and nuclear scattering. Lattice defects are produced by PKAs and any later-generation energetic recoils that they create, if given a sufficient amount of energy. Thus this PKA will displace a second atom (secondary knock-on atom, SKA), and possibly more so, until the energy it can transfer becomes lower than the threshold required for atomic displacement in the material.

The minimum energy required to knock an atom free of its lattice site is called the displacement threshold energy (E_d). In silicon the value $E_d = 21$ eV is generally well admitted for protons, neutrons and heavy ions. Each displaced atom (PKA, SKA, etc. . .) will in turn also do the same if its kinetic energy is large enough. Thus a collision cascade can proceed until no more atom can transfer enough energy to induce a displacement. At a given incident particle energy, the recoil atoms can vary in kinetic energy from near zero up to some maximum determined by the collision mechanisms. Both the average recoil energy and the shape of the recoil spectrum depend on the energy, mass, and charge of the incident particle and the mass of the target. Once an atom is displaced from its original position in the crystal, it leaves behind a vacancy. The combination of the interstitial atom and its vacancy is called a Frenkel pair as shown in Fig. 36

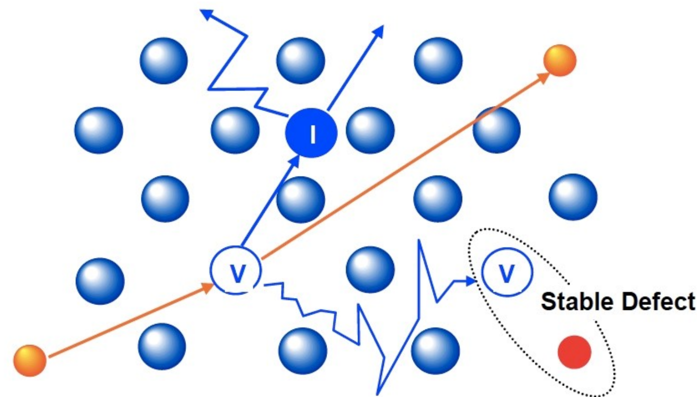

Figure 36: Displacement Damage mechanism: vacancies and interstitials migrate either recombine (90%) or migrate and form stable defects called Frenkel pair (10%).

As the PKA travels through the silicon, it displaces other atoms but its trajectory is also modified, and its energy decreases. Towards the end of the paths of all these reflected atoms (the PKA and all impacted atoms) lose a significant portion of their energy, and large clusters of defects may form (terminal clusters). Apart from isolated vacancies from Frenkel pairs, additional types of radiation-induced defects arise when vacancies or interstitials combine with other vacancies or impurity atoms and/or dopants. This creates defect-impurity complexes for example di-vacancies, a common semiconductor defect. Larger groups of vacancies may also be created, and arrangements of such large groups of vacancies might very well be at the origin of clusters.

The most important effect of displacement damage in a material is the creation of deep and shallow level states. The effects on the electrical and optical properties of semiconductor materials and devices can be explained by radiation-induced energy levels introduced in the bandgap. Deep level states can act as generation, recombination, or trapping centers. These centers can decrease the minority carrier lifetime, increase the thermal generation rate of electron-hole pairs, and reduce the mobility of carriers. Shallow level traps can compensate majority carriers and cause carrier removal. As a result, displacement damage is a concern primarily for minority carrier and optoelectronic devices. It is generally not an issue for MOS transistors except at very high particle fluences.

2.9 Means of prevention from radiation effects

Shielding can play a role in the single event effect rate if you are susceptible to low energy particles, but predominantly the higher energy particles are not well shielded and will still penetrate to the part's sensitive volume. Most of the reduction in flux only occurs at energy levels less than 10 MeV, where secondaries that have higher LET are not produced or lack sufficient range to traverse a sensitive volume. As it has been demonstrated in [123] [105], even substantial mass addition for shielding does not attenuate or prevent SEE. For example, the continuous isotropic flux of highly energetic cosmic rays of galactic origin (GCR) is not immediately fatal and become a threat to astronauts' health if the dose is accumulated during several-month stays in the deep space. Consequently, a small thickness of shielding mass is not only ineffective against GCRs, but can be detrimental due to the generation of secondary particles. An enough thick passive shield can, in principle, reduce the radiation dose to acceptable values but it leads to substantial increase of the spacecraft mass [92]. Fig. 37 shows how different materials and shielding thickness impact the equivalent dose.

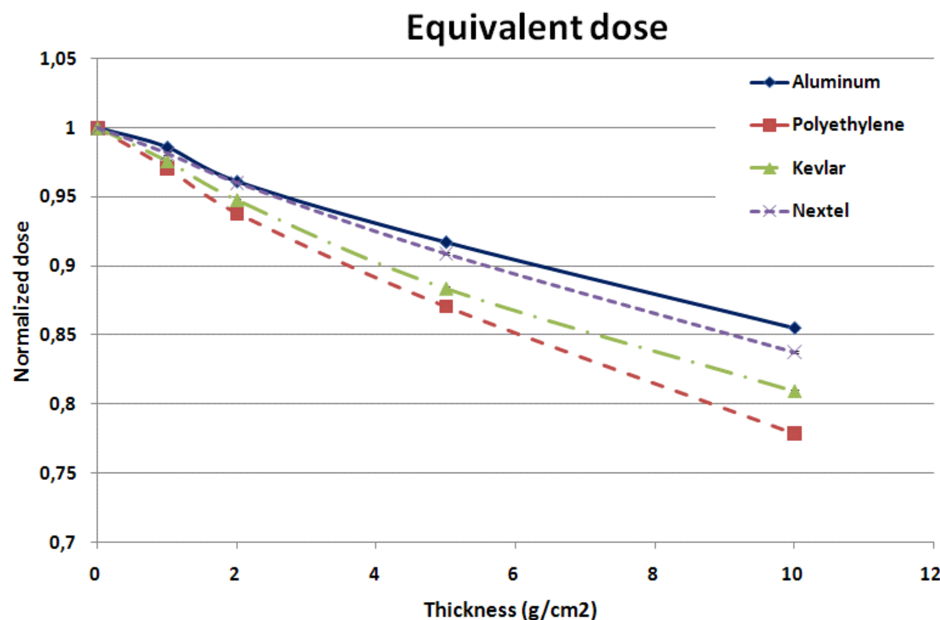

Figure 37: Calculated equivalent dose vs shielding thicknesses for aluminum, polyethylene, Kevlar and Nextel [108]

For this motivation different techniques has been put in place. Radiation-hardened technology is often characterized as technology in which the manufacturer has taken specific steps (i.e., controls) in materials, process, and design to improve the radiation hardness of a commercial technology. Consider the case of CMOS technology, whose low power and voltage requirements make it a popular candidate for space applications. The most likely failure mechanism for CMOS devices resulting from TID is a loss of isolation caused by parasitic leakage paths between the source and drain of the device. For

improved TID hardness, changes in the isolation structure may be required, i.e. a heavily-doped region or "guardband" can be formed by ion implantation that effectively shuts off radiation-induced parasitic leakage paths. In addition, a low thermal budget and minimum hydrogen during processing has been found to improve TID hardness. The use of oversized transistors and feedback resistors, capacitors, or transistors can be implemented for improved SEE immunity. For improved latchup and transient immunity, the change can sometimes be as simple as using of a thin epitaxial substrate. Silicon on Insulator (SOI) technology that employs an active device layer built on an insulating substrate can (with proper design) provide significant improvement in SEE and transient tolerance. In particular, Fully Depleted SOI attested to be 6 times more resilient than bulk to heavy-ion induced SEU[17], [76].

There are also several design approaches that can be used to increase radiation hardness[38], [56] . One global design change is the conversion of dynamic circuitry to full static operation, thereby placing data in a more stable configuration that is less susceptible to the perturbing effects of radiation. For TID, n-channel transistors can be designed in "closed" geometry that shuts off parasitic leakage paths. For SEU, memory cells with additional transistors can provide redundancy and error-correction coding (ECC) to identify and correct errors. Design approaches for improved radiation hardness generally result in a performance and layout area penalty [107] [106] [89]. Unless specific steps such as these are taken during the design and manufacture of a device, radiation hardness levels are typically low and variable. For example, unhardened CMOS SRAMs may experience upsets at a rate of 10^{-5} to 10^{-3} errors/(bit-day), which represents an upset every hour for a satellite with a large memory element in low-Earth orbit that passes through the South Atlantic Anomaly, an area of exceptionally high proton density that overlies much of South America and the South Atlantic Ocean.

2.10 Irradiation Testing and testing simulator

Since sending devices into space has exorbitant costs and is part of missions with multi-year preparation, it is necessary to be able to qualify the devices before sending them into orbit. Therefore, radiation hardness assurance programs supported by various means are therefore essential to ensure the achievement of the mission objectives.

2.10.1 CubeSat

One of the solution could be to embed the circuit to test on board of a Cubesat. Cubesat are quite recent standard conceived to develop a quick and cost effective solution to reduce the development time, to make space accessible to universities and research institutes. Nowadays they are being used by Space Agencies and companies all around the word. In

fact, small satellites are a cost-effective way to test new concepts for Earth observation and the upcoming satellite federations. The limit with this kind of means is that they are in LEO so the amount of radiations is limited and cannot be accounted as per Lunar or deeper space mission.

2.10.2 Irradiation facilities

Artificial irradiation environment such as irradiation facilities make possible to recreate a rich radioactive background with relatively affordable costs. For this reason they are the most used solution.

- TID testing: ^{60}Co sources are the most frequently used ones and have become de facto standard. Their use for hardness assurance testing is primarily based on historical practice, convenience and low irradiation costs rather than on technical grounds. Most of the time, they are employed to simulate electron-rich environments even though it may overestimate the total dose degradation in proton-rich environments. Gamma radiation testing may therefore be considered as a conservative radiation testing source, even if also protons can serve to the same aim [31]. It is important to highlight that TID is a bias dependent effect, whereby all the other effects are not.

- SEE ans SEU Testing: successful modeling and analysis of semiconductor devices' response to heavy ion irradiation relies on the ability to quantify the charge generated in the active regions of the devices and circuits. Protons and heavy ions are used to induce this kind of effects. Among the facilities, in this study we worked with the Université Catholique de Louvain (UCL), a CNES partner which offers various irradiation cocktail: Heavy Irradiation Facility (HIF), Light Ion Facility (LIF). Additionally it also features protons at energy ranging between 10 MeV and 65 MeV[11]. SEE; SEU, SEL and SEFI can be simulated also using Laser Beams, depending on the kind of technology under test. Fig. 45 shows the vacuum chambre to measure the response of electronic components to single event effects.

- DDD and NIEL Testing: protons and neutrons are generally used for inducing this effect. Device can be irradiated unbiased at room temperature.

Figure 38: Vacuum-Chambre at Université Catholique de Louvain (UCL) irradiation facility.

2.10.3 Irradiation simulation

Since the Radiation campaign described above have a significant cost, a good and cheaper alternative is represented by sophisticated simulations.

2.10.3.1 Stop and Range of Ions in Matter (SRIM) Software

SRIM is a collection of software packages which calculate many features of the transport of ions in matter. The SRIM (formerly TRIM) Monte Carlo simulation code is widely used to compute a number of parameters relevant to ion beam implantation and ion beam

processing of materials. It also has the capability to compute a common radiation damage exposure unit known as atomic displacements per atom (dpa)[112]. Typical applications include:

- Ion Stopping and Range in Targets: Most aspects of the energy loss of ions in matter are calculated in SRIM, the Stopping and Range of Ions in Matter. SRIM includes quick calculations which produce tables of stopping powers, range and straggling distributions for any ion at any energy in any elemental target. More elaborated calculations include targets with complex multi-layer configurations.
- Ion Implantation: Ion beams are used to modify samples by injecting atoms to change the target chemical and electronic properties. The ion beam also causes damage to solid targets by atom displacement. Most of the kinetic effect associated with the physics of this kind of interactions are found in the SRIM package.
- Sputtering: The ion beam may knock out target atoms, a process called ion sputtering. The calculation of sputtering, by any ion at any energy, is included in the SRIM package.
- Ion Transmission: Ion beams can be followed through mixed gas/solid target layers, that occurs in ionization chambers or in energy degrader blocks used to reduce ion beam energies.
- Ion Beam Therapy: Ion beams are widely used in medical therapy, especially in radiation oncology

2.10.3.2 OMERE

Omere is free software dedicated to the space environment and effects of radiation on electronic component. Developed by TRAD company with the support of CNES, OMERE calculates the space environment and the effects of radiation on electronics in terms of dose, atomic displacement, singular effect, and solar cell degradation. The effects of radiation can be directly determined by OMERE:

- calculation of dose curves for TID analyses
- equivalent displacement curve for the non-ionizing dose for all materials
- singular event rate calculations based on fitting (Weibul function) parameters

2.10.3.3 FASTRAD

FASTRAD is a complete engineering software developed by TRAD company for 3D radiation shielding analyses.

The radiation analysis engine of FASTRAD includes complementary calculation modules:

- a ray-tracing tool for fast radiation calculation (sector analysis),
- a Monte Carlo algorithm for realistic transport computation. This module has been developed in partnership with the CNES.

The physical interactions taken into account are: multiple scattering, ionization, photon creation, photoelectric effect, Compton diffusion and materialization. The forward Monte Carlo computes the transport of particles from the source to their total energy loss (inside the model limits). Secondary particles created by physical interaction are also tracked; Fig. 39 shows a 3D view of the irradiation calculation.

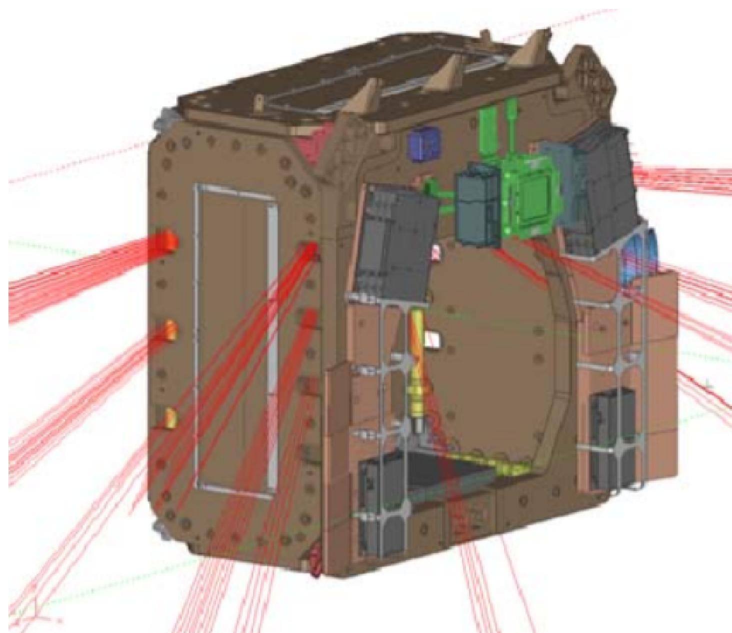

Figure 39: FASTRAD 3D view of a ray-tracing calculation. The rays display the location of the thinnest parts of the model [99]

2.10.3.4 TRADCARE®

TRADCARE® is an engineering tool developed by TRAD and CNES which allows SEE, SET, SEU and SEL prediction. It is based on Graphic Data System (GDS) geometry file, material properties and layer thicknesses which allow to create a 3 D representation of the device. Fig. 40 shows the 3D model generation.

Geant4 toolkit, a multi-physics SEE prediction chain based on Monte Carlo simulation capability, was implemented in TRADCARE® software [2]. The physics selected for the secondary production during irradiation simulation is the hadronic Bertini cascade model [122] exported from Monte Carlo Geant4 tool. The irradiation condition can be settled with high accuracy (particle type, angle of incidence, beam diameter and position) so that

after the irradiation a map of the most sensitive circuit's area is available as shown in Fig. 41

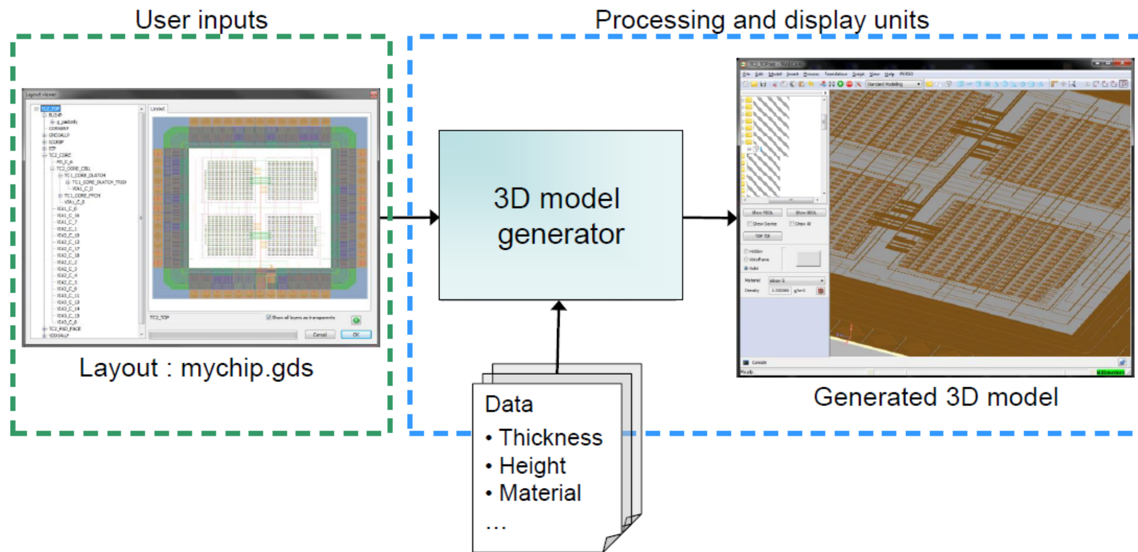

Figure 40: TRADCARE® 3D device model generation.

The tool has some functionalities still under development/ beta testing. In this study, for the first time, it will be used to carried out irradiation simulation on the spintronic devices.

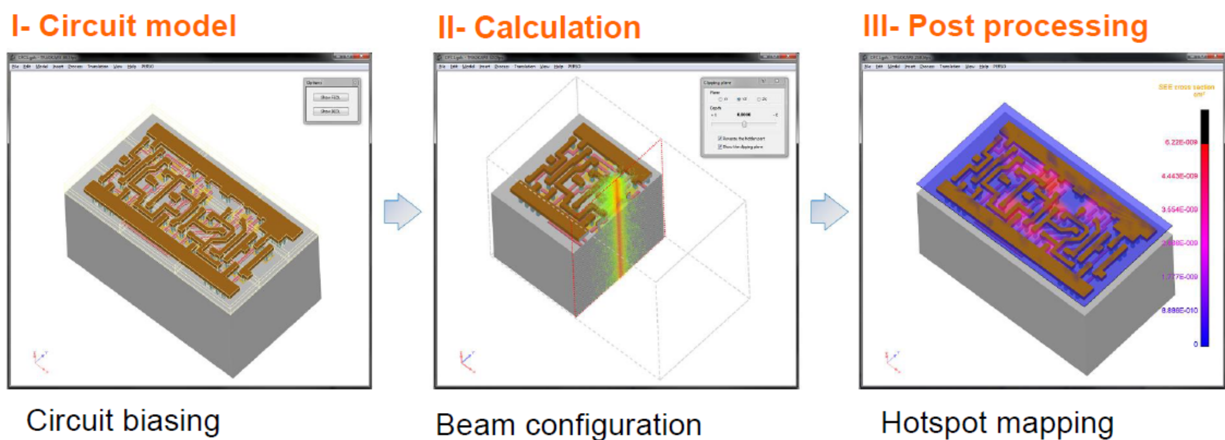

Figure 41: The step of the TRADCARE® simulation flow .

2.11 Conclusion

In this chapter we have reviewed the main space environment features and its various radiation sources. Fig. 45 sums up the effects that these radiation sources could have on electronics devices. We saw also that shielding has important limitations and it has demonstrated to be useless above certain energy. In order to have successful, cost-effective designs and implement new space technologies, the climatology must be understood and

accurately modeled. Underestimating radiation levels leads to excessive risk and can result in degraded system performance and loss of mission lifetime. Overestimating radiation levels can lead to excessive shielding, reduced payloads, over-design and increased cost.

Hardening by design technique using redundancy usually imply huge area and power overhead. Moreover, a technology can show an excellent radiation hardness against certain type of effects, as for example SEE, but in the main time, could be more vulnerable than other to TID. This latter is the case of FDSOI. For this motivation, space industry is looking to new technology solutions as MRAMs which offer a priori higher radiation immunity thanks to their non-charge based storage mechanism as detailed in Chapter I.

Since sending a device in Space is not a viable solution for testing its radiation response, usually the alternative is to perform irradiation campaign in irradiation facility's site. Nevertheless, since they also have a non-negligible cost, in the last years tools that allow to make very accurate simulations have been multiplied, so as to be able to validate the tightness of the circuit to radiation at the design level before it is manufactured, cutting costs considerably.

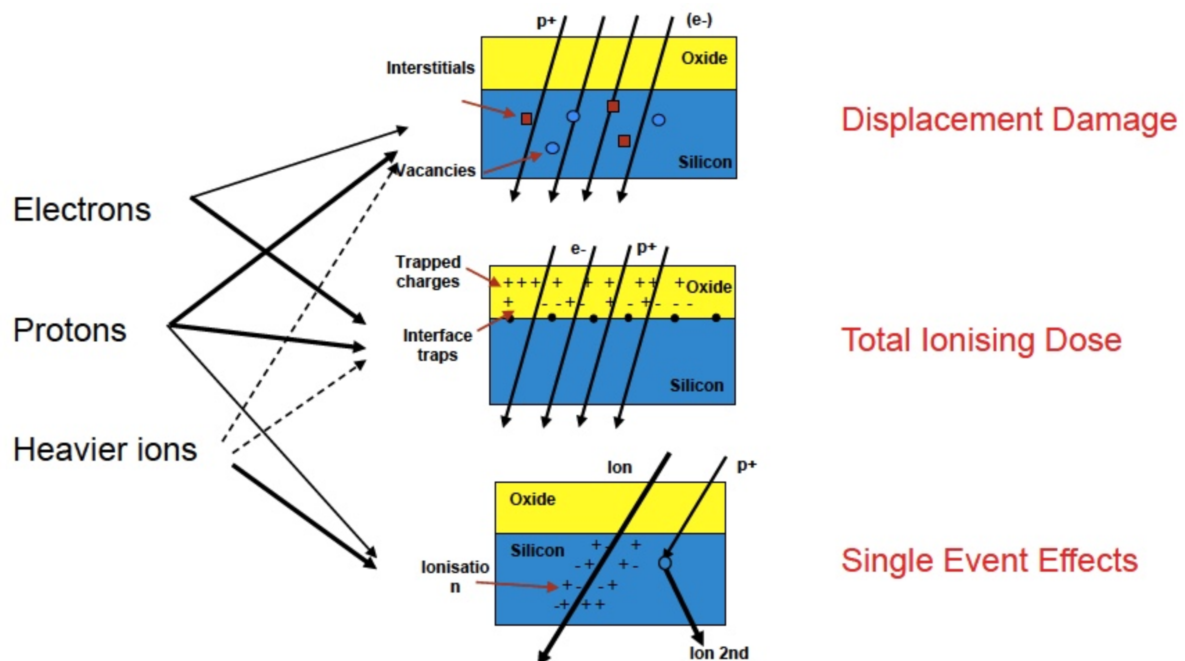

Figure 42: Three main type of effects induced on electronic device by Electrons, Protons and Heavy ions.

Chapter 3

Radiation Hardening by Design

3.1 Introduction

For embedded systems in harsh environments, a radiation robust circuit design is still an open challenge.

As complementary metal oxide semiconductor (CMOS) processes get denser and smaller, their immunity towards particle strikes decreases drastically. Indeed, the relevance of Single Event Transient is growing as technology scales down and operating frequencies go up. Selection of the radiation hardening methods depends on many factors, including the area penalty that can be tolerated or the robustness required.

Several design solutions have been proposed mainly based on hardware redundancy. Triple Modular Redundancy (TMR) approach is the widely used fault tolerant technique that belongs to this family. The concept of TMR relies on three identical copies of the circuit processing data and a majority voter unit voting the triplicated outputs to mask single faults in one of the copies. In [30] redundant feedback lines are used to mask the effects of SEUs. A similar idea is behind the use of SEU-tolerant flip-flop in [38] and the robust latch as proposed in [56]. The main shortcomings of these solutions are the silicon area overhead which implies higher cost and power consumption. As an alternative, a family of techniques based on time redundancy had been developed. SET filter can mitigate SET effects by sampling the input at different time instant by means of a voter. Also other works combine hardware and time redundancy with the aim to achieve higher tolerance to SET. These radiation hardening techniques are presented in [107] [106] [89]. However all these approaches suffer from two important limitations:

- The inborn vulnerability of bulk technology to radiations
- The crucial importance of the voter element.

Indeed, besides beeing the most important part of these technique implementation, the voter is usually also the most vulnerable as depicted in Fig. 43.

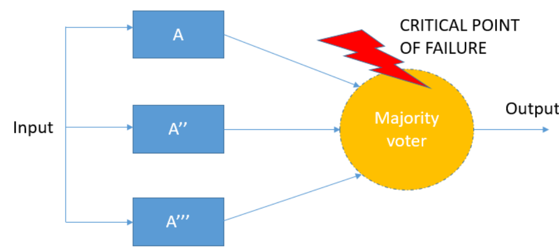

Figure 43: Triple Modular Redundancy (TMR) scheme. The majority voter constitutes the critical point of failure

For this motivation we decide to focus on the design of a SET tolerant C-element circuit combining two important aspects:

- 28 nm FDSOI instead of Bulk technology
- Non Volatile by means of the STT-MTJ and SOT-MTJ.

The scenario of integration of the so designed C-element is a Dual Modular Redundancy (DMR) data path in a regime of asynchronous communications. Fig. 44 gives an overview of the state of the art and of the proposed approaches.

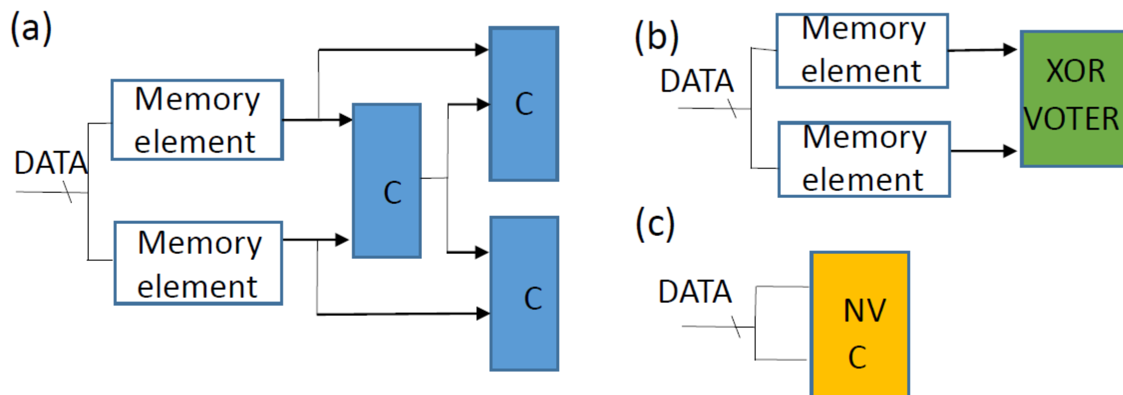

Figure 44: Simplified radiation hardening solutions in [38] [56] (a), [68] (b) and the one proposed in this work (c).

All simulation results presented in this chapter were run with Spectre Electrical simulator under Cadence Analog Design Environment platform and are referred to 40 nm diameter MTJ if not specified differently.

3.2 FDSOI

Silicon on Insulator is a wafer structure consisting of an insulating layer sandwiched between two silicon slices. The insulating material could be Sapphire or silicon Dioxide (SiO_2). Despite its high cost, it is a promising technology mainly in terms of performance gain, estimated to be around 30%. Indeed, the high restive substrate drastically reduces

the leakage current. This same insulating substrate represents an advantage in terms of SET tolerance. Indeed, the SET effect result to be very localized thanks to the possibility of local insulation. Additionally the active area regions are reduced with respect to the Bull technology and this implies less sensitive areas exposed to the possibility of a particle strike. There exist two type of SOI devices: partially depleted (PD-SOI) and fully depleted (FD-SOI). Fig:fer shows the difference between a Silicon on Insulator and a Bulk substrate. It has been demonstrated that FD-SOI are up to 6 times more robust than Bulk to SET [39]. Unfortunately, since there is no silver bullet in the RHBD, this technologt show high sensitivity to TID [125] exactly because of the higher insulator area.

In this work we used 28 nm FD-SOI from ST-Microelectronics.

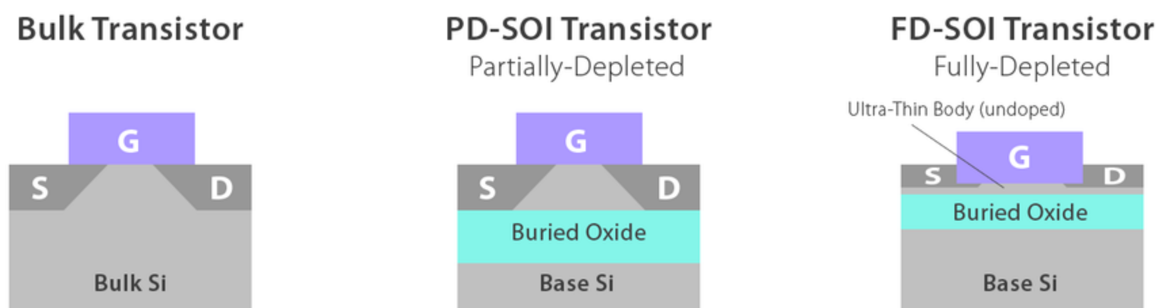

Figure 45: Bulk, PD-SOI and FD-SOI.

3.3 Error model using Cadence Virtuoso

From the view point of the electrical design we simulated the heavy ion impact by means of a well-known way to model the electrical impact of particle strikes [110]. Introduced some decades ago, it is based on current spike injection properly calculated. Indeed, for the heavy-ion induced events, the deposited charge Q can vary from a few to a few hundreds of femto Coulombs. Hence, SETs can be simulated by injecting into the sensitive nodes of the circuit (i.e. the drain of the off transistor for a N type CMOS) a double exponential current pulse [85]. The injected current is expressed by the following equation:

$$I_{inj}(t) = \frac{Q_{inj}}{\tau_f - \tau_r} \times (e^{\frac{-t}{\tau_f}} - e^{\frac{-t}{\tau_r}}) \tag{3.1}$$

Where Q_{inj} is the amount of collected charge and τ_f and τ_r are the fall and rise time constants respectively. Fig. 46 shows the simulated current pulses generated by various particle strikes based on the quantity of deposited charge.

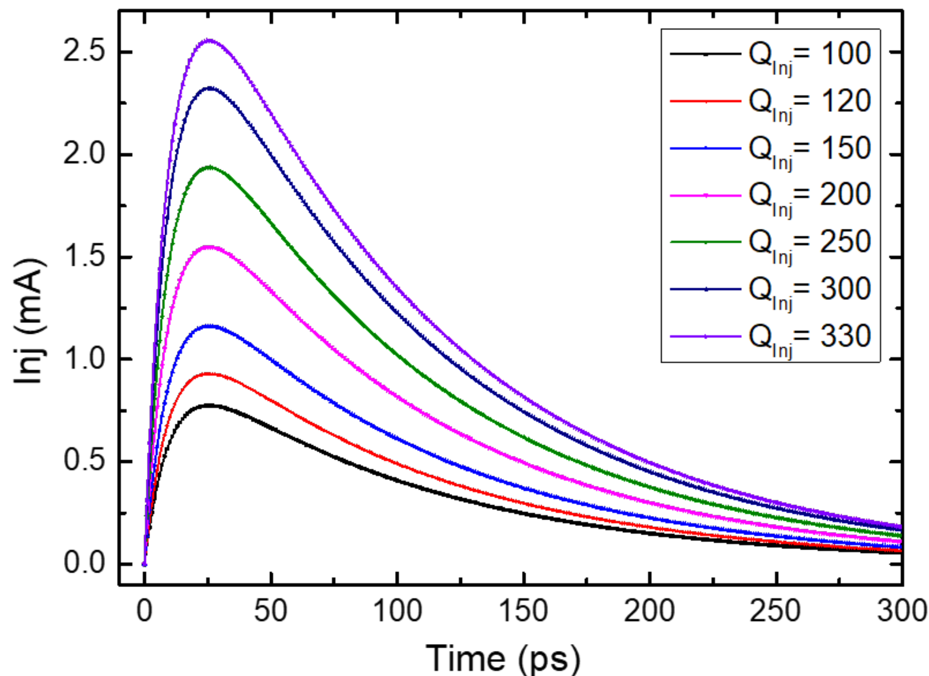

Figure 46: Various particle strike simulation dynamics

3.3.1 Critical charge: considerations on MOSFET parameters dependence

The injected charge depends on the timing parameters of the current pulse according to Equation 3.1. In general, the accumulated charge increases linearly with the increase of the current pulse width. Moreover, the transient current can be enhanced by bipolar amplification due to the parasitic source-body-drain structure. Using the 28 nm FD-SOI technology, we achieved immunity to this phenomenon; as a drawback, aggressive scaling increases the probability of multiple nodes to be affected by one particle strike [69]. In this analysis we injected a double exponential current pulse with a fixed $\tau_r = 10$ ps and a value of $\tau_f = 120$ ps. The dependency of Q_{crit} on transistors width and length has to be taken into account for a robust transistor sizing. Actually, a rigorous definition of critical charge in logic circuit with active feedback is [102]:

$$\begin{aligned} Q_{crit} &= Q_{node} + I_{P,ON} \times \omega_{pulse} \\ &= C_{node} Vdd + I_{P,ON} \times \omega_{pulse} \end{aligned} \tag{3.2}$$

Where C_{node}, proportional to the product between gate length (L) and width (W), is the capacitance of the considered node and $I_{P,ON}$, proportional to the transistor aspect

ratio ($\frac{W}{L}$), is the stabilization current of the pull-up transistors. Thence, the larger the current pulse, the higher the contribution of $I_{P,ON}$. For the chosen τ_f, increasing the transistor width up to 10 times the minimum size allows to increase Q_{crit} by almost a factor of 10.However, this should face area and power consumption trade-off.

Low threshold voltage transistors were employed to guarantee a fast stabilization of the node charge and, therefore, to enhance the advantage of the quenching phenomena in 28 nm FD-SOI, which, by means of the electron-hole recombination, results in a faster decay of the transient.

3.4 C-element

The C-element is a state holding circuit, which is transparent when all its inputs are equal, and holds the previous output otherwise, as reported in Table 3.1 [91].

Table 3.1: Truth Table of the 2-input C-element

Input A	**Input B**	**Output**
0	0	0
0	1	Previous output
1	0	Previous output
1	1	1

There are different implementations, but the Single Inverted Latch SIL-C element was demonstrated to be the less sensitive to fault injection due to the reduced number of sensitive nodes and for this reason it was chosen for this study.Fig. 51 shows its circuit implementation. In [30] they propose to use 3 C-element in synchronous regime to block a SET propagation as detailed in Fig. 48. In general, in the synchronous word the redundancy techniques leverage a DMR which allow to only detect an error or the TMR to give also the possibility to correct a detected mismatch.

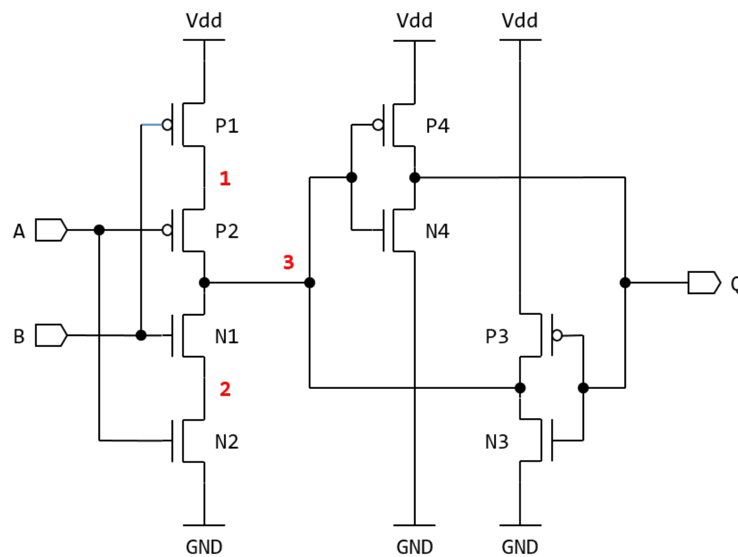

Figure 47: Single Inverted Latch implementation of the C-element. The numbers in the circuit represent the sensitive nodes.

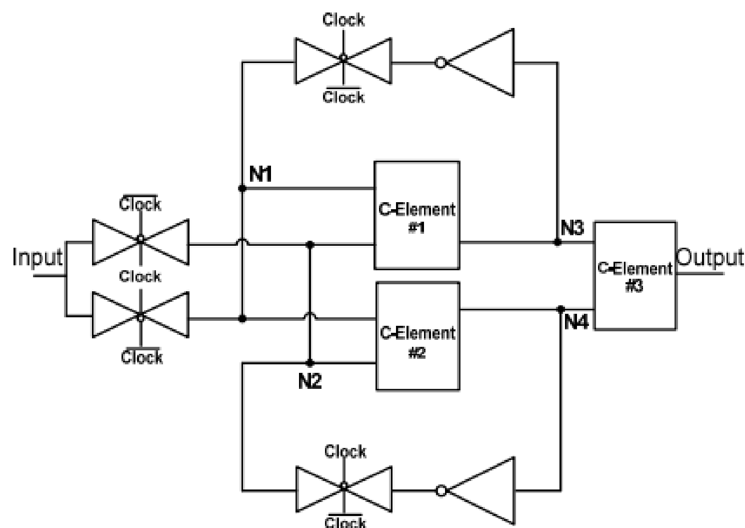

Figure 48: The proposed SEU tolerant latch in [30]

In contrast to this approach, a DMR asynchronous solution is presented in [79] where the use of Non-Volatile memory elements and asynchronous protocol allow error detection and correction at each stage of a pipeline. Fig. 49 details this solution. To reduce the Silicon footprint and power consumption of this solution we proposed to use, instead of NV flip-flop, a C-element, which rendered Non-Volatile, enables logic in memory functions and do not need to be duplicated (as the NV flip-flop does). This way the number of sensitive nodes is also reduced hence we aim to obtain a less vulnerable circuit.

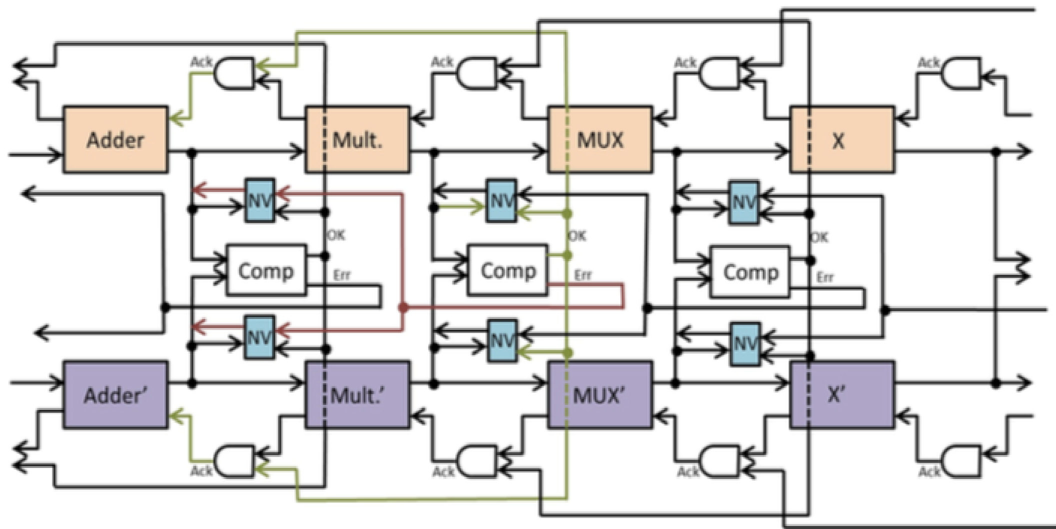

Figure 49: Proposed solution in [79].

Indeed, if the previous approach need an external memory element and a circuit able to highlight a mismatch (the XOR or the Muller gate), the proposed solution, on the contrary, integrates both the memory element and the Muller cell into a single circuit. The memory capability is ensured by means of STT-MTJs. Hence, the proposed circuit receives as input the data path and its duplication as illustrated by Fig. 50. It blocks a mismatch propagation (second and third lines of Table 3.1 or allows the correct bit propagation (first and fourth lines of Table 3.1). In the context of a multi-stage asynchronous micro-pipeline, it also allows one to restore the correct bit from previous stages. This behaviour is ensured by the C-element that stores the right value (and its complement) inside the STT-MTJs as will be detailed in Section 3.5.4.

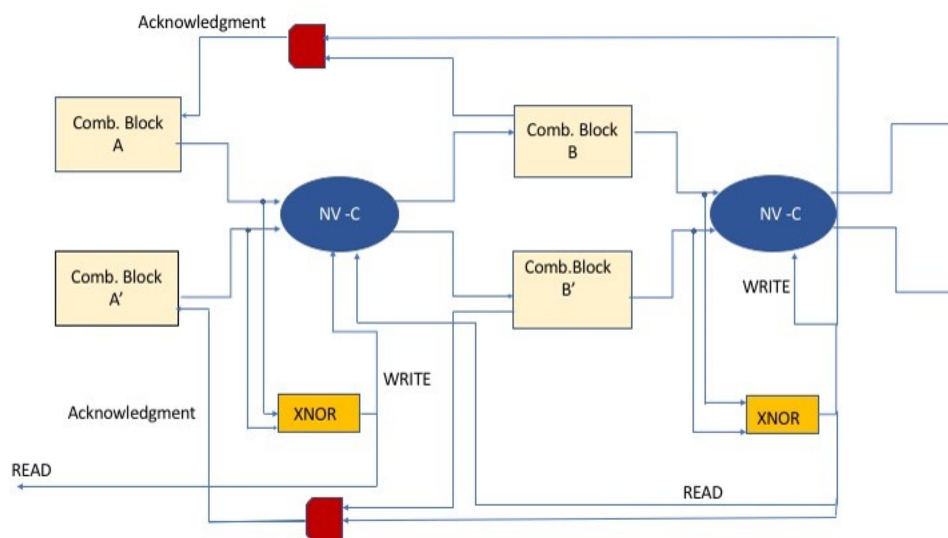

Figure 50: Solution proposed in this work, leveraging a SET tolerant NV-C element.

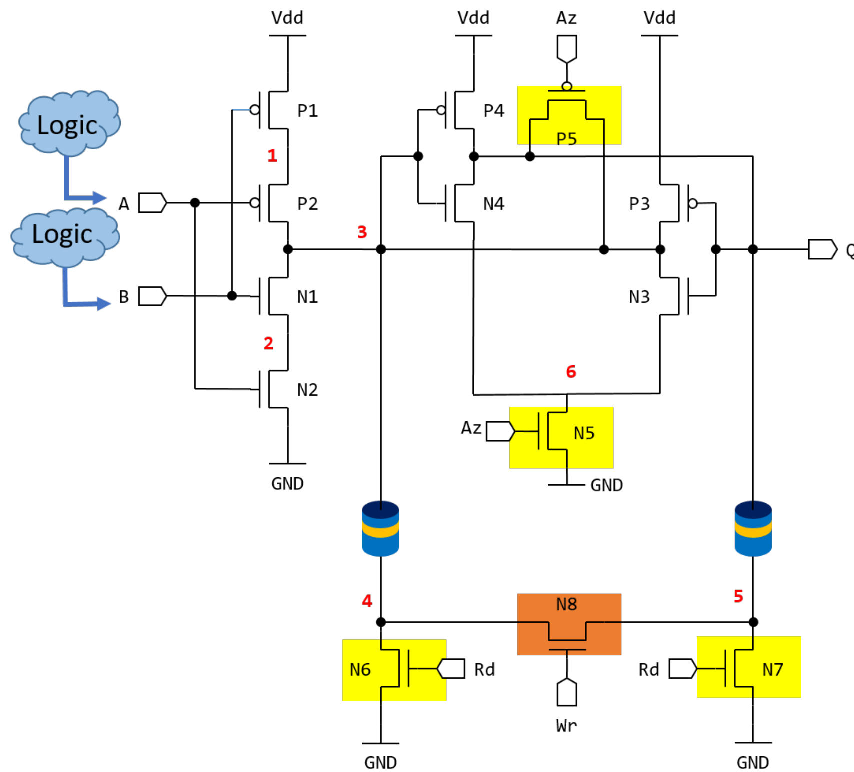

Figure 51: Proposed radiation tolerant Non-Volatile implementation of the C-element. The numbers in the circuit represent the sensitive nodes.

3.5 Proposed Novel Circuit

In the proposed circuit, MTJs are used to store the output state and its complement while the CMOS part takes charge of the combinational operations. Among the various Muller cell implementations, the Single Inverter Latch (SIL) C-element has been chosen, since it was already demonstrated to be the most soft-error resilient [57].

At first, we propose to make the C-element non-volatile: two MTJs and five transistors are used for this purpose, as depicted in Fig. 51. The circuit level implementation consists of pull-up transistors (P1, P2), pull-down transistors (N1, N2), an inverter (P4, N4) and a weak inverter (P3, N3). Read operations (involving N5, N6, N7 and P5) are achieved by equalizing the voltage of the output node (Q) and node 3 by means of Az signal. Hence, sensing the value of the MTJs resistance (Rd signal) exploiting the Tunnel Magnetoresistance (TMR) effect [77].

To perform a write operation, a bipolar current pulse is generated by driving the gate signal of N8 to logic level high. This current pulse must have the appropriate amplitude and width to switch the orientation of the MTJ's free layer, namely it has to be above the minimum switching required current (critical current, I_c)already defined in Chapter I. Design and simulation results presented in this chapter were run with Spectre Electrical Simulator, under Cadence Analog Design Environment platform, using the 28 nm FD-SOI technology PDK from STMicroelectronics. The Supply Voltage was fixed at 1 V.

Concerning the STT-MTJ cells, a physics-based 40 nm perpendicular MTJ compact model described in Verilog A has been used [52]. This model originates from the framework of Julliers' model, Brinkman's model and Simmon's model with an analytical approach and along with some important approximations. In fact, the MTJ switching thresholds are derived from linearization of Landau-Lifshitz-Gilbert (LLG) equations around the stability points. The conductance of the MTJ varies with the bias voltage applied across the device and with temperature. Moreover, as a basic assumption, the magnetization of each FM layer is considered uniform. Monte Carlo simulations at different corners have been run to validate the functional operations of the cell against process, voltage and temperature (PVT) variations for the CMOS part, and resistance-area product, critical current and TMR variations for the MTJ components. Table 3.2 shows the default STT parameters in the considered MTJ compact model.

3.5.1 Robustness evaluation

The STT compact model was calibrated with the parameter's values listed in Table 3.2. Errors were injected into the sensitive nodes of the proposed circuit (numbered from 1 to 6 in Fig. 51). Simulation results can be summarized as follows:

- SET at node 1 or node 2 will not affect the output of the C-element; only a simultaneous hit of both will inevitably affect the output computation.
- Since Az signal is normally high, a strike at node 6 could lead to a transient disturbance only during sensing operation (N5 off). Using wider windows of activation for both Az and Rd signals reduces the probability for this event to affect the read operation. An enhancement of the MTJ reading reliability could also be achieved with higher TMR as detailed previously.
- A hit at node 3, the most critical node of the volatile part, leads directly to a transient on the output. Even so, as detailed in Fig. 52, Q quickly recovers its value in a time, referred to the recovery time, ranging from 250 ns to 350 ns for an injected charge varying from 100 fC to 330 fC, respectively.
- Both node 4 and node 5 are the most critical for the NV-part. In order to test their behaviour when an SET occurs, the protection transistors N9 and N10 have been disconnected in this first step. A charge of 100 fC has been injected on the drain of the read/write off transistors. As a result, a current above the critical value flows through the MTJ, reversing its memory state. Therefore, this SET induced a non-volatile SEU, compromising the stored data reliability. Then, we keep increasing the injected charge to evaluate how the output node, Q, is affected. Actually, the occurrence of NV errors in MTJs and SEEs on the output node are quite independent.

Still up to $Q_{inj} = 240$ fC in node 4, the output of the circuit (Q) quickly recovers from the SET, so that the non-volatile error occurs even if the output of the circuit is correct (Fig. 53). Despite this, it is not acceptable to maintain an incorrect stored data in the memory part of the circuit. The same amount of charge, injected at node 5, results in a NV error and also in a SEU on Q node (Fig. 54): this is easily understandable since the affected node is closer to node Q than node 4. In both transient simulations, the current induced in the MTJ in parallel state (storing the bit "0") is higher with respect to the current induced in the antiparallel state, precisely because of the lower value of its resistance. This is noticeable in Fig. 53 by observing the transient current peak on MTJ's free layer. This should not be confused with the fact that, the switching energy is lower for AP→ P than for P→ AP, as it is well known from Spin Transfer Torque theory [8].

Table 3.2: Default STT parameters in the p-MTJ compact model

Parameter	**Description**	**Value**
Area	MTJ surface	20 nm ×20 nm
TMR(0)	TMR with 0 V_{bias}	1.5
E_{bd}	Breakdown electric field	0.8 V/nm
R_p	Parallel resistance	1 kΩ
RA	Resistance area product	1.5 $\Omega\mu m^2$
Ic0	Minimum switching current	50 μA
t_{ox}	Oxide thickness	0.8 nm
P	Polarization of the free layer	0.65

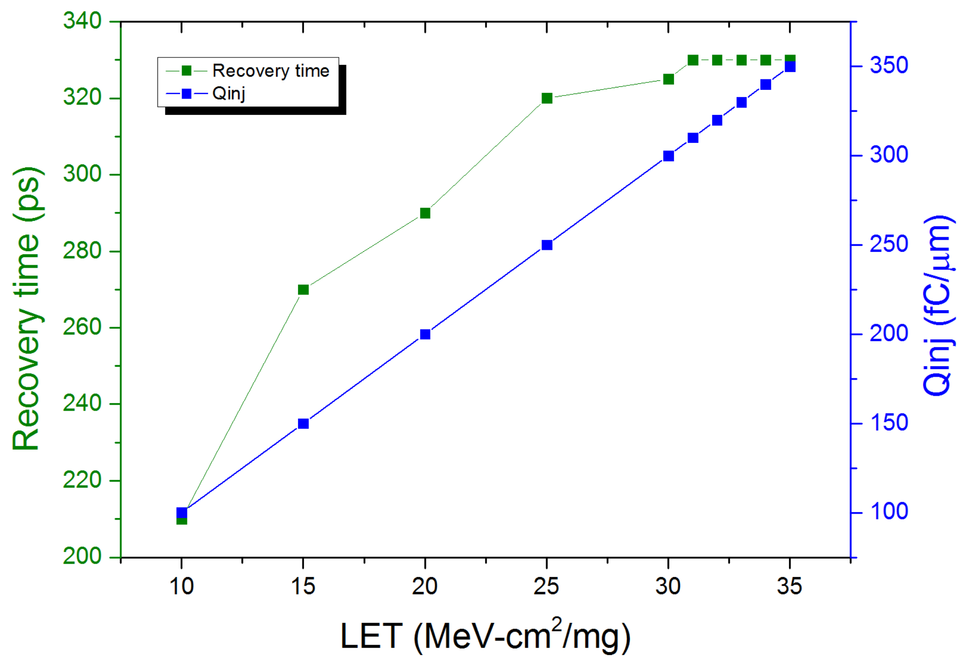

Figure 52: Recovery time at node 3 after a particle strike with different linear energy transfer (LET) values.

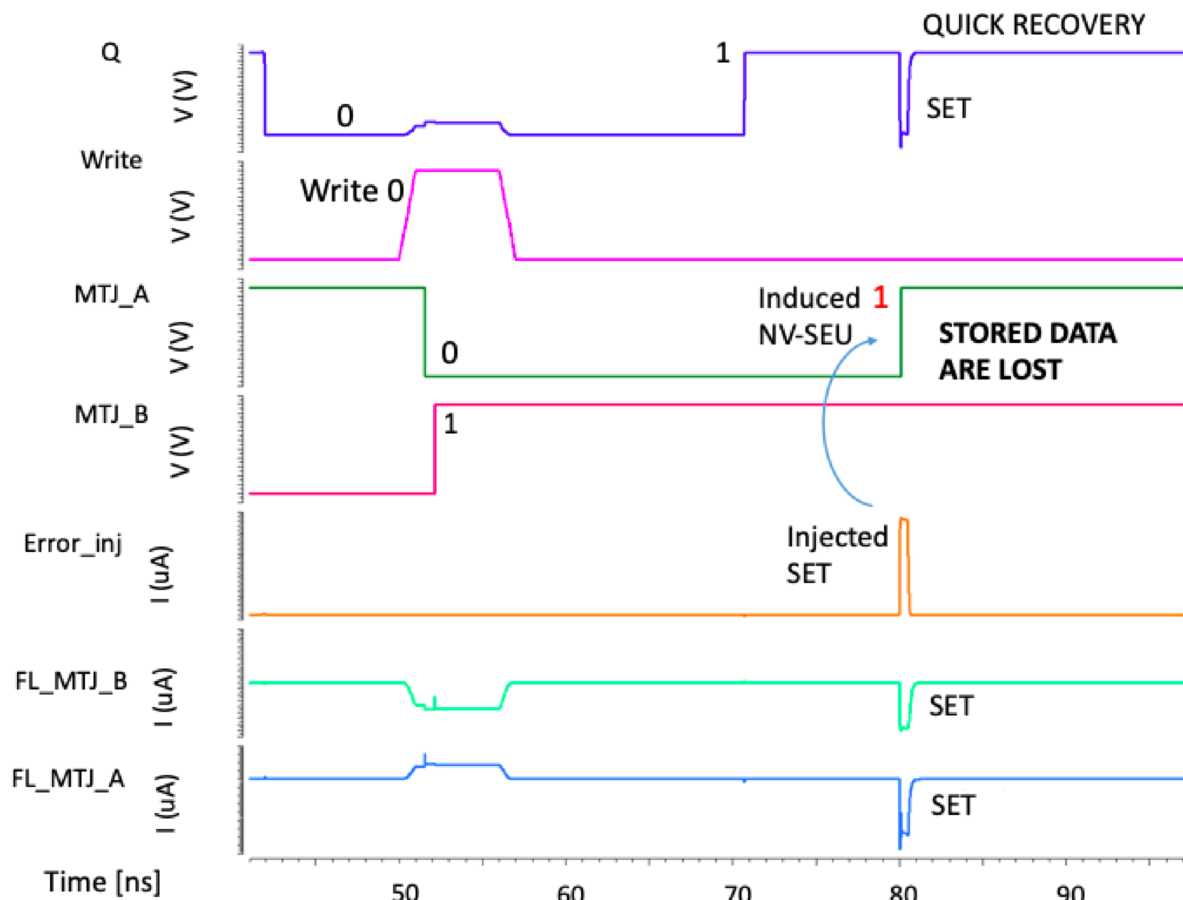

Figure 53: Transient simulation waveforms of the Non-Volatile C-element when Q_{inj} = 240 fC in node 4.

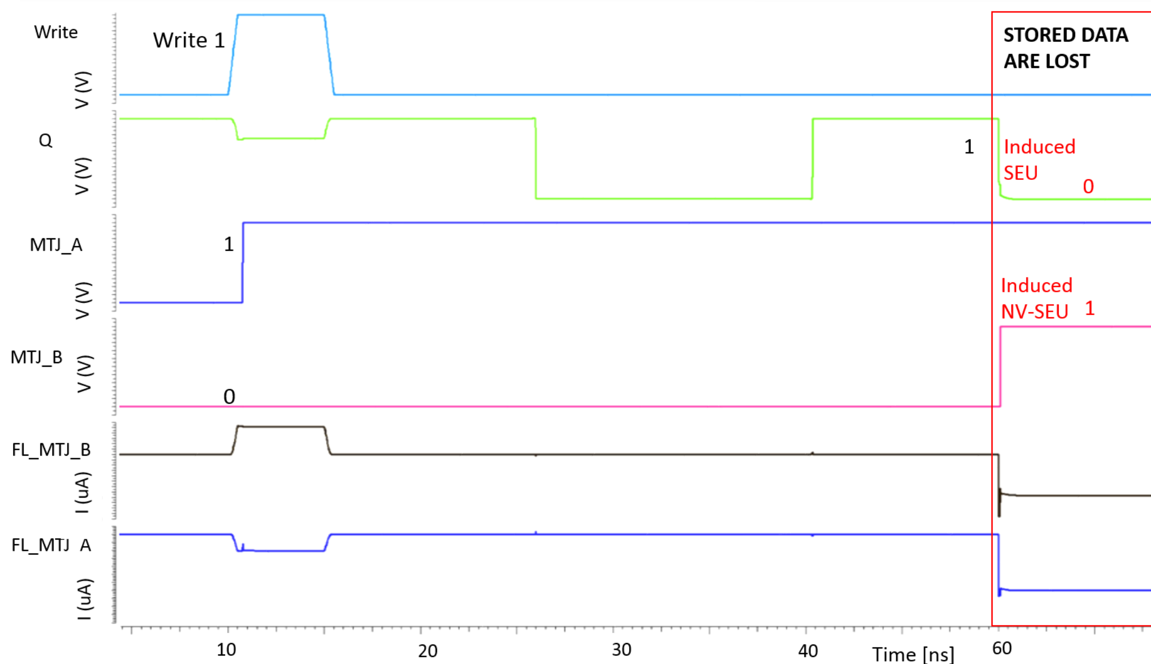

Figure 54: Transient simulation waveforms of the Non-Volatile C-element when Q_{inj} = 240 fC in node 5.

3.5.2 Radiation hardening enhancement

Since current peaks induced on the drain are usually intense and narrow [40], two different strategies are pursued: on the one hand minimizing the probability of a NV upset induced by the strike, $P(t_{strike})$, by making it more difficult to upset the FL; on the other hand, reducing as much as possible the current, induced by an upset, flowing though the MTJs. The latter is achieved by activating, during the standby window (i.e. when neither a write nor a read operation have to be performed), two transistors providing a shunt path for the current, which will act as a protection for the stored data.

3.5.2.1 Impact of MTJ parameters on radiation hardening

- Resistance-area product (RA):

  According to [8], the switching probability during a sub-critical current pulse is given by:

$$P(t_{strike}) = 1 - exp(-\frac{t_{strike}}{\tau_{switch}}) \tag{3.3}$$

  Where t_{strike} is the duration of the current induced by the upset, and τ_{switch} is the mean time needed to switch the MTJ's free layer orientation. Immediately following from Equation 4.4, a way to minimize the $P(t_{strike})$ is to increase τ_{switch}. This could

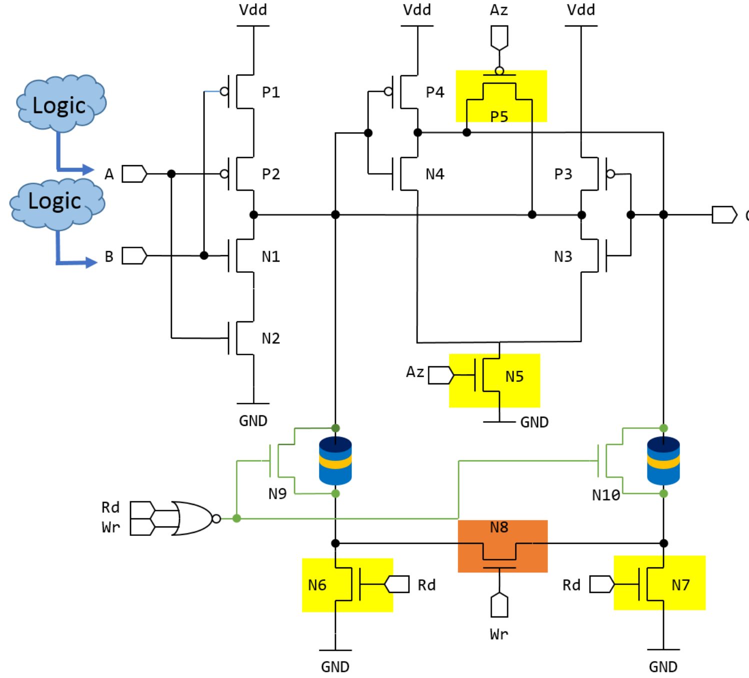

Figure 55: Enhanced proposed radiation tolerant Non-Volatile implementation of the C-element.

be done by increasing the RA parameter [109], [126] and evaluating the impact on the other STT-metrics:

$$RA \propto exp(-\frac{4\pi t_{ox}\sqrt{2m\phi}}{h}) \tag{3.4}$$

Where h is the Planck constant, ϕ the barrier potential height and m the effective mass of the electron. At first, it should be noticed that the increase of RA is exponentially related to the increase of oxide thickness. The role of the tunnel barrier thickness is crucial to enhance radiation tolerance: the thicker t_{ox}, the higher the breakdown energy of the MgO, thus the more robust to radiations the MTJ. Nevertheless, a particular attention must be given to the growing of t_{ox}, which makes it more difficult to upset but also increases the resistance of the magnetic device. Clearly, this could lead to the failure of standard writing operations. Moreover, due to the limited length of spin relaxation, the MgO thickness has to be thin enough to ensure the electron tunnelling possibility [126]. In addition, the reliability of reading operations has to be increased. For this reason, the increase of RA has a good impact because it leads to a linear increment of the TMR. This relation was proven experimentally and is valid in the region below RA values of 10 Ω μm^2.

- Thickness (volume) of the free layer:

Following Eq. 1.5 and Eq. 1.6 (Chapter I), this parameter is directly involved in the critical current definition. By increasing the free layer volume (or thickness since a

constant MTJ diameter is considered), more current would be needed to switch the magnetization of the FL, thus the critical current increases. As a result, $P(t_{strike})$ is lowered; as a drawback, the write energy is increased.

Increasing the free layer volume leads to higher thermal stability, as described by Eq. 1.5. This has a beneficial effect on the retention time and on the radiation tolerance, since data stored are less sensitive to the thermal and energy fluctuations [8].

- Size:

  In this analysis, the MTJ's area is kept constant with the aim to investigate the radiation tolerance of scaled MTJ integrated in a 28 nm FD-SOI technology. Thus, a radius of 20 nm is kept constant in this design.

Table 3.3 summarizes the effect of the considered parameters on $P(t_{strike})$ and the write energy. Interestingly enough, these last two metrics have opposite trends, suggesting that high MTJ robustness and low write energy cannot be achieved at the same time. Since the proposed circuit was conceived in such a way that a reduced number of write operations have to be accomplished, this penalty has less impact than in the other proposed design [68]. In conclusion, by taking into account these observations a new setup, suitable for radiation hardening purpose, is used to calibrate the STT model, as detailed in Table 3.4.

Table 3.3: Impact of RA increment on MTJ radiation robustness for MTJ radius = 20 nm

Symbol	Parameter	$P_{MTJ_{upset}}$	Write energy
$R_p \Uparrow$	Parallel resistance	$\Downarrow$	$\Uparrow$
$\tau_{switch} \Uparrow$	Mean time for MTJ switch	$\Downarrow$	$\Uparrow$
TMR $\Uparrow$	Tunnel Magnetoresistance Ratio	$\Downarrow$	-
$E_{barrier} \Uparrow$	Oxide barrier energy	$\Downarrow$	$\Uparrow$
$t_{ox} \Uparrow$	Oxide thickness	$\Updownarrow$	$\Uparrow$
$\Delta \Uparrow$	Thermal stability factor	$\Downarrow$	-
V $\Uparrow$	Volume of the free layer	$\Downarrow$	$\Uparrow$

Table 3.4: Robust setup for STT parameters in the p-MTJ compact model

Parameter	Description	Value
Area	MTJ surface	20 nm 20 nm
TMR(0)	TMR with 0 V_{bias}	2.0
E_{bd}	Breakdown electric field	0.8 V/nm
R_p	Parallel resistance	6.8 k
RA	Resistance area product	8.5 m^2
I_{c0}	Minimum switching current	67 A
t_{ox}	Oxide thickness	1.1 nm
P	Polarization of the free layer	0.71

3.5.2.2 Impact of the shunt path on radiation hardening

As an alternative, a less resistive path is created by the insertion of two NMOS (N9, N10) in parallel to each MTJ as shown in Fig. 55. The key idea is to obtain a resistive shunt path for the current pulse induced by particle strikes. Hence, provided that $R_{on} \ll R_p$, the quantity of current flowing through the MTJs will not be enough to induce their switching. The R_{on} of the NMOS transistor in linear region will vary as:

$$R_{on} = \frac{1}{2K_n(V_{gs} - V_{dt})} \tag{3.5}$$

Where K_n is the electron mobility. Thus, a trade-off between large transistors and robust enhancement is mandatory. After a parametric analysis, a transistor aspect ratio between 8 and 10 has been chosen for the design, in spite of a slight area penalty.

Additionally, to ensure the validity of this solution, the gate signal of N9 and N10 has to be carefully controlled. A NOR gate between the *Read* and *Write* signals ensures that they do not interfere with the standard operations. It acts when N6, N7, N8 are off, so node 4 and node 5 represent exactly the drain of the off NMOS transistor.

Simulation results show that the insertion of the NMOS in parallel to each MTJ increases the circuit robustness to non-volatile errors up to 3 times with respect to the solution without the shunt path, and 1.5 to 3 times with respect to the designs in the state of the art [127, 68, 58, 79]. As highlighted in Fig. 56, after a $Q_{\text{inj}} = 300$ fC in node 4, the output Q quickly regains its original value (it takes around 1 ns in the worst case) and the information stored in the MTJs are not affected at all. Concerning the strike at node 5, the output Q will be reversed as in the non radiation-tolerant version. Nevertheless, since MTJs are not affected, the correct value can be restored as detailed in the next sections.

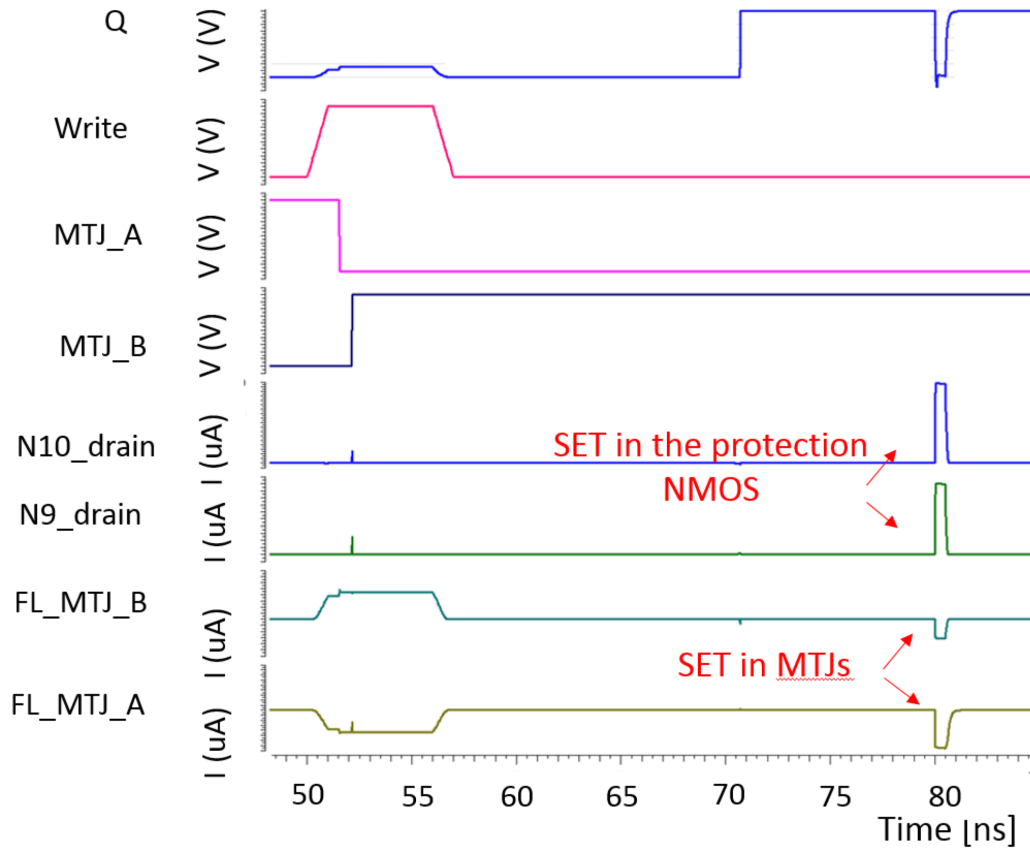

Figure 56: Transient simulation waveforms of the radiation tolerant Non-Volatile C-element when $Q_{inj} = 300$ fC in node 4.

Fig. 57 summarizes the error injection responses in terms of recovery time (duration of the transient on the output of the circuit, Q) and current induced (intensity of the transient) in the parallel state MTJ, by varying the quantity of injected charge. The two NV C-elements, the basic version and the radiation-tolerant one, are then compared in the plot. Starting from 250 fC, the current induced in the parallel state (worst case) of the MTJ is slightly above the critical current value (2 μ A). In spite of this, no bit flip occurs because the transferred energy is not enough to reverse the FL magnetization. This is valid up to ~300 fC when random switching is observed even in the presence of the protection transistors. The radiation-tolerant version of the circuit also leads to a faster recovery time of the output Q (25% faster). This can be explained with the charge recombination process in the inserted protection transistor. Unfortunately, this is not sufficient to cause an increase of the critical charge in node Q.

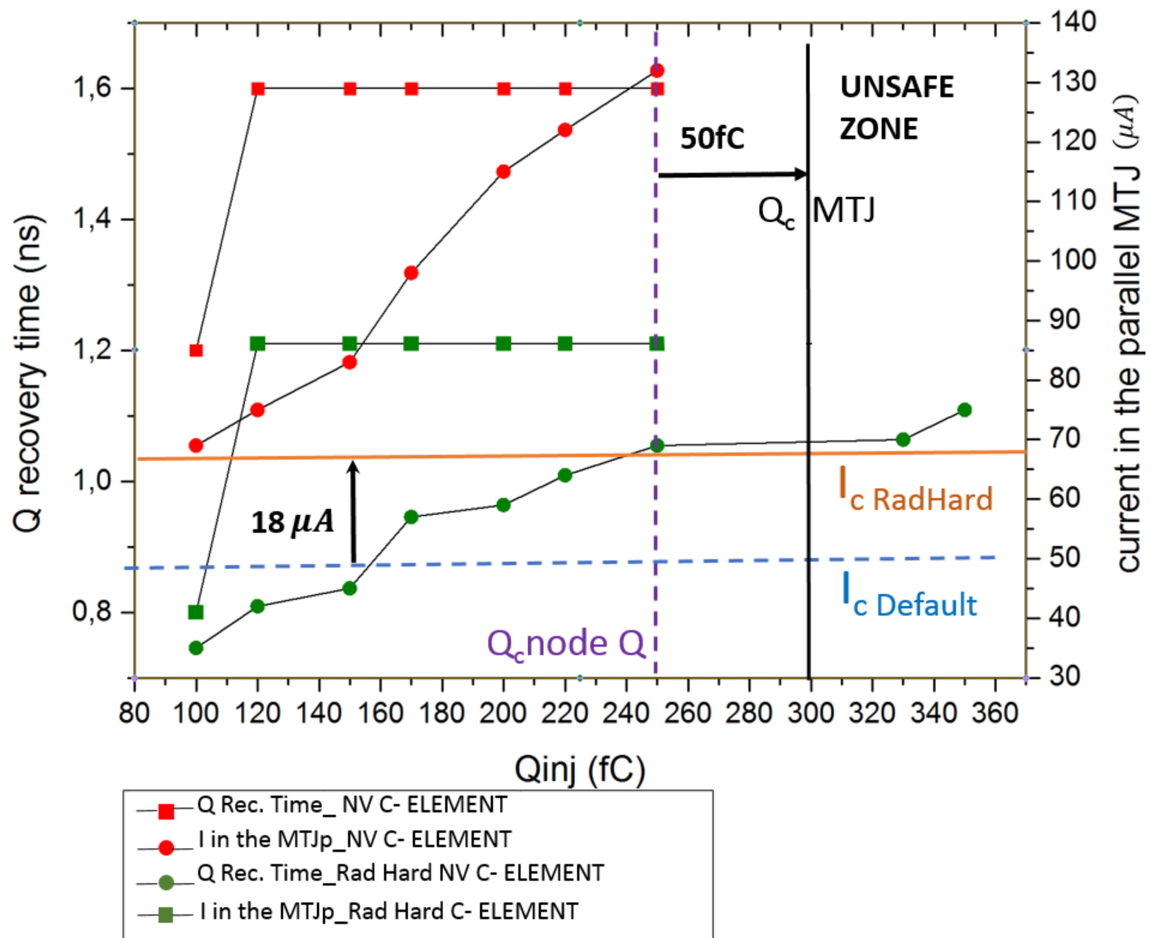

Figure 57: Output recovery time and current peak induced in the parallel MTJ after an SET with different energy values. The radiation hardened version and the basic version are plotted.

We also have to consider that the circuit is still vulnerable to multi-node upset, as noticeable from Fig. 58. Indeed, if several nodes are affected at the same time the output of the N9-N10 control logic can be flipped. In this case, the shunt path would either not be activated (bit flip from “1” to “0”), or activated when it should not (bit flip from “0” to “1”). In this case, reading or writing operation may be concerned. However, this occurance depends meanly on the amount of collected charge, which determines the SET expiration time and thus the vulnerability window.

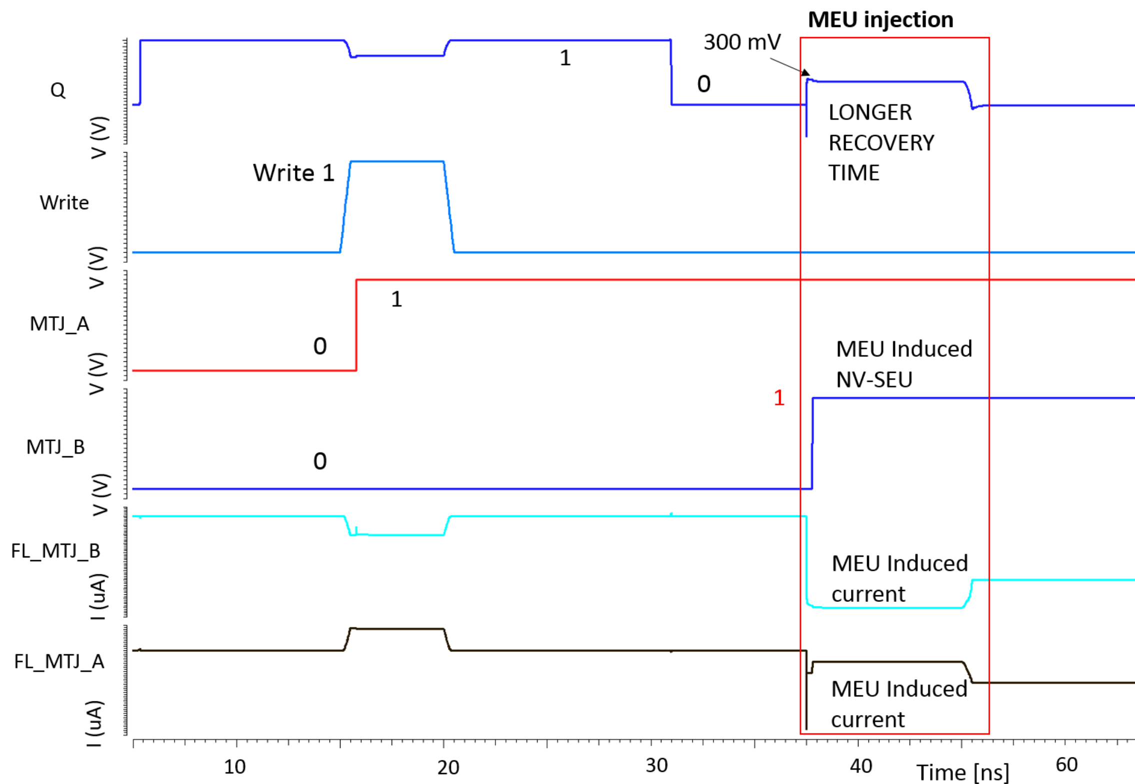

Figure 58: Transient simulation waveforms of the radiation tolerant Non-Volatile C-element when Q_{inj} = 308 fC in node 4 and 5.

3.5.3 Performance evaluation

Fig. 59 compares the non volatile version of the circuit (taken as the baseline), the radiation-tolerant one and solutions from [79] and [18]. It is interesting to notice that, as expected, the main penalty of the robust version is the mean write energy, estimated to be 187 fJ per write operation (mean writing time being 2.8 ns and $I_{c0}67\mu A$, at 1 V). This is due to changes in the MTJ setup in order to achieve higher radiation tolerance. The penalty due to a higher cost for a single write operation is softened by the reduced number of them, as will be further detailed in the next Section. Unlike the other solutions, memory elements and peripheral circuits being merged in the same circuit, area is not a critical metric for this circuit. On the contrary, delay is the major penalty. This is not surprising since, among the existing C-element implementations, the SIL one is the most robust and the slowest. Moreover, an additional delay is added because of the insertion of transistors P5 and N5 in the proposed non-volatile version, since they have to disconnect (connect) the SIL part from (to) GND to allow the MTJ reading operations. However, the main advantage of the proposed solution is the capability of correcting errors due to SEEs along all the sensitive nodes in the C-element and to store, in the same cell, the correct data. The non-volatile errors radiation tolerance is shown to be up to 3 times higher than the other solutions.

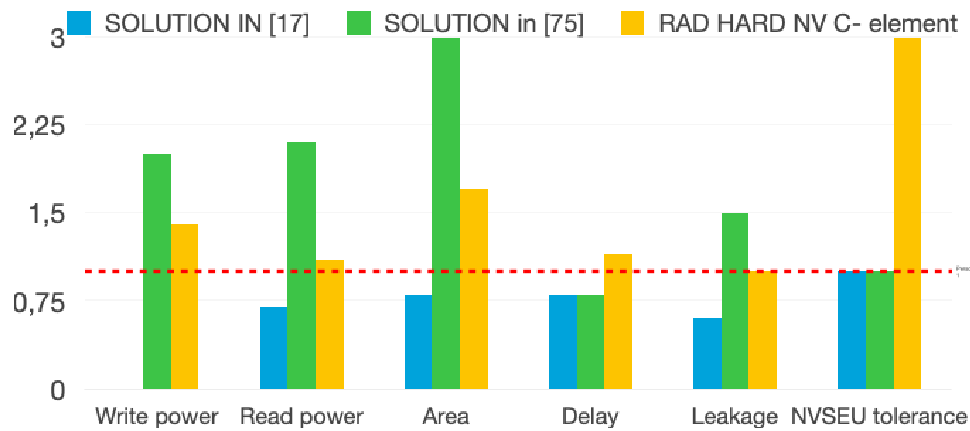

Figure 59: Performances, area and robustness comparison between the proposed solution and the state of the art. The basic version of the NV C-element is assumed as the baseline (red dotted line). Data for solution in [18] refer only to the read circuit.

3.5.4 Asynchronous micropipeline

In this section, a possible radiation hardening scenario is suggested: the use of the proposed NV C-element in an asynchronous DMR micropipeline, as depicted in Fig. 60.

A traditional asynchronous micropipeline is formed in stages. Each stage integrates a half buffer formed of several volatile C-elements. Hence, if the circuit is powered down, the data stored by the various half buffer are lost. The same will happen in case of a reset event. By using the cell presented in this Chapter, the SEEs are mitigated while the immunity to power-off and resets is achieved without the need to duplicate the memory elements. Indeed, if a mismatch between the two data-paths occurs, the error propagation is blocked by the C-element. Write and read operations are handled by an XNOR and inserted in each stage. The write signal is only activated if the inputs of the C-element are equal. Otherwise, the read signal performs the reading of the bit stored in the previous stage, allowing the combinational block to carry out again its operations. Since write operations can occur only if data are correct, their reduced number mitigates the increase of write energy per bit. The output of the XNOR is also sent to an AND gate in charge to propagate the Acknowledgment signal along the return path, with the aim to confirm (output “1”) or not (output “0”) the readiness to receive new data, according to the 4 phases handshake protocol requirements.

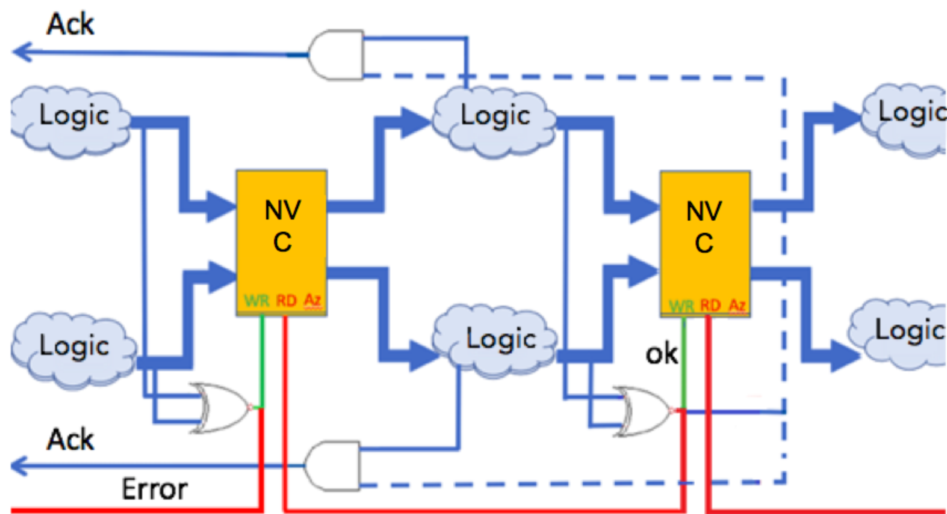

Figure 60: SEEs mitigation in an asynchronous micro-pipeline hardened by means of the proposed Non-Volatile C-element.

3.6 An SOT-STT hybrid model for error electrical injection

In this section we present the design of the C-elment by means of SOT devices. In order to evaluate SOT robustness to electrical fault injection a new compact model have been developed.

3.6.1 SOT NV C-element implementation

Fig. 61 shows the SOT-MTJ implentation of the proposed circuit. The circuit works exactly as the one proposed in the previous section. The only novelty is that, being the SOT-MTJ a three terminals device, two more transistors (N7 and N8) have been added for the reading operations.Unfortunately this lead to an increase of the number of transistors and sensitive nodes in the circuit. However, we pursue a study to evaluate the SOT-MTJ tolerance to fault injections with respect to the STT-MTJ. In order to do so, we needed to develop a new model, since the existing one do not take into account the possibility of writing the MTJ from the reading path by STT effect. Indeed, in normal conditions, with an appropriate control of reading and writing signals this eventuality can not happen. Indeed, the strength point of the SOT is exactly this one, as detailed in Section 1.5.4. Nevertheless, in this context, a fault injection made on purpose on the reading path could generated a current high enough to write the SOT device by leveraging the STT effects in the MTJ pillar. Basically, even if we call the device SOT-MTJ, the possibility of tuning up a spin tranfer torque effect in the nanopillar has to be taken into account, even if reduced compared to STT devices.

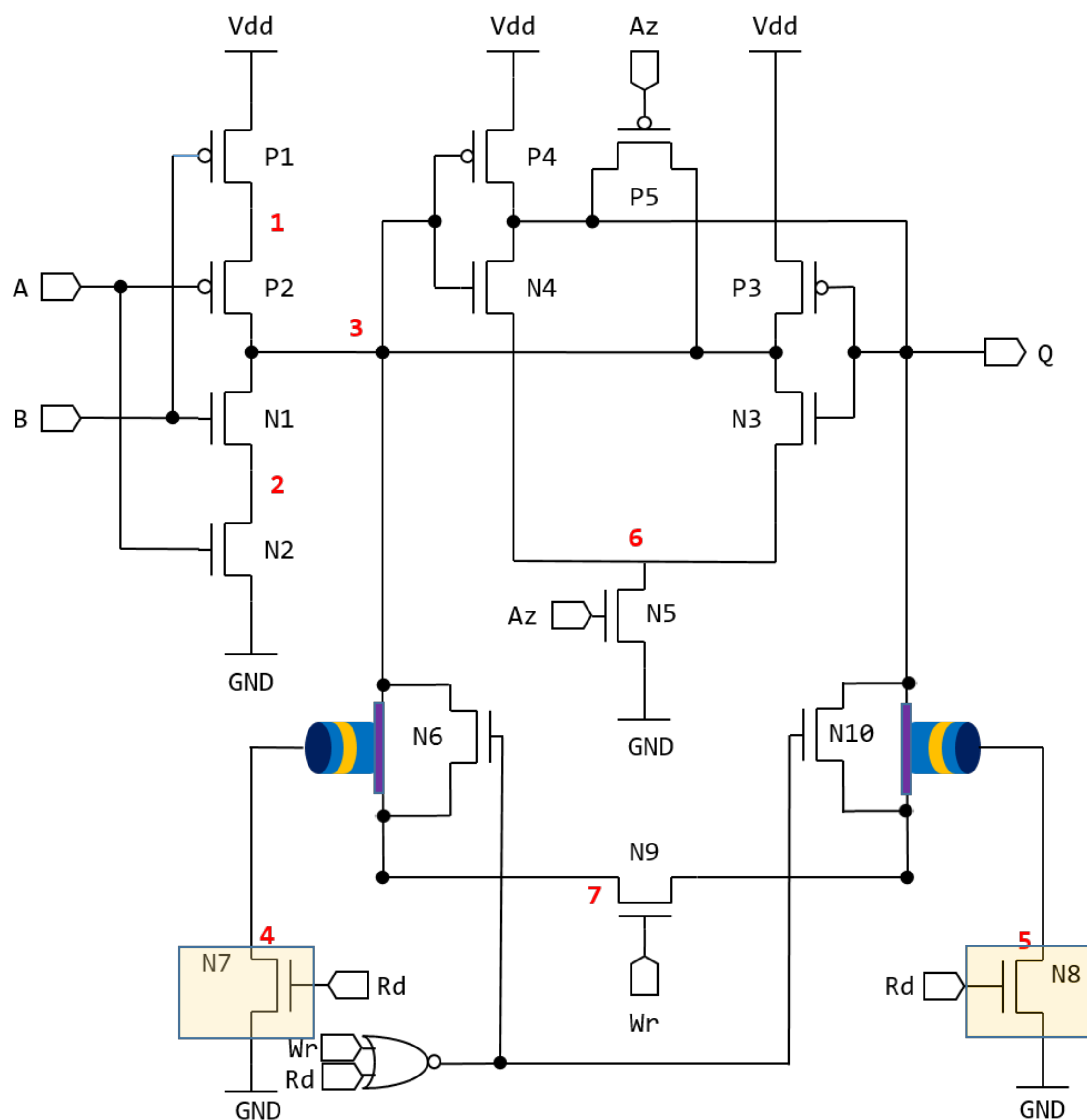

Figure 61: SOT implementation of the proposed NV C-elment.

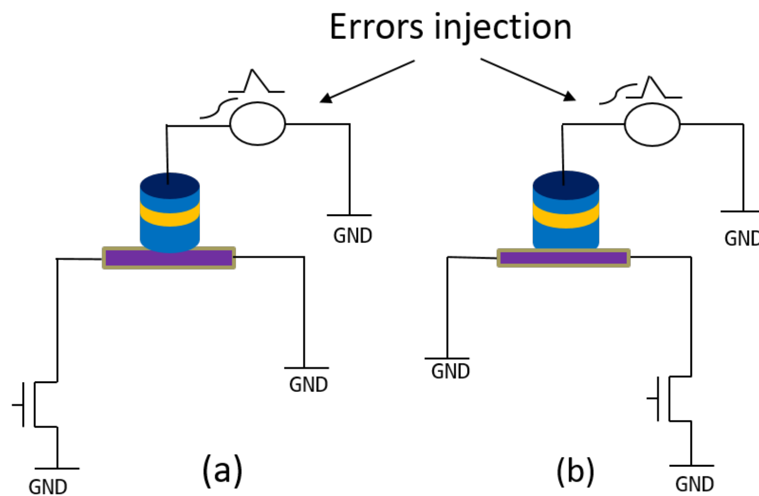

Figure 62: Error injection from the reading path in the two different writing configuration (a) and (b)

3.6.2 SOT proposed model

In this section we will build up a new SOT model which takes into account also the STT effect, in order to properly evaluate the SOT MTJ tolerance to SET. Hence, we followed the steps [53] illustrated in Fig. 63:

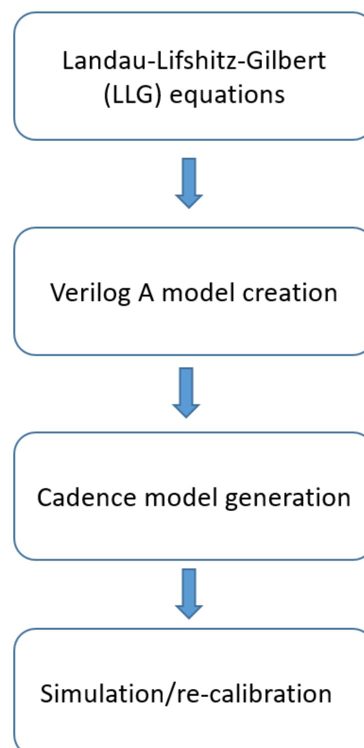

Figure 63: Flow of the proposed SOT-STT model.

As a first step we rearrange the Landau-Lifshitz-Gilbert (LLG) equations which de-

scribe the temporal evolution of the magnetization, adding both the STT (C_{STT}) and the SOT (C_{SHE},C_R) terms:

$$\frac{\partial m}{\partial t} = -\frac{\gamma}{1+\alpha^2}\vec{m}\wedge\vec{H}_{eff} - \frac{\gamma\alpha}{(1+\alpha^2)M_s}\vec{m}\wedge(\vec{m}\wedge\vec{H}_{eff}) - C_{STT}J_{MTJ}\vec{m}\wedge(\vec{m}\wedge\vec{p}) - C_{SHE}J_{Ch}\vec{m}\wedge(\vec{m}\wedge\vec{u_y}) - C_R J_{Ch}\vec{m}\wedge\vec{u_y}) \tag{3.6}$$

by solving them we find the magnetization expression on the three axes. Then, in order to obtain the model, we build the equivalent RC circuit ruled by the well-known law:

$$C\frac{\partial V}{\partial t} + GV = I \tag{3.7}$$

where C is the capacitance and G is the conductance. Then we have projected the Equation 3.7 along the 3 axes as detailed in Fig. 64 to obtain the expression of the currents. Based on that, a Verilog A code was implemented and synthesized in Cadence Virtuoso environment. According to the code, the generated model has 3 blocks as shown in Fig. 65

- In the first block by leveraging the LLG equation all the conductance are calculated as a function of the current along x, y and z.
- The second block serves as normalization of the magnetization vector components by remembering that it has to have unitary norm.
- The third block, is used to take into account the calculated variation of the TMR with the voltage across the MTJ.

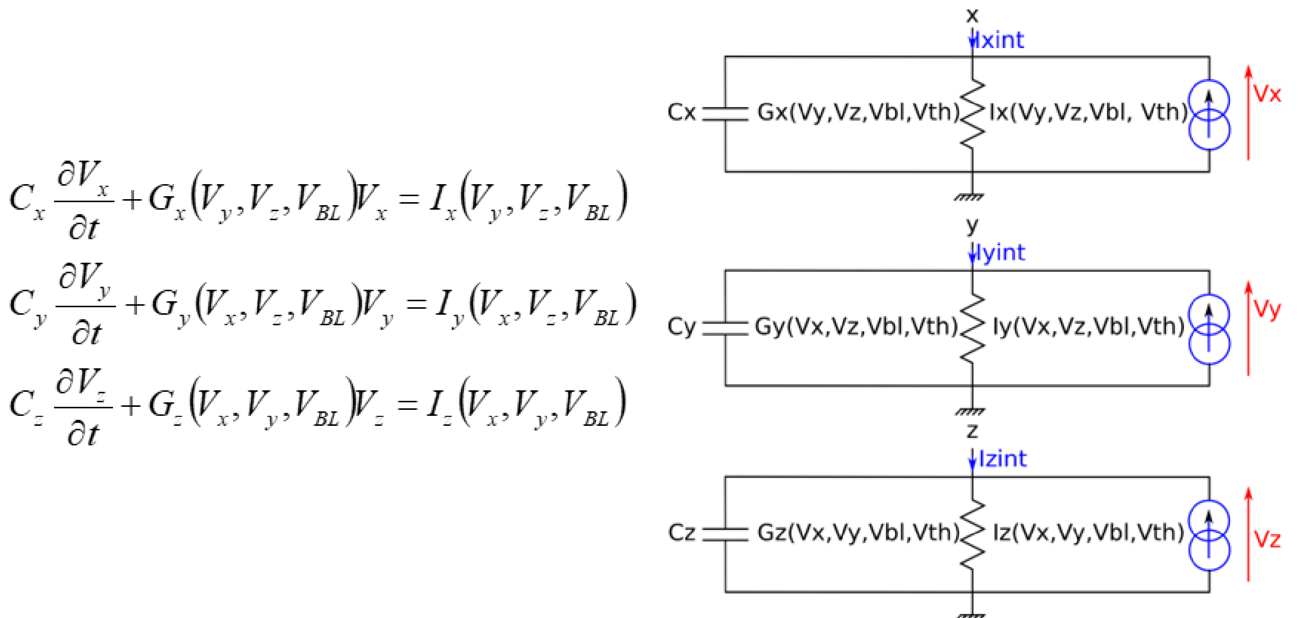

Figure 64: RC equation along the three axes and the equivalent circuit of the SOT model.

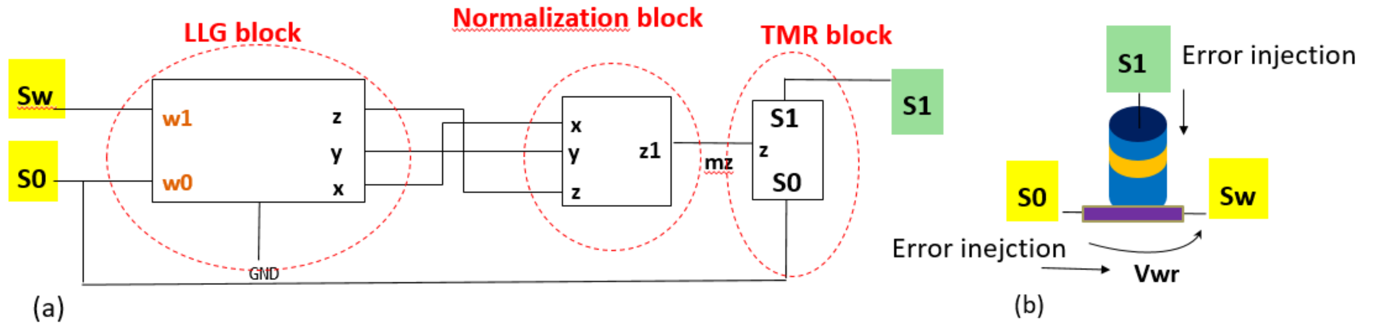

Figure 65: The three blocks that constitute the SOT model generated from the Verilog A code (a). The corresponding pins in the SOT schematic.

3.6.3 SOT robustness evaluation

3.6.3.1 Influence of the SOT channel parameters

The value of the heavy metal strip resistance depends on the chosen material as Fig. 66 shows. The Rashba and Spin hall effects coefficients in the Equation 3.6 also vary accordingly.

	Resistivity [Ω cm]	R_{SOTch} [KΩ]	C_{she}	C_r
Platinum (Pt)	20	0.180	$0.10\ 10^{-12}$	$0.05\ 10^{-12}$
Tantalium (Ta)	180	1.620	$0.05\ 10^{-12}$	$0.20\ 10^{-12}$

Figure 66: SOT channel parameters based on its material. The value are referred to a strip of 180 (length) x 50(width) x 4 (thickness), values in nm.

We have basically two way to enhance the robustness of the classical SOT writing path against current fault injections:

- Increase the width of the SOT channel so that for the same current density less current will flow through the strip. In this way the injected current will less likely reach the value needed to switch the MTJ.
- Using a material with higher resistivity so that higher current is needed to flip the MTJ.This implies the inconvenience of higher power consumption.The range for the resistance values are: 100Ω <R<3 KΩ since the resistance has to remain compatible with the MOS hybrid design.

3.6.3.2 Influence of the MTJ resistance

It is important to highlight that the MTJ resistance for SOT device is usually quite higher than for STT being the barrier thickness up to 1.8 nm. This way the barrier energy also

increase and so does the TMR (and the reading current). From the point of view of fault injection tolerance this is an advantage of SOT devices with respect to STT ones. Typical resistance values are illustrated in Fig. 67. These are limited by the MgO thickness which has to stay below 2 -2.5 nm to ensure the possibility of the electron tunneling quantum effect.

RA [$\Omega\mu m^2$]	R_p [KΩ]	R_{AP} [KΩ]
5	4	16
20	16	40

Figure 67: SOT-MTJ resistance ranges. Values are reffered to a TMR=300%

Moreover, it is important to underline that, when we try to switch the SOT from the reading path, since the current is inject from RL to FL, only the transition P to AP is possible. Thus, it is not possible to have AP to P switching induced by the electrical error injection from the reading path. The latter is another advantage with respect with the STT-MTJ in which an error could be induced in a symmetrical way. Simulation results confirm SOT to be harder to be switched, suggesting that breakdown will arrive before an accidental switching for these devices. We conclude it is not necessary to include transistor N6 and N10 to protect the SOT in the proposed circuit.

3.7 Conclusion

In this chapter, we propose a STT-MTJ based C-element with enhanced single-event tolerance. Error injections in sensitive nodes attested that only two nodes of the circuit could lead to non-volatile errors and thus, to SEU in the memory part of the circuit. A radiation-tolerant design has been proposed and tested through simulations to avoid, or at least decrease, soft errors in non-volatile magnetic elements. A specific STT-MTJ setup has been used for this purpose: STT values have been settled accordingly with the aim to decrease the MTJ's radiation-induced switching probability. An increase of write energy and delay are the drawbacks of this solution. To mitigate the first, a proper control of the write signal has been proposed. A suitable scenario for the presented VLSI cell is also mentioned: in the context of DMR micro-pipelined asynchronous circuit, the integration of the proposed circuit is convenient to block SEEs propagation, achieving SEU tolerance. As next step, a validation of the design behaviour under irradiation by means of TRADCARE® engineering tool [7] is planned. Then, heavy-ion and proton test campaigns will be performed to confirm simulation results. There are also limits inherent to the FDSOI technology robustness: on the one hand, it is shown to be more tolerant to SEU [39]; on the other, it is more sensitive to Total Ionizing Dose (TID) if compared

with bulk technology [125].

We also implemented an SOT version of the proposed C-elment. However, the number of sensitive nodes resulted increased. Besides this, in order to evaluate the SOT robustness to fault injection we developed a new compact-model which account for the possibility to write via the reading path. This gave rise to an hybrid SOT-STT compact-model, an essential mean to take into account the possibility of switching when using an electrical simulator to inject errors. Simulation results and considerations confirmed single SOT-devices more robust than STT-MTJs, while the overall circuit has an increased number the sensitive node counts.

Nevertheless experimental campaign and more advanced simulation results are needed to confirm the founding of this chapter, since electrical simulation are a very preliminary means of evaluation which do not take into account the physics and the materials.

Chapter 4

Heavy ion irradiation effects

4.1 Introduction

Comparative studies between Toggle-MRAM and STT-MRAM hybrid CMOS memory seem to suggest the latter to be more robust to heavy ion-induced hard errors [60]. This could be explained by smaller bit size and, more likely, by different nano-pillar materials. In [46] protons and gamma ray effects on in-plane STT magnetic memories are reported. Unfortunately, in-plane STT devices quickly showed their limits, so that the necessity to overcome them comes hand in hand with the need to improve reliability, power consumption and density by, respectively, improving the thermal stability, reducing the switching current, and eliminating the elliptical shape constraint.

For these motivations, Perpendicular Magnetic Anisotropy (PMA) CoFeB/MgO STT devices [48] represent today the most advanced and promising technology to achieve high density (over 1 Gb of memory capacity) application in harsh environment. To the best of our knowledge, only a few studies have explored the effects of radiations on STT-MRAM with PMA. The bit cell, typically, performs remarkably well even if the use of complementary metal oxide semiconductor (CMOS) transistors in peripheral circuitry lowers the overall robustness. In [41] it has been found that the use of PMA-MTJs can reduce the risk of bit flip by three orders of magnitude than that of conventional SRAMs during high energy neutron irradiation. In addition, few risks have been suggested for other radiation particles such as alpha particles and thermal neutrons. In [62] purely magnetic devices were found to be insensitive to Single Event Upset (SEU) up to 15 MeV Si irradiation. Hybrid PMA-STT/CMOS 55 nm memory device from Avalanche Technology was tested for Total Ionizing Dose (TID) and heavy ion radiation response in [49]. Altogether results were optimistic even in presence of some unclear failure mechanism occurring in a small percentile of 350 cumulative test runs.

Contrary to these encouraging results, serious concerns were reported in [65] where it has been shown that high-energy heavy ion tests on scaled (up to 20 nm diameter) PMA STT-MTJ under negative bias may induce clear flips between resistance states. This study intends to be a preliminary step to the integration of these spintronic devices with the most advanced CMOS node. If the robustness to high LET is confirmed, one suitable strategy for future design could be to replace as many transistors as possible with

magnetic devices, using the logic in memory concepts based on purely magnetic logic gate [101].

Additionally, the thermal effects induced by heavy ion energy deposition have been largely ignored in the field of radiation effects in electronics. Nevertheless, these effects will become more significant in electronic structures when the feature sizes will be reaching deeper into the nano-scale. Some studies tried to explain *a posteriori* the effects on MTJ irradiation sites by means of traditional LET cross-section plot or by exploiting TEM microscopy [63] [80].
In this chapter, new insights are proposed to bring clear understanding on the possible basic degradation mechanisms that can trigger SEU in STT-MTJ, regardless of the radiation source, building a bridge between radiation effects and spintronic theory. By focusing on MTJ parameters such as specific heat, density and capacitance, we propose a sensitive volume definition for the MTJ that includes not only the MgO oxide barrier and both CoFeB layers, but the entire MTJ. Concerning the SEU triggering events in the CoFeB, two switching mechanisms are considered: Spin-Transfer Torque and thermal activation. For the first time, the temperature reached during the radiation-induced thermal spike is investigated. Indeed, the thermal stability of the material's intrinsic magnetization at temperatures below its Curie temperature is a key factor to determine its resistance to radiation. Additionally, since the distance between two MTJs in the same metal layer could be as small as 500-750 *nm* in the most advanced nodes, recoil atoms from one magnetic device could upset its neighbor. This investigation on the fundamental mechanisms triggered in MTJ by irradiation are accompanied by a quantitative simulation analysis. TRADCARE® a Geant 4 based simulation tool, was employed to this aim.

4.2 Critical parameters and basic mechanisms

Radiation effects research on semiconductors has been pursued since the 1960s, becoming an extremely vivid area of research and development.
Breakthrough discoveries have occurred quite regularly, opening new perspectives for applications. Concepts like Linear Energy Transfer (LET), Critical Charge (Q_c) and Sensitive Volume (SV) were defined to assess radiation effects on memory devices that store data by injecting or removing charge. Moreover, they were introduced at a time when the channel length of a transistor was in the order of few microns. While recognizing a long history of successful engineering practice based on these concepts, they now do show their limits for devices with nanometric dimensions and when the data storage mechanism is not based on charge.

For these motivations this section investigates radiation-induced switching mechanisms, temperature effects, breakdown voltage, sensitive volume and critical charge definitions for Spin-Transfer Torque Magnetic Tunnel Junction. Thermal spike model is adopted

to estimate the temperature reached during heavy ion irradiation, and temperature effects are suggested to be responsible for the magnetic properties degradation and for upset processes.

4.2.1 Tradcare® Simulation

TRADCARE® is an engineering tool developed by TRAD and CNES. Geant4 toolkit, a multi-physics SEE prediction chain based on Monte Carlo simulation capability, was implemented in TRADCARE® software [2].

In this work, it has been used to draw the magnetic device LET profile and to extract the charge deposited into the MgO barrier and the list of secondary products under the same conditions than for the UCL heavy ion test. To this purpose, a device model was created based on the density, resistivity and thickness of all the PMA-STT MTJ atomic layers and its gds file, a binary file format including information on planar geometric shape and layout in hierarchical form (see Fig. 68). This way, the Transmission electron microscopy (TEM) image of the device (Fig. 69 a) turns out to be in complete analogy to the generated model in the simulation environment (Fig. 69 b). Fig. 70 shows the details of the implemented MTJ stack. The estimation of the deposited energy in the material for unit length was a crucial parameter in computing the temperature reached during the thermal spike as it will be detailed in the next sections.

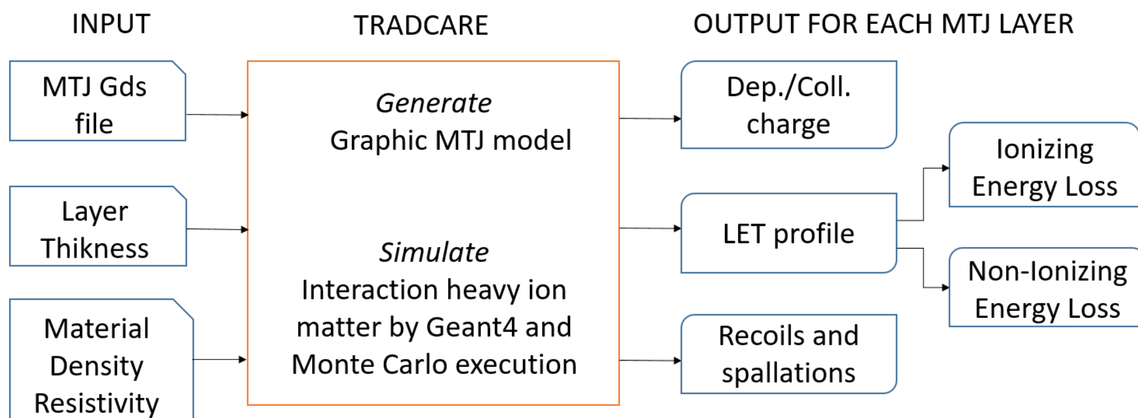

Figure 68: Schematic view of the TRADCARE® flow.

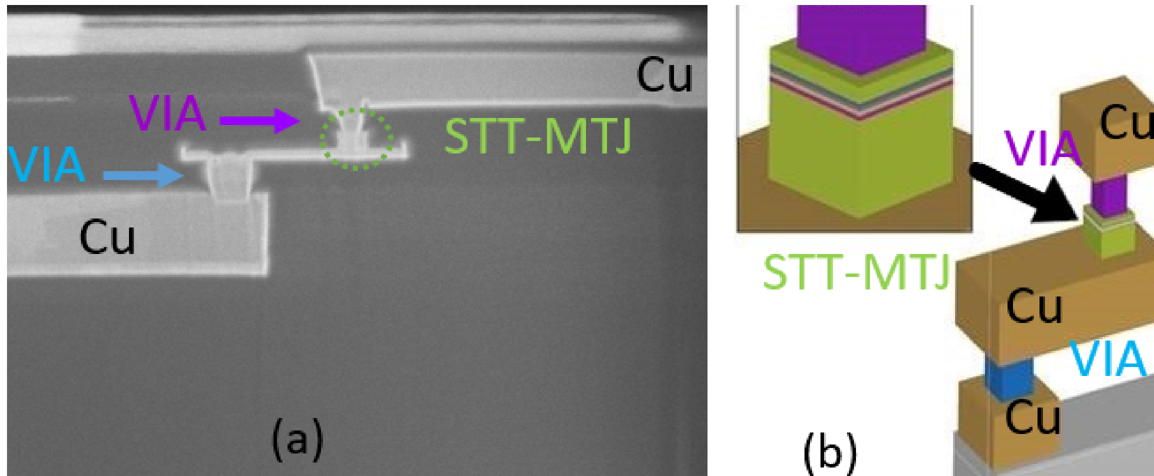

Figure 69: Scanning electron microscope (SEM) image of the considered PMA-STT MTJ (a). The corresponding device model created in the TRADCARE® simulation environment (b).

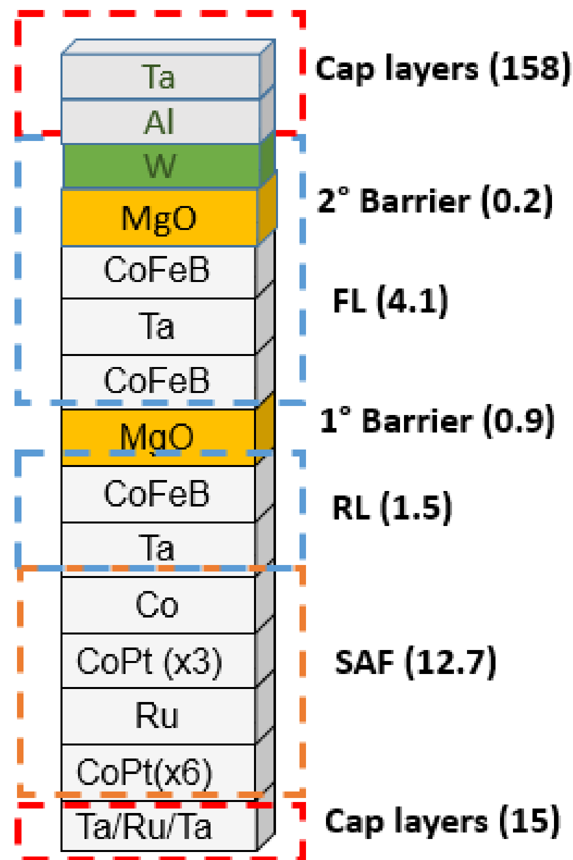

Figure 70: Details of the MTJ stack implemented in the model. Numbers in brackets represent the thickness of the corresponding layers in nm.

The LET profile and energy deposition for the main STT-MTJ layers is drawn in Fig. 71. In the plot, the LET value has been multiplied by the material density in order to highlight the differences across the MTJ materials. Thus it is expressed in keV/nm for the sake of clarity. Indeed, multiplying this value by the thickness of each layer leads to the

deposited energy. The highest energy deposition occurred in the Co layer, in particular in the Co[(0.5)Pt(0.25)]$_6$ region, due to the larger number of repetitions. A considerable LET (60.3 keV/nm) is also deposited in the CoFeB alloy but, due to the limited thickness and the slight mitigation of the Ta spacer (52.3 keV/nm), it does not result in a remarkable amount of deposited energy; as expected, the less affected layer is the oxide, with a very low LET and thickness.

One could question the validity of applying classical concept as LET approach to such multi-materials nano-structures. This is clear by comparing Fig. 71 with Fig. 72 where LET and range for the different MTJ materials are plotted.

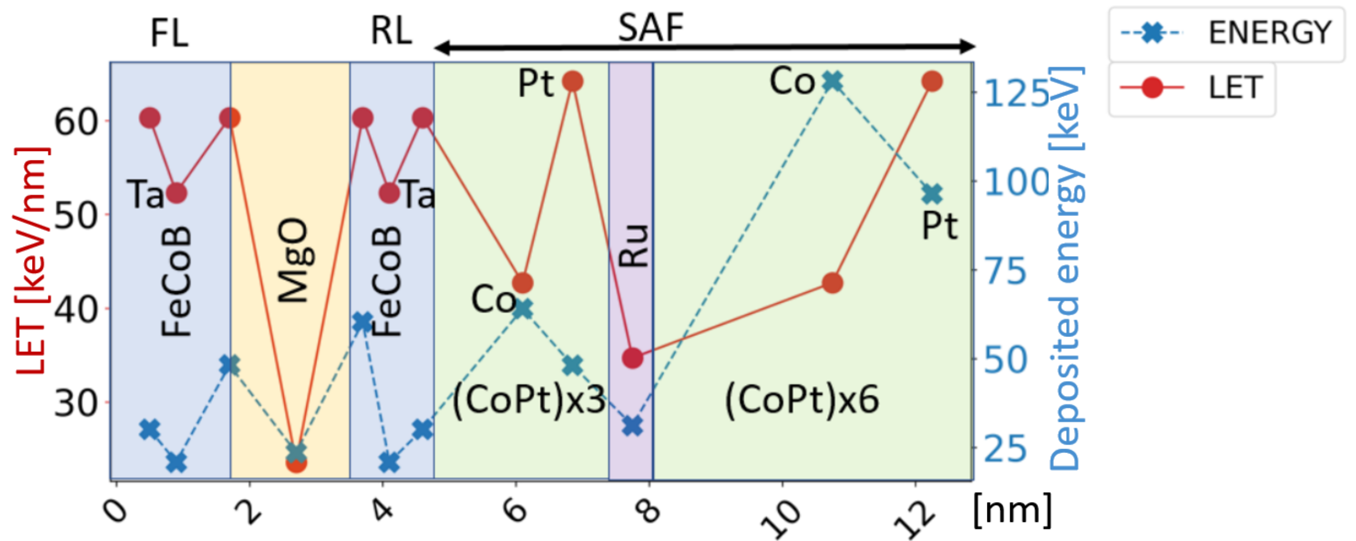

Figure 71: LET and deposited energy across the different materials in the main MTJ stack.

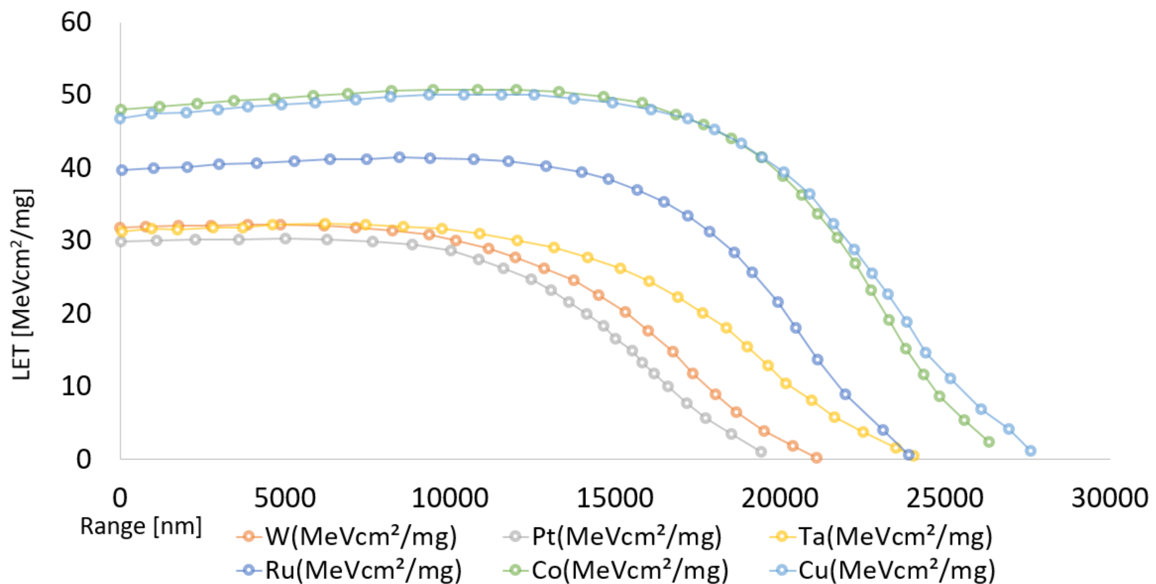

Figure 72: LET of ^{124} Xe^{35+} in the MTJ's material if they were standing-alone.

The physics selected for the secondary production during Xenon irradiation simulation is the hadronic Bertini cascade model [122] exported from Monte Carlo Geant4 tool. Even if in the PMA STT-MTJ two MgO barriers are present, only the one associated with the Tunnel Magnetoresistance (Fig. 70) has to be taken into account for the breakdown process. Thence, among all the secondary products, we listed the ones that crossed the insulating barrier as depicted in Fig. 73. Encouragingly enough, most of these particles (76%) deposited a charge equal or lower than 1 fC. Only 0.0096% of the secondaries deposited a charge of 20 fC, a value one order of magnitude smaller than the one able to induce a breakdown.

Thanks to TRADCARE® simulations, we also excluded another potential problem: the possibility that the pads could lead to the MTJ breakdown due to an excess of charge at their surface. Indeed, the pad's surface is 200 μm x 200 μm, a huge size in comparison to the MTJ. To check the validity of this hypothesis, under our experiment condition, we simulated the irradiation of the bilayer (300 nm Al+ 10 nm Cr) pads and we found a deposited charge of $9{\cdot}10^{-10}$ C for a 10^{5} ions/cm^2. Since the upper and lower pad areas are the same, in the limit of the fabrication process, a very weak charge flux will be established through the MTJ and thus the eventuality of a breakdown seems to be not possible.

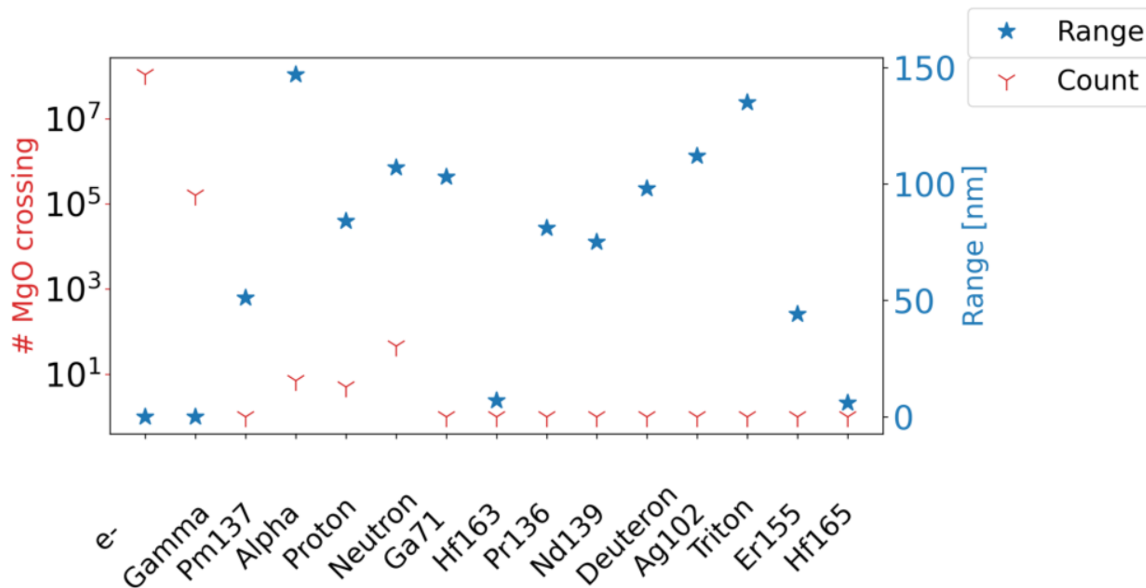

Figure 73: List of the secondary products that crossed the MgO barrier. The crossing count is in logarithmic scale

4.2.2 Single Event Effects originates in CoFeB

4.2.2.1 Spin-Transfer Torque Switching

As demonstrated in [48] the minimum charge needed to switch the free ferromagnetic layer through an ordinary spin-torque mechanism is given by:

$$Q_{switch} > 2qN_s \tag{4.1}$$

where q is the elementary electron charge and N_s, representing the total number of spin, can be calculated as:

$$N_s = \frac{M_s V}{\mu_B} \tag{4.2}$$

where M_s is the saturated Magnetization, V corresponds to the Free Layer Volume and $_B$ is the Bohr magneton. The quantity of charge obtained from Eq. 1 should be multiplied by 1.25 to take into account the fact that the polarization of the electrons tunneling through the MgO barrier is about 80% [86]. We identified with this value the critical charge of the FL, as defined traditionally, the minimum amount of charge needed for an SEU occurrence triggered by STT mechanism.
For example, for an MTJ with a radius of 10 nm, we obtain $N_s = 4062 \cdot 10^3$ and thus a value of $Q_{criticFL}= 1,627\ pC$. According to Eq. 2, MTJ's diameter scaling and FL thickness decrease will both have a detrimental effect on the critical charge as shown in Fig. 74. Hence, we can compare Q_{switch} (needed to trigger an upset by STT mechanisms) with the charge deposited in the FL by different ions at various energies to see if it can be exceeded. Simulation is used to evaluate the number of hits induced by 1 GeV Ba ions needed to deposit an amount of charge equal to $Q_{criticFL}$ as highlighted in Fig. 74. It is important to underline that, to trigger the requested current injection, these hits should occur quasi-simultaneously since the relaxation time of the excited carriers is in the order of ps [33]. Therefore, it appears very unlikely that direct hits induced by heavy ion could trigger an SEU. This is also confirmed by the STT-MTJ switching probability distribution obtained by electrical simulation. Indeed, the duration of the switching pulse is around 2 *ns* when the applied voltage across the junction is 1 V. It follows that, even if a shorter pulse could carry the same amount of charge, this would result in a voltage drop higher than 1 V across the MTJ; the breakdown electric field of these devices is around 1V/nm. In other words, a smaller number of more energetic strikes will cause directly the breakdown of the device instead of triggering a spin-transfer torque effect.
In conclusion, it seems almost impossible to explain the post-irradiation STT-MTJ switching, observed in previous studies [64] [61], from the viewpoint of STT dynamics induced by particle hits whatever the ion species chosen for the irradiation. As a consequence, the critical charge is not a suitable definition neither for switching nor for breakdown since the pulse duration and voltage drop across the MTJ are decisive parameters to be taken into account.

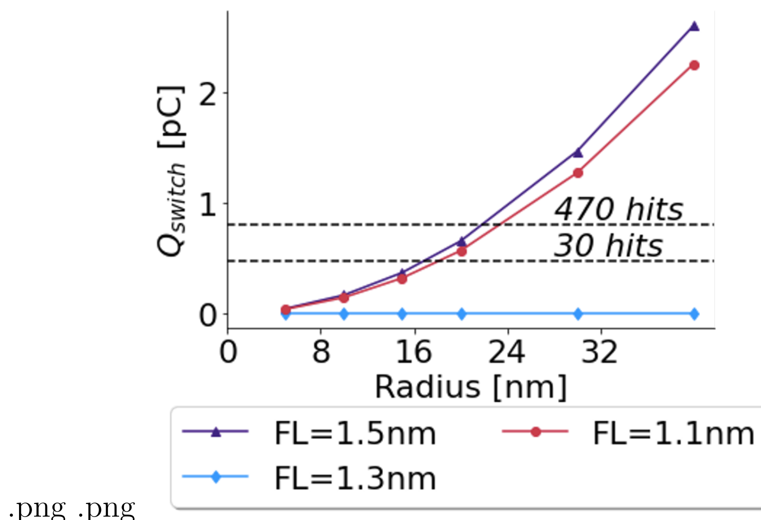

.png .png

Figure 74: Free layer Critical charge by varying MTJ radius and FL thickness. Dotted lines represent the number of Ba hits needed to deposit the equivalent amount of charge.

4.2.2.2 Thermal Switching

The energy released within the MTJ by a particle strike could potentially thermally activate the switching of the magnetization. In order to estimate the heating process due to heavy ion irradiation, different models were proposed in the last decades [119]. Among them, the thermal spike model [115] is the only one that works for all kinds of materials including semiconductors and insulators [24]. According to this model, heat waves propagate from the heavy ion hit point around the ion track in a radial way. The main idea is to suppose that the energy deposited in the lattice can be described by a transient thermal process acting in the electronic and atomic subsystems. The temperature evolution in the spike can be calculated by assuming that the initial temperature distribution has the form of a δ function along a linear ion track [15]. Thence, the temperature at a radial distance r from the impact and at time t can be written in cylindrical coordinates as:

$$T(\mathrm{r},\mathrm{t}) = \frac{F_\mathrm{d}}{4\pi k t} exp(-\frac{C r^2}{4 k t}) + T_{(\mathrm{t=0})} \tag{4.3}$$

where F_d is the fraction of deposited energy in the material per unit length (electronic excitation and nuclear collisions), K is the thermal conductivity, C is the heat capacity and $T_{(t=0)}$ is the material's temperature before the strike. Density (ρ) and heat capacity (c) values for all the MTJ layers are listed in Table 4.1. For metals as well as for alloys specific heat capacities were estimated based on the Dulong-Petit law. $\mathrm{F_d}$ [keV/nm] was computed from the LET profile obtained from TRADCARE® simulations. Fig. 75 depicts the LET at 1 GeV for Xe and Ba ions across the three MTJ's layers: FL, insulator, RL.

Table 4.1: Values of density , heat capacity *c*, and total thickness *t*, of the MTJ layers materials

Material	$\rho [Kgm^{-3}]$	$c\ [J/(k\ Kg]$	$t\ [nm]$
Ta (β)	16327	144	178.3
Pt	21450	180	4.25
Co	8900	639	5
Ru	12370	239	1.6
CoFe	8658	446	2.7
MgO	3560	648	1.2

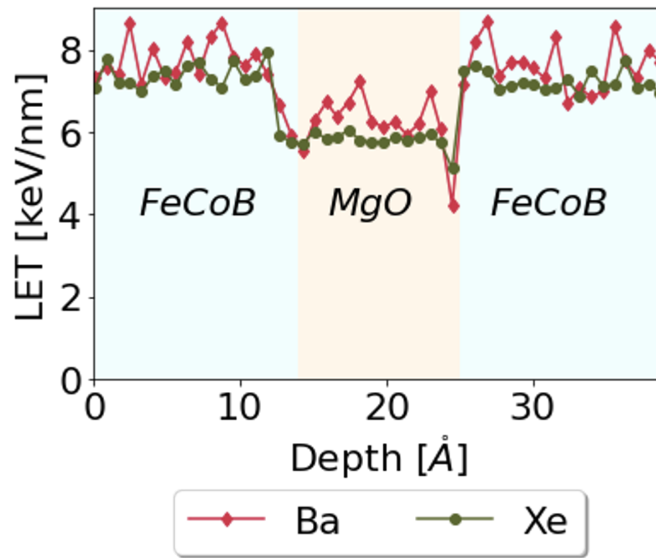

Figure 75: Electronic LET profile for Ba and Xe ions across the three MTJ's layers FL (CoFeB)-MgO-RL (CoFeB).

It is obvious that the electronic stopping power affects the location of the range distribution. Therefore, the thermal spike's strength depends on the ion type and on the material where it originates. Fig. 76 shows the temperature distribution reached during the thermal spike for Xenon ion on CoFeB. Extremely high temperature (thousands of K) are reached during some fs to few ps at the strike point. Then, the heat waves continue to propagate and the temperature relaxed to 370 K after 2 ns.

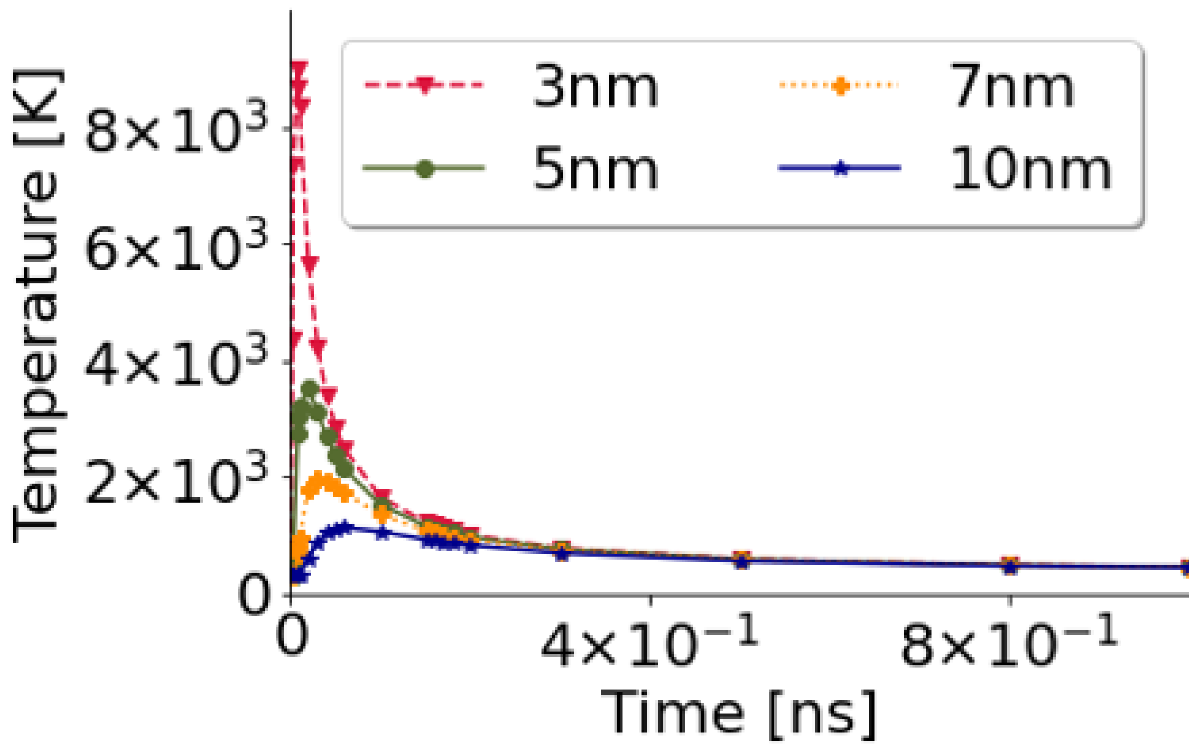

Figure 76: Thermal spikes in CoFeB FL induced by a Xe strike.

Simulations demonstrate that particle strikes on Si substrate can thermally affect the MTJ. In addition, the thermal spike propagates, thus the MTJ does not even need to be directly hit to be reached by an undesired thermal spike. A strike originating in Platinum reaches a temperature equal to 600 K after 1 ns while a value just under 400 K is attained in the case of a particle strike on a Platinum layer as depicted in Fig. 77. Consequently the maximum propagation range, namely the radial distance at which the temperature returns to around 300 K, is larger for Platinum than for Silicon.

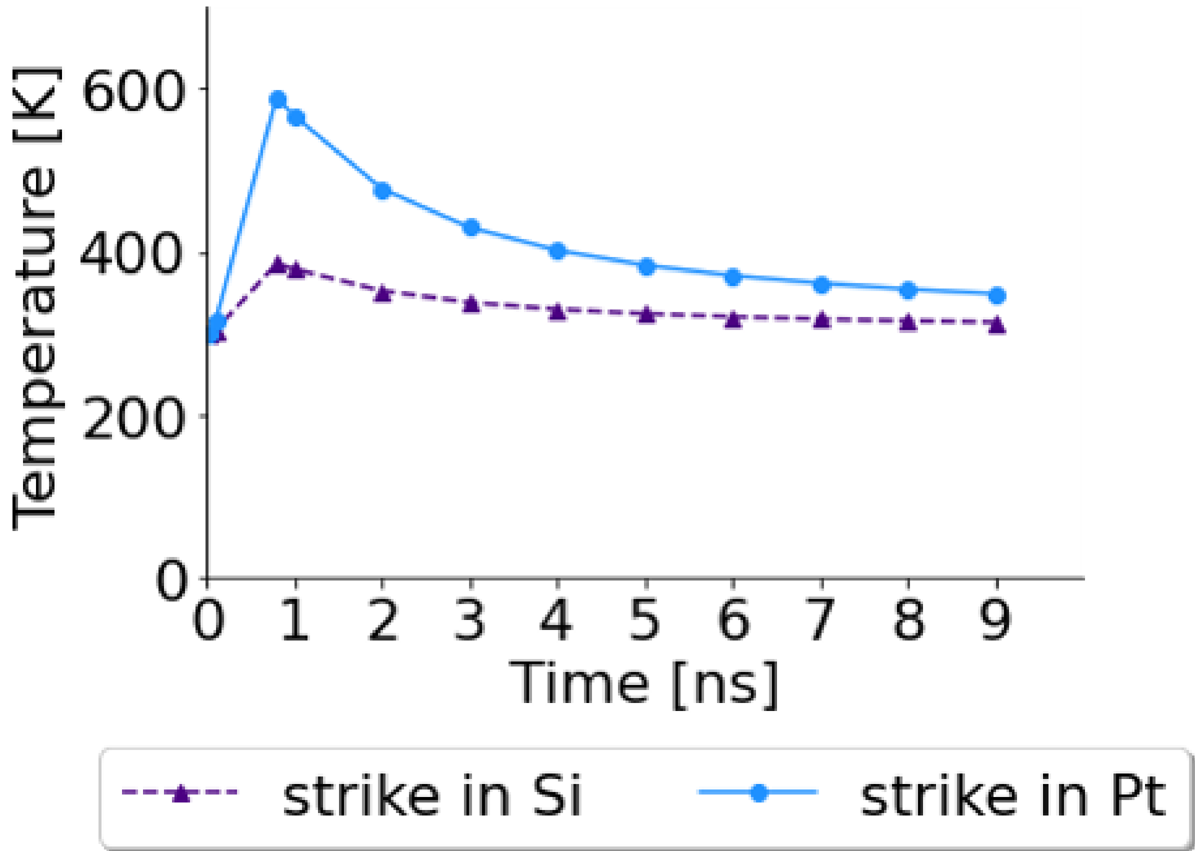

Figure 77: Thermal spikes induced by Xe on Si and Pt at 30 nm from the hit point.

However, at a temperature T, the thermal switching probability of the magnetization, after a time t, is fitted exactly by the Néel Brown relaxation formula:

$$P(t) = 1 - exp(-\frac{t}{\tau_0 exp(-\frac{\Delta E}{K_B T})}) \tag{4.4}$$

where the exponential at the denominator is the mean time needed to switch the MTJ's FL orientation, according to Arrhenius law: τ_0 is the attempt period (1 ns), and T is the temperature reached during the strike. As plotted in Fig. 78 for one bit, in a range of temperature between 400 K and 550 K, the switching probabilities are less than 10^{-2}. At higher temperatures they exponentially rise from T = 619 K with a corresponding P_{switch} = 8% to T = 750 K with P_{switch} = 50%.

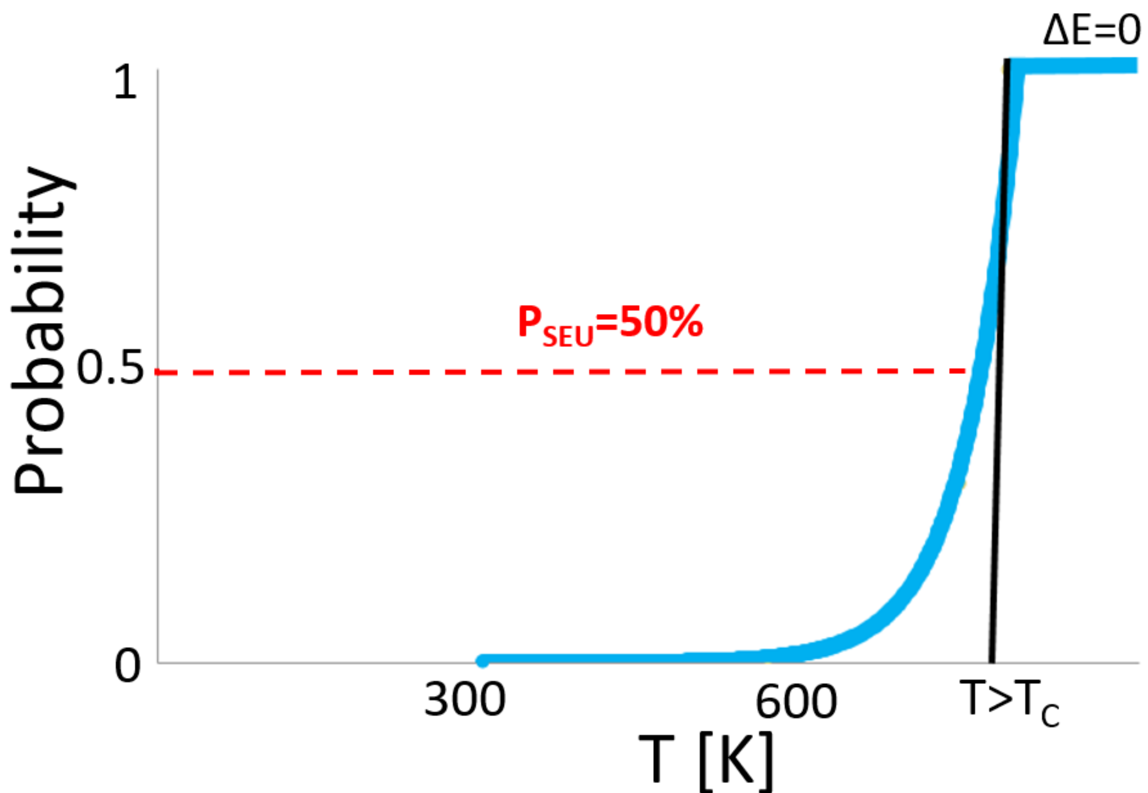

Figure 78: Free layer thermal switching probability distribution after a time equal to 5 ns from the strike moment.

4.2.3 Transient thermal Events

4.2.3.1 Magnetic properties degradation

Regardless of how the MTJs experience the temperature rise (direct hit or hit proximity), the magnetic properties of the spintronic devices are dramatically affected by these temperature spikes. These degradation effects are transient but their ability to threaten the memory should not be underestimated since they start to be triggered at temperature spikes not very high above room temperature. For this reason, it can be expected that thermal induced stress, due to several heating/cooling cycles, could have an important impact on the functional STT-MTJ lifetime.

Indeed, according to Bloch's low [9], the temperature dependency of the saturation magnetization M_s and the anisotropy K_u can be fitted as:

$$M_{\mathrm{s}}(t) = M_{\mathrm{s}}(0)[1 - (\frac{T}{T_{\mathrm{C}}})^{3/2}] \tag{4.5}$$

$$K_{\mathrm{u}}(t) = K_{\mathrm{u}}(0)[(\frac{M_{\mathrm{s}}(t)}{M_{\mathrm{s}}(0)})^{2.2}] \tag{4.6}$$

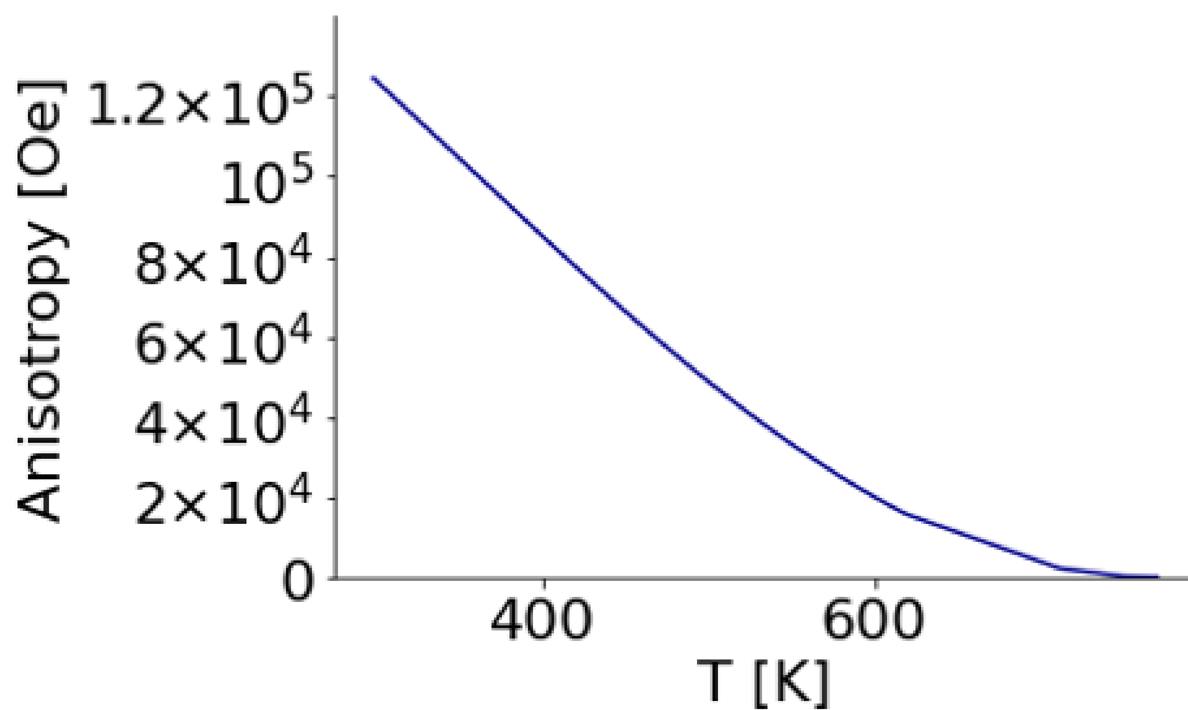

Figure 79: Temperature variation of Anisotropy.

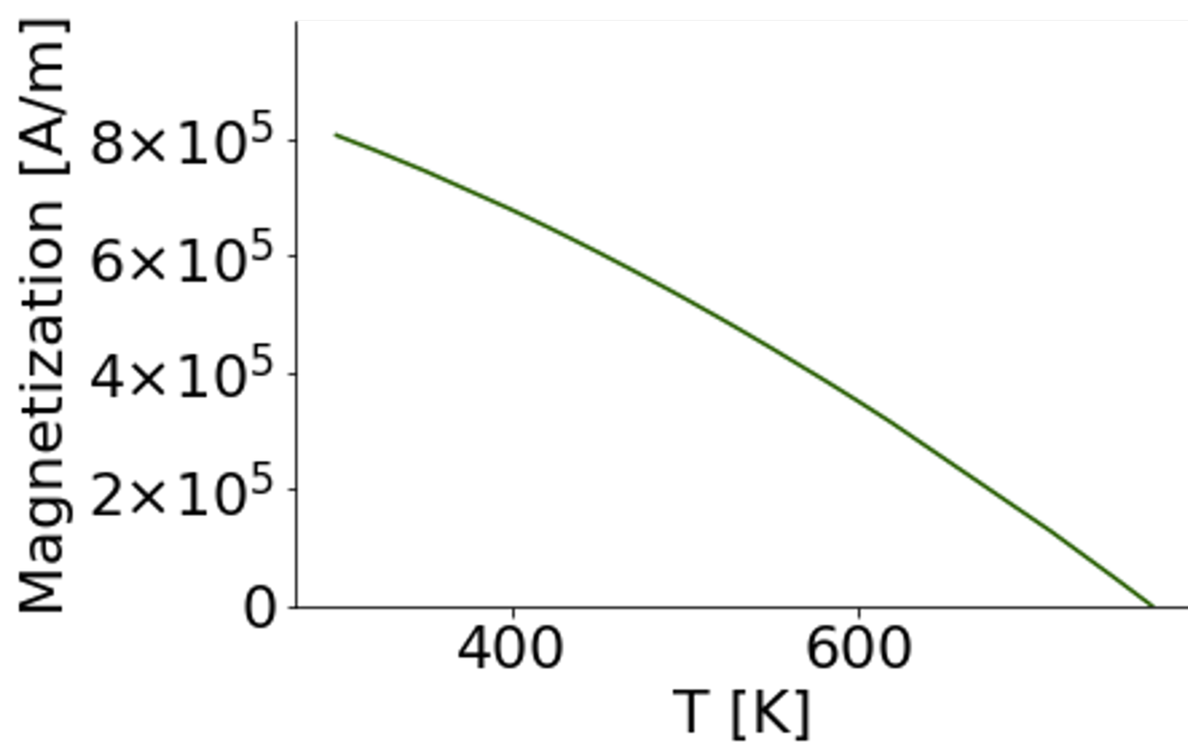

Figure 80: Temperature variation of Magnetization.

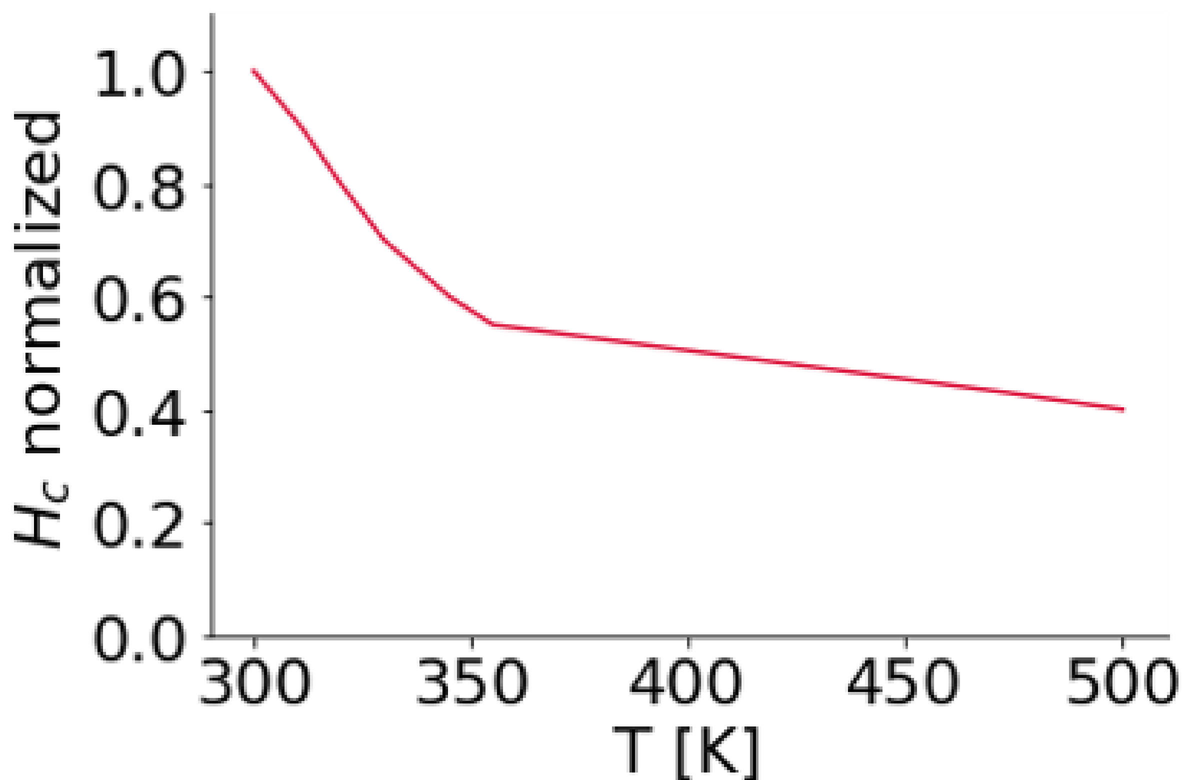

Figure 81: Temperature variation of Coercive field.

As noticeable in Fig. 79, perpendicular anisotropy is more sensitive to temperature rise with respect to magnetization (Fig. 80). However, among the STT-MTJ analysed parameters, the coercive field is the most affected by temperature increase, as our experimental data in Fig. 81 demonstrate, in agreement with the state of the art [51]. For example, a temperature of 340 K is already high enough to decrease the anisotropy by 17% whereas at the same temperature the coercive field is reduced by 38% from its initial value. Around 510 K the transient loss of M_s and K_v is attested to be 50% of their initial value.

4.2.3.2 Thermal stability and Retention time of the stored information

The energy barrier, ΔE, which divides the two stable opposite states (AP, P), depends in a complex way on both M_s and K_u (and on the free layer volume) [74]. Nonetheless, in macrospin regime (r<30 nm) the barrier height could be approximated in a simplified way, as:

$$\Delta E = K_u V \tag{4.7}$$

where K_v is the anisotropy and V is the FL volume. Then, recalling that K_B is the Boltzman constant, we can define an important parameter which represents the MTJ's

thermal stability factor, as follows:

$$\Delta = \frac{\Delta E}{K_B T} \tag{4.8}$$

It follows immediately that a temperature rise, combined with the radius scaling, will drastically reduce the thermal stability of the memory device, as the plots in Fig. 82 illustrate.

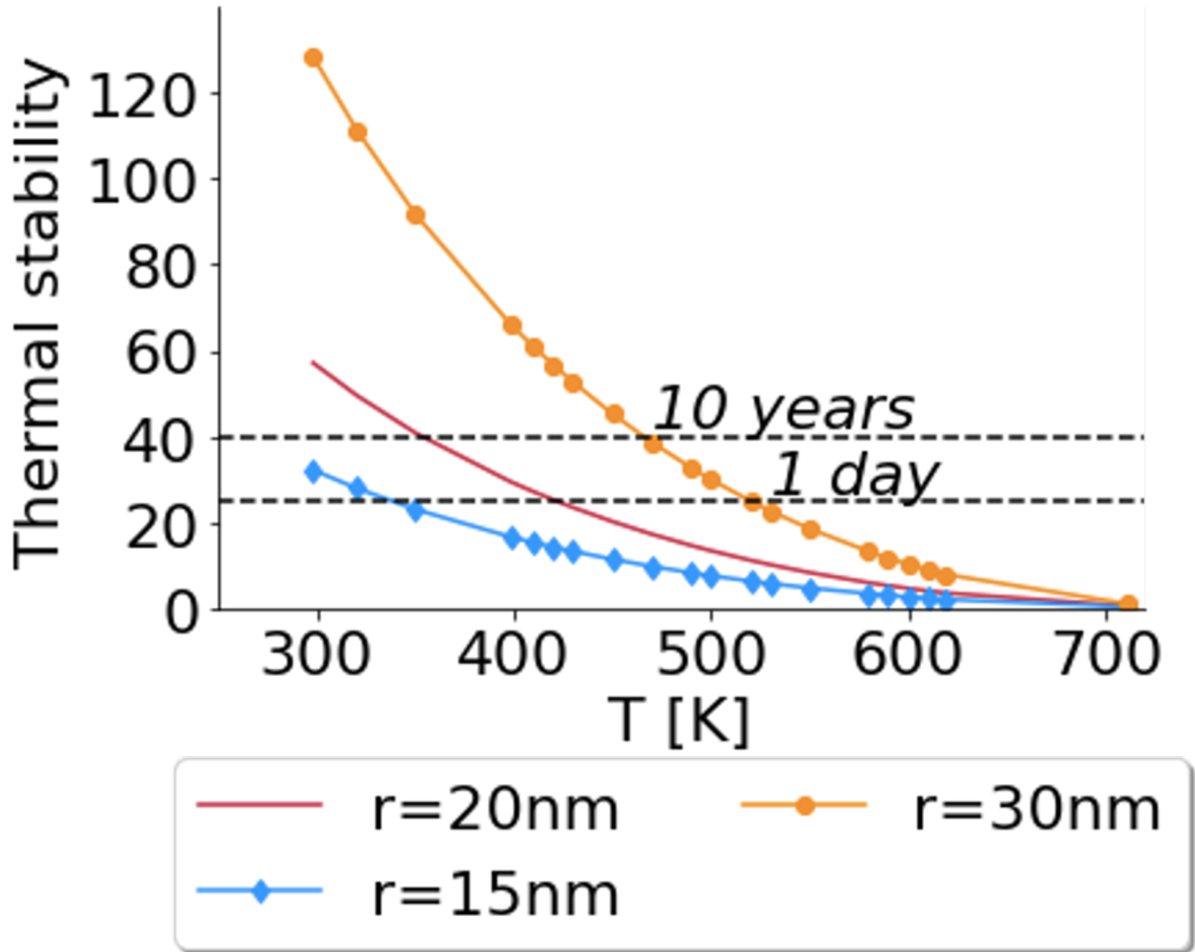

Figure 82: Thermal stability factor and retention time impacted from scaling and temperature rise.

The stability of the stored information (i.e. the retention time) for a duration T_r can be written as [26]:

$$\frac{\Delta E}{K_{\mathrm{B}} T} > \ln(\frac{T_{\mathrm{r}}}{\tau_0}) \tag{4.9}$$

This inequality sets the condition upon the minimum barrier height needed for the stability of the storage layer against thermal fluctuations at a given T. For example, for a 3 years space mission, we obtain from Eq. 9: E>39 $K_B T$ that is not met for any temperature above 353 K. Luckily enough, the temperature of the MTJ will not be constantly equal to the one reached during the strike, but a criticality still remains since MTJ scaling

also has a deleterious impact on the thermal stability factor as highlighted in Fig. 82. This could represent an important limitation for missions where the average temperature at device level is expected to be constantly higher than 350 K. Indeed, this failure mechanism is related to temperature, hence could be triggered even without any particle strikes. Additionally, these considerations suggest that the most scaled devices are not the most suitable for harsh environment application since thermal stability and retention time depend on the MTJ size. For example, as can be seen from the dotted line in Fig. 82 a thermal stability value of 40, equivalent to a retention time of 10 years, is ensured at a temperature of 473 K for a 30 nm radius, whereas for a 20 nm radius this stability is matched at a lower temperature (358 K). An interesting idea to overcome this problem could be the recently presented Perpendicular Shape Anisotropy (PSA) MRAM in which the dimension (volume) of the free layer is drastically increased along the vertical axis while keeping a scaled radius [98]. Another promising option to enlarge E is to increase the number of MgO-ferromagnetic interfaces [93].

4.2.4 Permanent thermal effects

4.2.4.1 H_C degradation and the role of Synthetic Antiferromagnetic layer

The narrowing of the hysteresis loop in perpendicular anisotropy STT-MTJ as temperature rises was already experimentally proven in [95]. In this work, a mismatch was found among the theoretical prediction of the H_C temperature degradation rate in [113] and the obtained experimental data. For this reason, it was concluded that the temperature sensitivity of H_C was in reality higher than the one predicted in [113] due to stress or strain on the devices, caused by the patterning and encapsulation. Here we want to take one step beyond, and argue that, even after the cool down, some degradation in the coercive field remain.

This was observed by measuring the hysteresis loop of some STT-MTJ SPINTEC samples before and after a bake at 475 K: the coercive field is reduced. Since the absolute value of the coercive field appears to be reduced mainly from AP to P state transition, the thermal rise seemed to induce an asymmetry of thermal stability between parallel and antiparallel states, the first one being favored. Interestingly, the simultaneous variation observed in offset field, H_{off} allows us to argue that the first is a consequence of the second: defects creation in the SAF results in an uncompensated stray magnetic field from RL to FL that ends up favoring the transition towards parallel state, i.e. a smaller absolute value of the coercive field from AP to P reversal. These findings are in agreement with [55] where it was proven, experimentally and for the first time, not only that H_{off} and H_c changes are related, but also that a significant increase of the first induced a reduction of the second and this correlation worsen with scaling.

In conclusion, even if the temperature rise associated with a single event lasts for a short time, the effects on the MTJ stability could be permanent, most likely cumulative, due to a complicated synergy of recoils and electronic excitation such as cascade collisions, thermal spikes, latent track formation and displacement damage. As a result, an important role is covered by the different coefficient of thermal expansion inside the MTJ (magnetovolume) and by the materials that surround the MTJ and could exert a strain on it (magnetostriction). The relation between thermal film stress/strain and magnetic properties in CoFeB is particularly strong since these alloys have a high positive magnetostriction [88]. Additionally, experiments found out that magnetovolume and magnetostriction result also in a modification of Curie Temperature for the ferromagnetic materials: an increase in case of lattice expansion and a decrease in case of constriction. In the case of swift heavy ions irradiation, the thermal MTJ's bottleneck could be most likely represented by the SAF, the two Co/Pt multi-layers blocks separated by the Ru spacer. There are at least two motivations to this statement. The first one is related to its thickness and density: according to our simulation, most of the energy will be dissipated in this part of the MTJ. Our findings are in accordance with [121] where after swift heavy ion irradiation, the STT-MTJ most affected layer was the Co/Pt. Noticeably, as shown previously (see Fig. 77), the radial distribution of the heat propagation for the Pt is very wide. The second is related to the key role of the Rutenium spacer that has to ensure the antiferromagnetic coupling between the two CoPt multilayers: a reduction in the effective thickness of the Ru (0.9 nm) (due for example to thermal intermixing or diffusion of Ta [118], or Fe in the SAF [44]) will result in a loss of the SAF magnetic moment and thus a destabilization of the AP state. This possibility is corroborated by [118] where it is demonstrated that over a fluence of 10^{14} ions/cm^2 the 2 blocks become ferromagnetically coupled and behave as a single thicker ferromagnetic layer. Accordingly, the loss of perpendicular Magnetic Anisotropy was documented in CoPt multilayers over 10^{15} Ga^+ ions/cm^2 irradiation in [114] and in [32]. In particular, the substitution of Ta, as the cap layer, with W seems to be beneficial to avoid deleterious material inter diffusion [117].

4.2.4.2 Curie Temperature overtaking: Thermal Event Upset

Thermal switching and temperature effects appearing to be a serious concern, one more important temperature-dependent process should be analysed, since it could lead to the loss of the stored information.

Indeed, ferromagnetic materials preserve their magnetic property only below the so-called Curie temperature, above which they fall in a disordered magnetization state, becoming paramagnetic. If this threshold is exceeded even for a very short duration, the magnetization is completely destroyed and then rebuilt during cooling time, in principle, in up or down state with equal probability. In reality, since the parallel state is favored from an energetic point of view, the final mutual configuration of the FL and RL will always

be parallel, regardless of which ferromagnetic layer's magnetization will be rebuilt first. In other words, this is an asymmetrical upset as the final state will always be logic value "0". Thence, if the initial stored bit was "1" the probability of upset is 100%; on the contrary, if the initial stored bit was "0" the bit will be restored after a transient loss due to the paramagnetic transition and no upset will occur. However, the MTJ will be still operational after cooling, but the information in the bit cell could be corrupted.

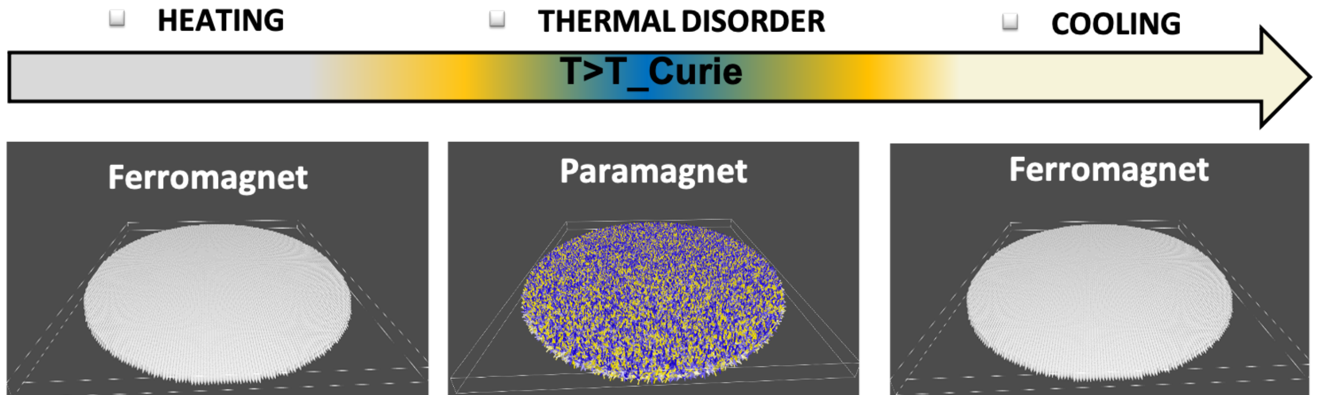

Figure 83: Thermal evolution and TEU occurance: FL and RL will always align in the favored energetic configuration, i.e. the parallel state.

The Curie temperature, specific for each material, strongly depends on the thickness of the considered layer: for a 1.5 nm thick CoFeB layer it is 770 K [70]. This could explain the sudden SEU occurrence always toward parallel state.
This upset is not directly related to the strike of the MTJ but rather to the temperature reached even in the proximity of the device, exceeding the material's Curie's temperature. We propose to call this specific mechanism Thermal Event Upset (TEU). The notion of proximity becomes particularly delicate since the distance between devices scale down as depicted in Fig. 85. This latter is attested to be as small as 500 nm in the most advanced technology node. Fig. 84 shows the secondary energetic recoil products range and energies. Even in the presence of the typical SiO_2 spacers that surround each MTJ, simulation results seem to suggest that the most energetic recoils could threaten the neighbour MTJ on the same metal layer.

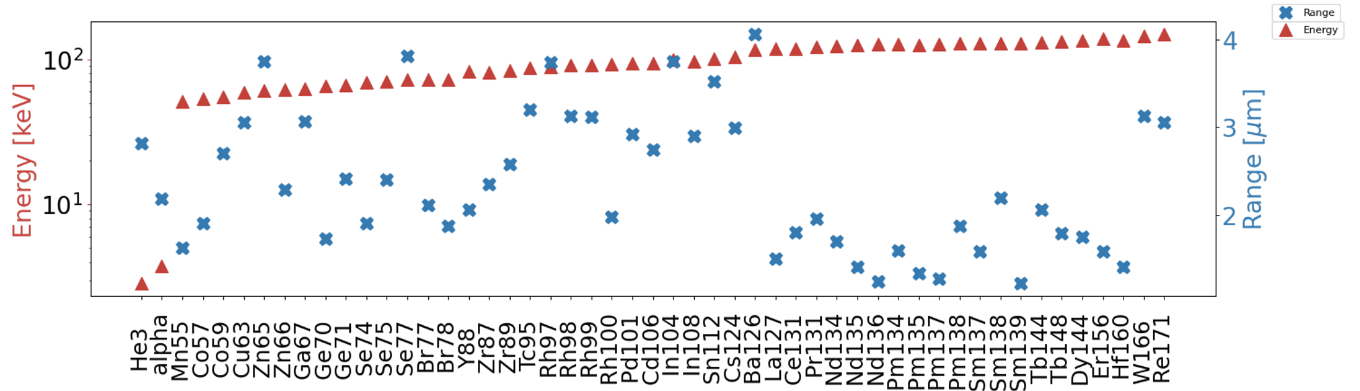

Figure 84: Energies and ranges (along the longitudinal axis) of secondary products expected during the irradiation experiment.

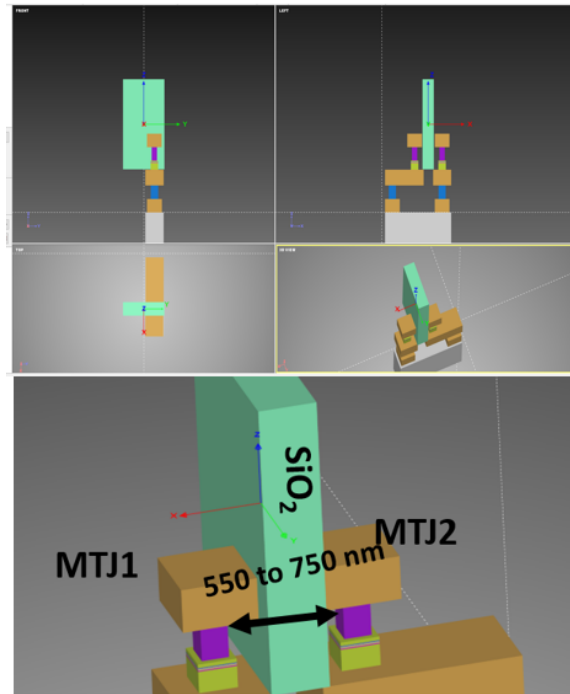

Figure 85: As process get denser secondaries product have a range comparable with the space in between one MTJ and the other. View in TRADCARE® environment.

4.2.4.3 MgO Tunnel Barrier

If the thermally driven processes triggered under irradiation have a predominant role during ion strikes (in the limit of a certain fluence), it seems reasonable to argue that degradation of magnetic properties appear before degradation of electrical properties. Reference [96] presents irradiation results obtained in recent perpendicular STT-MTJ which corroborate our thesis. The observation has been first attributed to the modest penetration of the low energy ions in the device stack but, it has also been observed after high energy ($\geq$ 2 GeV) ion irradiation [121]. For this last ion energy, the nuclear energy loss ($\leq$ 1 keV/nm) is negligible compared to the electronic energy loss. Thence the inelastic

Table 4.2: NIEL, displacement per atom and number of atoms displaced in the MgO tunnel barrier during 1 GeV irradiation, 10^{12}ions/cm^2

	NIEL [keV/nm]	*DPA [10^{-4}]*	*Displaced Atoms*
Xe	3.58	3	56
Ba	4.29	3.6	68
Bi	12.8	11.7	221

collision dominates the energy loss process. Along the incident ion path, there is a state of intense electric excitation that, in principle, can lead to the formation of a damaged region and the electron-phonon coupling constant dominate how the thermal energy diffuse over time according to the thermal spike model (as detailed in the subsection 4.2.2.2). However, highly ionizing particle irradiation in insulator can, via a thermal spike phenomenon, promote self-healing rather than defect production [25]. This could explain the observed robustness of the electric properties with respect to the magnetic ones, even when ion irradiation can induce the presence of few tracks observable in cross-sectional TEM image in the insulating MgO layer [121]. If the thermal spike is the dominant damaging process the same hypothesis formulated for the degradation of the magnetic properties explain the maintain of the electric ones. This should be valid at low and moderate fluences when the possibility to precisely hit the MTJ is intrinsically very low. This will also explain why with increasing the fluence the TMR is finally corrupted: typically, numerous tracks creation occur in the MgO creating defect-rich regions. At high fluence, this degradation process dominates over self-healing. The ion type chosen for the irradiation still plays a key role since the difference in mass, and thus nuclear and electric stopping power in the material, lead to important fluctuations, as confirmed by simulation results summarized in Table 4.2.

4.3 Dynamic Irradiation Experiment

The last generation of PMA STT-MTJ, i.e. Double Barrier Magnetic Tunnel Junction memory devices were used to this purpose. Indeed, as the MTJ dimensions scaled down over 40 nm, the PMA (and thence the thermal stability factor) can be threatened since the interfacial surface, where the anisotropy generates, is reduced. Thence, to further take advantage of the CoFeB/MgO interface, i.e. the main source of PMA, the number of oxide layers has been doubled, this way benefiting of two metal/oxide interfaces.

Since the interactions of heavy ions with matter can create a plethora of unwanted consequences such as target fragmentation, projectile fragmentation and neutrons, it is crucial to perform a study on purely magnetic memory array. Indeed, recoil atoms from MRAM stack layers may be a threat for surrounding devices. For this reason, a clear

understanding of secondary products energy and range could improve the IC design layout step, where the placement of transistors and spintronic devices at different metal levels has to be done. The highest LET available at the facility was chosen to demonstrate radiation hardness even in worst case conditions. Accordingly Xenon ions accelerated at 995 MeV with a fluence of 10^8 ions/cm^2 were chosen. The high fluence value was chosen not to simulate any in-flight condition, but to have a reasonable chance of hitting the targets on the test vehicle.

4.3.1 Device Under Test

In this study, two groups of STT-PMA devices were considered: the first consists of 4 memory matrix samples. They were fabricated at a Spintec Industrial partner Laboratory using the most advanced CoFeB-MgO technology and they will be investigated from the viewpoint of their SEU tolerance. As depicted in Fig. 86, each sample has a cross bridge structure of two metal wires for the top and bottom electrodes, which will be used to make four-terminal measurements.

The first group PMA-MTJ samples have different size resulting in a difference in the main MTJ parameters, as detailed in Table 4.3. They were received naked at our Laboratory. After a careful microscope observation we create a power point view of each matrix by indicating in red the part of the circuit which appeared defective. Then, as shown in Fig. 87 a wire bonding plan was made for each spintronic matrix. This technical file was sent together with the naked circuit to be wire bounded. According to the number of signals and circuit's dimensions we choose as package the PGA 84. A PCB has been designed and it has been fabricated to support the PMA-MTJ samples and all the connectors compatible both with Laser and Heavy ions test environment. Particular attention was given to the position of all connectors placed on the bottom of the boards to ensure the correct exposure to the laser beam and avoid wire crossing and twist for the vacuum room in UCL. Additionally, the board was designed to host 3 circuits at the same time, in order to maximize the number of circuits exposed in the same moment to heavy ion irradiation.

To program the MTJ arrays the pad corresponding to V_{STT+} and V_{STT-} will be properly driven, trough the PCB, by the use of the digital test card DPIN96 of the D10 Diamond Test machine, by means of a set of instructions written in the STIL (Standard Tester Interface Language) Syntax. By the application of a voltage pulse of 0.9 V for a mean time of 5 ns all devices will be programmed in the anti-parallel state. Since the energy to pass from 1 to 0 is lower that the one needed to flip the bit in the opposite direction, we ensure, with this choice, to be in the worst case, i.e. the easier to be switch due to Single Event Effect (SEE).

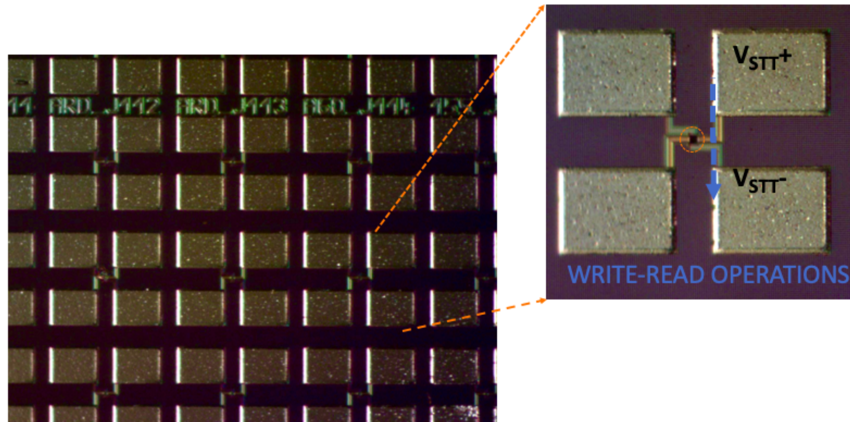

Figure 86: Photomicrograph of the first group purely magnetic STT matrix. In the zoomed part the 4 MTJ pad and the MTJ device are highlighted.

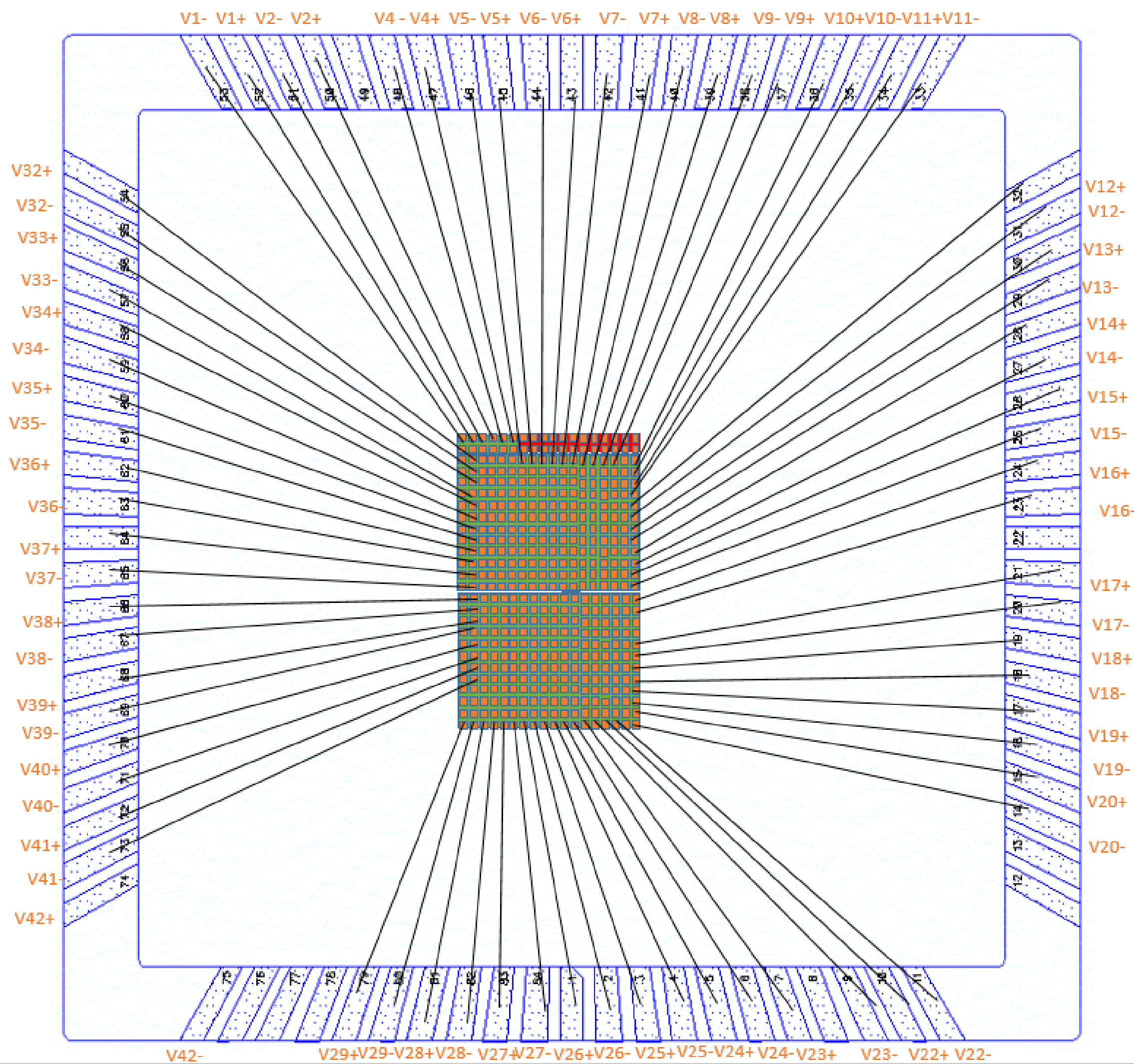

Figure 87: Wire bonding diagram for one of the 16 naked MTJs matrix. The red zone were not bonded because of some defective devices.

The second group of devices intended to be investigated from the structural modification point of view by means of Transmission Electron Microscopy (TEM) before and

Table 4.3: Magneto-electrical parameters of the different investigated samples

Parameter	Symbol	SPINTEC Partner Value range	SPINTEC Value range
Critical Diameter [nm]	$\mathcal{CD}$	50-200	180-300
Tunnel Magnetoresistance	$\mathcal{TMR}$	50-150	50-150
Barrier Thickness [nm]	$\mathcal{T}_{\text{ox}}$	0.8-1	1.2-1.3
Resistance area Product [$\Omega\mu\text{m}^2$]	$\mathcal{RA}$	4	6

after irradiation.

These films are based on SPINTEC's stack and fabricated by SINGULUS Technology.

The MTJ nano-pillar typical parameters are highlighted in Table 4.3. The expected TEM observable radiation's effects are:

- structural modifications at the interface Antiferromagnetic-Ferromagnetic (AF-FM) and FM-Insulator that could lead to switching voltage modifications.
- structural modification of the barrier with or without Oxygen depletion that lead to TMR reduction

4.3.2 Irradiation campaign set-up

Radiation test experiments will be executed at the UCL (Université Catholique de Louvain), Cyclotron of Louvain-la-Neuve. For this experiment we use $^{124}\text{Xe}^{35+}$ irradiation. The beam has a diameter of 25mm and a homogeneity of 10%. The $^{124}\text{Xe}^{35+}$ beam is accelerated at an energy of 8 MeV/u, thus achieving a finale kinetic energy of 995 MeV. Since our target in not Si we will not report classical LET data for this ion. The upset cross section per bit will be calculated as:

$$\sigma = \frac{N_{\text{SEU}}}{N_{\text{bit}} \cdot \phi}$$

Where N_{SEU} is the total error number, N_{bit} is the total number of bits, and ϕ is the fluence. Instead to continually change the LET at normal incidence it is more suitable to rotate the target by remembering that the effective LET of the impinging particle is inversely proportional to the cosine of the incidence angle. A tilt of 30 degree will be performed for these motivations. Concerning the fluence we will start with a low flux of $5 \cdot 10^3$p/cm^2/s and then we will rise to higher fluencies until reaching a fluence of 10^7p/cm^2/s. This is due to several motivations: achieve an homogeneous strike probabilities over the DUT for a given LET, increase the probability to trigger a SEE. Actually, we expected to detect a rare effect, thus all the technical precaution, as for example shielded cable and reduction of parasitic effect have been taken into account in the experiment setup preparation. The radiation effects will be inferred from the static current voltage characteristics measured

in situ both in real time (dynamic measurement of the MTJ resistance on the majority of the devices) both before and after irradiation (static measurement on a small percentage of the device.). Fig. 88 shows the prepared test bank, where the Diamond test machine is the test machine previously described.

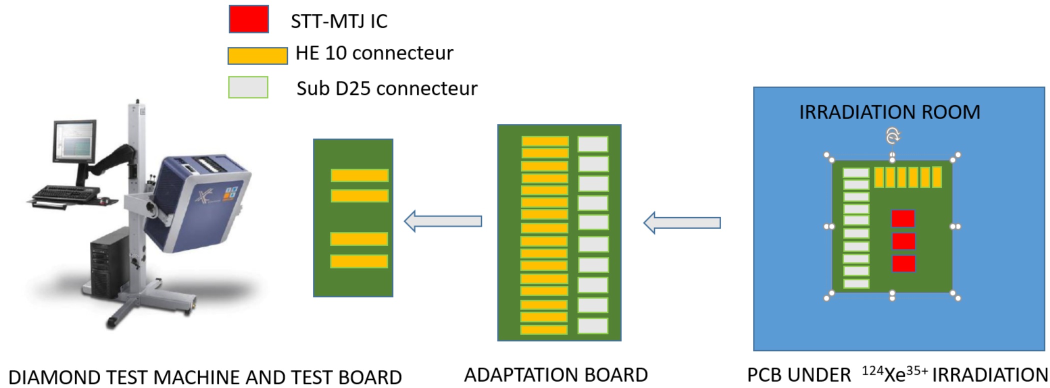

Figure 88: Experimental test bank for the real time monitoring of the I/V characteristic during devices exposition to heavy ion

4.3.2.1 PCB and adaptation cards

Fig. 89 details the irradiation room at UCL facility. The chamber has the shape of a barrel stretched vertically only. One side flange is used to support the board frame (25 X 25 cm) and user connectors. The chamber is equipped with a vacuum system. In order to monitor the evolution of the MTJ electrical parameter under irradiation 2 boards have been designed as depicted in Fig. 90. The first one is the PCB: it can host 3 circuits in order to maximise the number of irradiate circuits at one time. We properly choose the connectors and shielded cables to be able to monitor the signals from the outside. However an adaptation card was also designed to make it possible the compatibility between our test board and the Sub D 25 connectors. Fig. 91 shows the two boards constructed according to the given specifications.

Figure 89: Heavy ion irradiation room at UCL facility

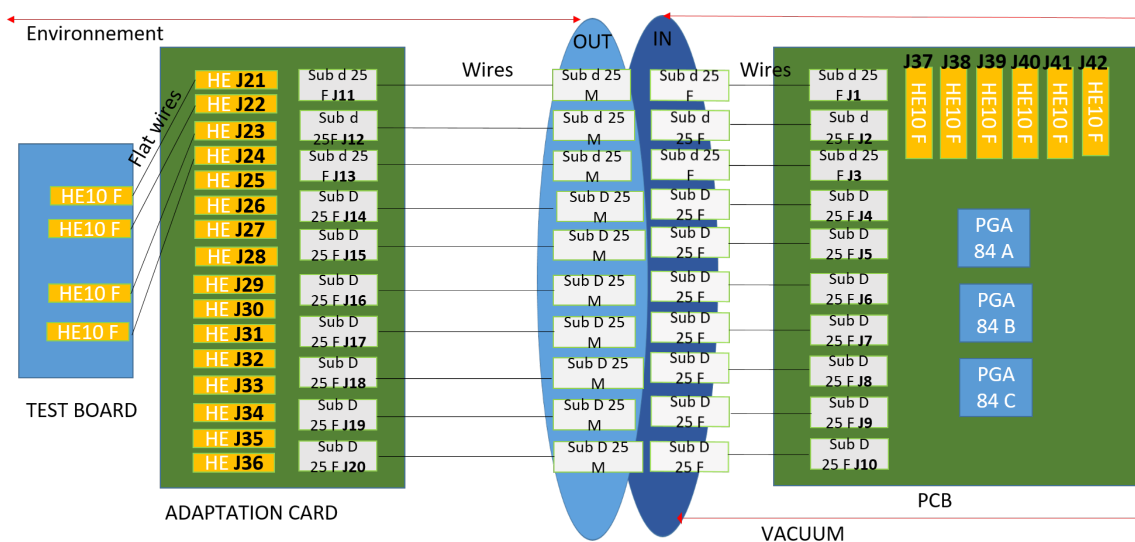

Figure 90: Schematic of all the electrical components needed for the irradiation experiment.

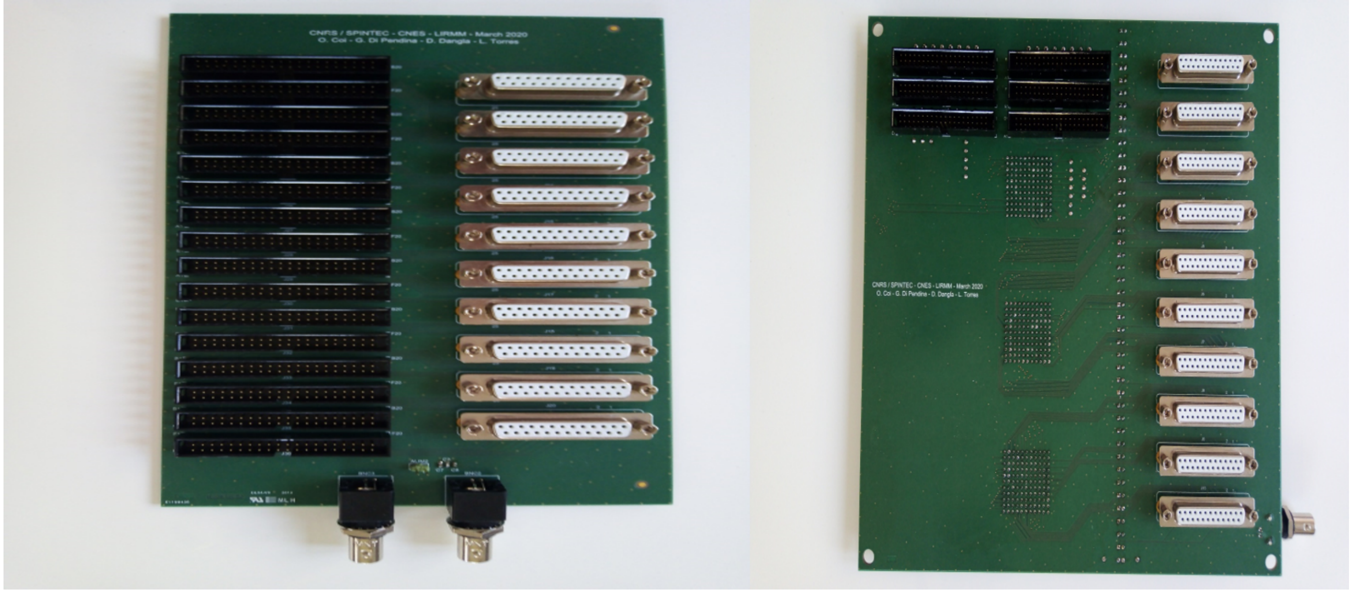

Figure 91: The two fabricated boards.

PCBs were ready in March 2020, and all the material have been bought, unfortunately this experiment did not take place because of Covid pandemics. The wire bonding of the circuits is still undergoing in the manufactory.

4.4 Static Irradiation Experiment

This chapter explores the irradiation response of purely magnetic devices with size ranging from 20 nm to 150 nm, without any bias voltage applied. This way, we aim at observing the intrinsic robustness of spintronic devices without other stress sources and regardless from the peripheral circuit. Additionally this allow us to send the circuits to the UCL facility without needing to move there.

Fig. 92 a represents the memory matrix layout made up of 9x12 STT-devices. Fig. 92 b and Fig. 92 c detail the cross bridge structure of two metal wires for the top and bottom electrodes, which will be used to perform two-terminal measurements prior and after the irradiation. Indeed, to program the MTJ arrays the two contact pads, corresponding to V_{STT+} and V_{STT-}, will be properly driven by means of an electrical probe. The electrical characterization of the wafer has been performed with magnetic field switching instead of current switching, this way reducing the impact of self heating degradation [120] on the circuit before irradiation. A fully automatic measurement wafer probe station was used for this purpose. It is equipped with an electromagnet which applies magnetic field in a direction perpendicular to the plane of the wafer. Multiple successive resistances versus field hysteresis loops have been performed for each single MTJ measurements (12 loops at a frequency of 5 Hz) in order to account for thermal stochastic fluctuation. We programmed all the samples under a field of 2000 Oe (almost the double of the coercitivity

value) so that the SAF, the RF and the FL ended up well aligned. Thereby the stray field is well compensated, resulting an hysteresis loop almost centered around zero: due to process limitations a negligible offset field (less than 100 Oe) is still present in most of the samples.

Due to the beam's diameter and irradiation time constraints, two groups of devices were selected based on high TMR and high H_c criteria after the whole wafer characterization. Each group consists of 6 memory matrix , each matrix including 128 STT-MTJs organised in 12 columns and 9 rows depending on their sizes. This results in a huge dispersion of the main device parameters, as detailed in Table 4.4 where the PMA-MTJ nano-pillar typical parameters are highlighted. A set of MTJs from the same wafer will not be irradiated and serve as control-group. All devices have been programmed in the anti-parallel state which is the less stable state for these samples. A read check was performed after programming concluding in the mapping of 1.8% altogether not working devices. Actually, a zero field measurement allows to sense the resistance by applying a voltage of $\sim 30\ mV$ to the devices. Since the critical current to flip the value from "1" to "0" is lower than the one needed to flip the bit in the opposite direction, we ensure, with this choice, to be in the worst case, i.e. the easiest to switch leading to an SEU occurrence.

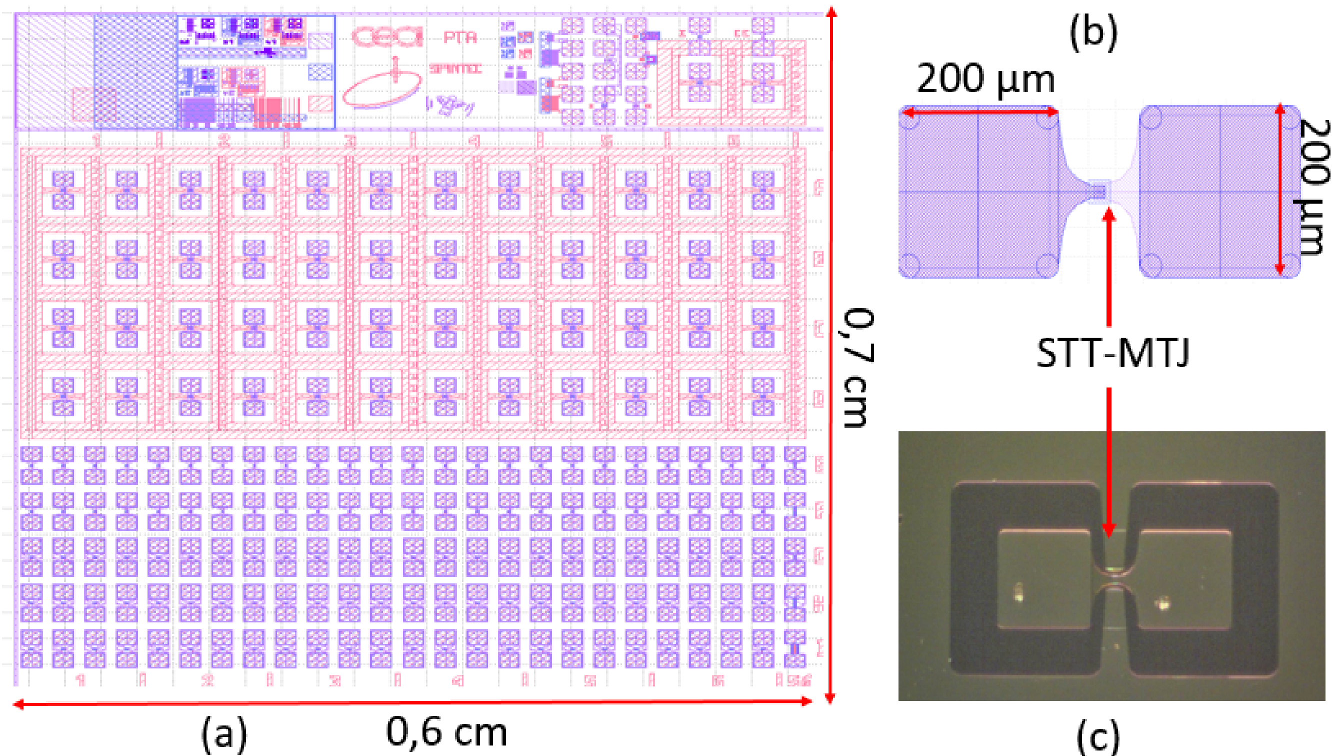

Figure 92: Layout of the magnetic STT-MTJs memory matrix considered for this study (a). Layout view of the single device (b) Photomicrograph view of the single device (c).

Table 4.4: Magneto-electrical parameters of the investigated samples

Parameter	Symbol	Group1 Value range	Group2 Value range
Critical Diameter [nm]	$\mathcal{CD}$	20-150	20-150
Tunnel Magnetoresistance	$\mathcal{TMR}$	30-63	30-58
Barrier Thickness [nm]	$\mathcal{T}_{\text{ox}}$	0.9-1.1	1.2-1.3
Resistance area Product [$\Omega\mu$m^2]	$\mathcal{RA}$	3.3-12	4.8-18.8

4.5 Irradiation campaign

The experimental radiation campaign was performed at the UCL Cyclotron (Université Catholique de Louvain), of Louvain-la-Neuve in July 2020, due to some restrictions, the only possibility was to do a static test, i.e. devices were tested before and after the irradiation but not during the experiment. For this experiment, the chosen ion species is ^{124}Xe^{35+}. The ion beam has a diameter of 25 mm and a homogeneity of at least 90% as reported in Fig. 93. The ^{124}Xe^{35+} beam is accelerated at an energy of 8 MeV/n, thus achieving a final kinetic energy of 995 MeV, providing the highest LET value achievable at the facility.

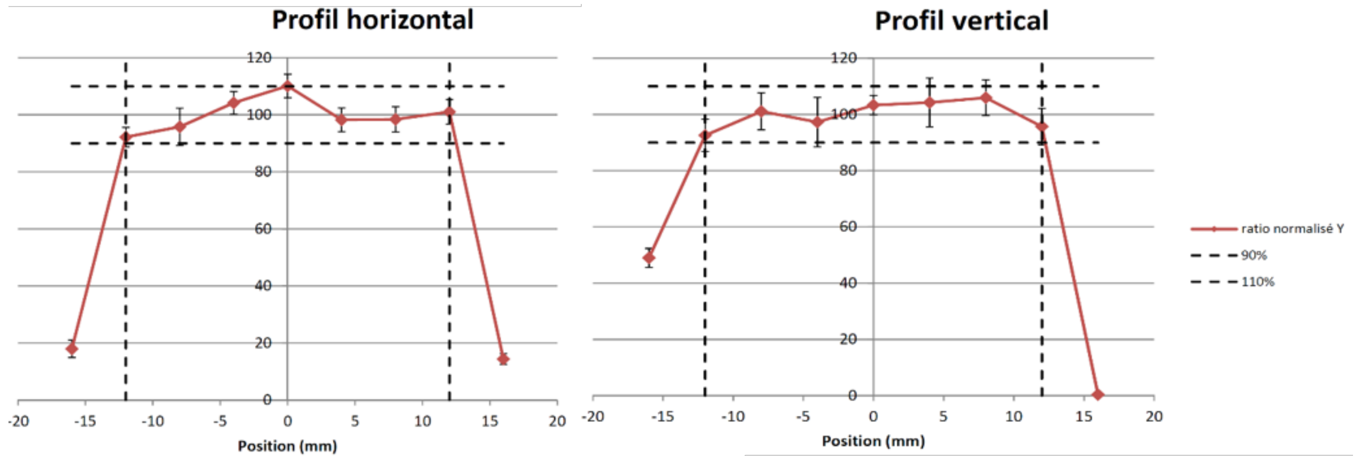

Figure 93: Beam homogeneity profiles

Although our target is not Si we report classical values for reader reference: a LET of 62.5 MeV-cm^2/mg and a range of 73.1 μm as indicated in the facility's irradiation report. Table 4.5 details the irradiation conditions reached during the experiments on the two groups (RUN 1 and RUN 2) corresponding to the irradiation of the first and second MTJs arrays). Fig. 94 shows the two samples fixed on the proper support as they were sent to the irradiation facility togheter with the coordinates of the beam center. Fig. 95 shows the centered beam during the irradiation of the first sample as reported in the Irradiation report we received after the experiment.

Table 4.5: Irradiation conditions during the experiment

Run	Fluence [ions/cm^2]	Elapsed time [s]	Mean flux [ions/cm^2/s]
1	2.67 10^8	17229	15480
2	2.60 10^8	16838	15422

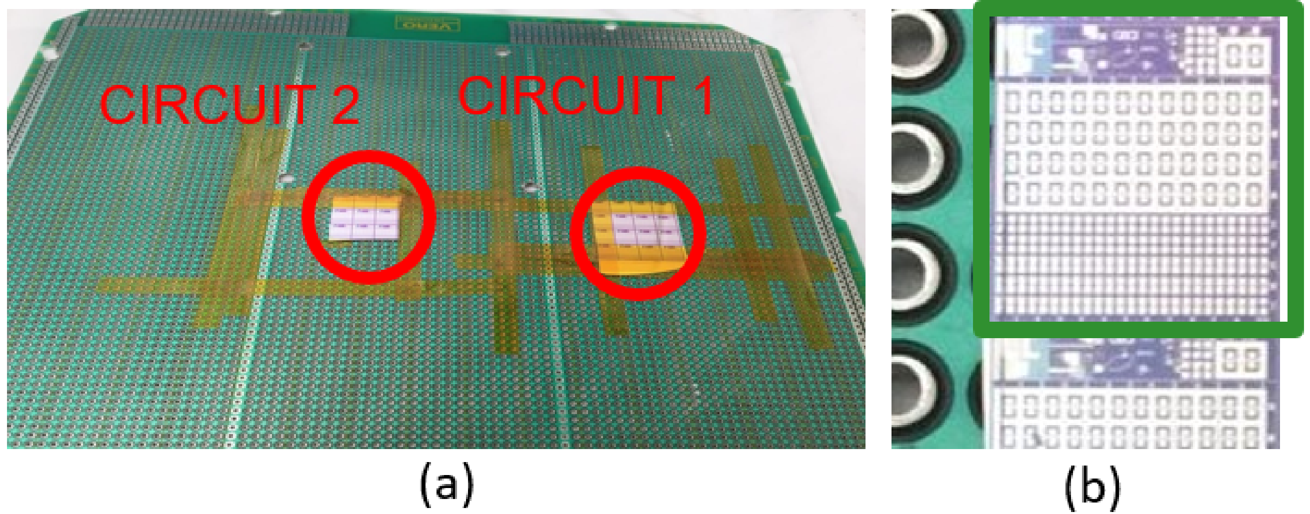

Figure 94: The support with the 2 circuits prior to the irradiation (a) A zoom on each MTJ matrix (b)

Figure 95: Irradiation of circuit one. The beam in centered on the useful area, i.e not covered by the scotch (see Fig. 94)

4.5.1 Analysis of Heavy ion irradiation effects

In order to do a consistent analysis of the post irradiation results we compute the irradiation-induced change, ΔX, in the mean value of the parameter X for all the pMTJ as:

$$\Delta X = \frac{1}{N}\sum_{i}^{N} X^{after,i} - X^{before,i} \tag{4.10}$$

Where N represents the total number of MTJ in the set and i is their index. The standard deviation gives a measure of the error in detecting radiation-induced change of parameter ΔX and is computed as:

$$\Sigma_{\mathrm{X}} = (\frac{1}{N-1}\sum_{i}^{N}((X^{after,i} - X^{before,i}) - \Delta X)^2)^{\frac{1}{2}} \tag{4.11}$$

We made a comparison among these two statistical indications to conclude if the error induced by irradiation can be distinguished from the highly dispersed MTJ parameter values.

4.5.2 Test of read operation

The first check made on the irradiated devices was a test of the read operation. For the resistance parameter, the σ value has been found almost 3 times larger than the Δ value. In a graphical way, this can be also seen in Fig. 96 were a Gauge Variability chart is displayed for different sets of MTJs depending on their size. It is evident that the resistance variation before and after irradiation fall in the inter-quartile range (IQR) variability of the same parameter before irradiation.

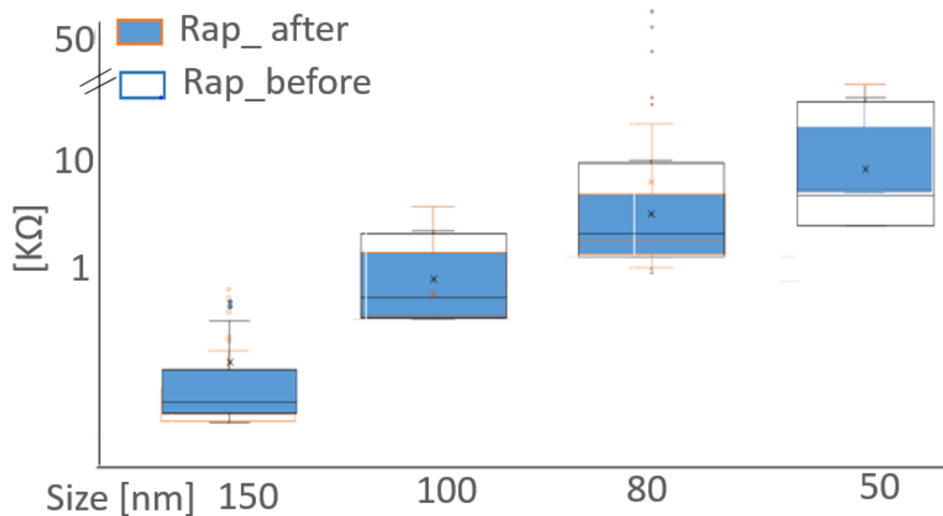

Figure 96: Distribution of Resistance parameter before and after the irradiation.

Table 4.6: Max and Min percentile variation of R_{min} among the different tests

	Test A^r	**Test B^r**	**Test C^r**	**After/Before (mean)**
Min.	-0.03%	+0.03%	+3.18%	-0.21%
Max.	+0.02%	+0.80%	+7.24%	-8.88%

As next step, we verified if the resistance variations due to irradiation are discernible from the ones due to measurement error. In order to identify and isolate the contributions of systematic error sources we performed on the same irradiated sample:

- a motion of the probes up and down on the MTJs pads and a consequent reading (4 times) (test A^r).
- a cycle of 4 readings without moving the probes (test B^r).
- repetition of test B after one month (test C^r).

It is worth to remember that each read/write operation is a 12 loops measurement. We find out that the changes in resistance before and after irradiation are bigger than the variation between test A and test B. Nevertheless, they are still comparable with the variation found in test C, as reported in Table 4.6. These considerations on our experimental limitations, do not allow us to conclude on resistance fluctuation, even though the observed resistance variation of 8.88% is almost 10 times larger that the one reported in [62]. In their experiment after 15 MeV Si ion irradiation of 70 nm diameter MgO single MTJ, a resistance change of 1% was noticed. However, the validity of this comparison is questionable, since both the DUT dimensions and the irradiation conditions were different. Even if we could not conclude on the resistance variation, a count of the occurred hard errors was possible: we notice some MTJs (12 for RUN 1 and 22 for RUN 2) sensed as short circuit during all tests. Thence, the cross section [cm^2/bit] was calculated as the number of hard errors

$$\sigma = \frac{N_{\mathrm{SEU}}}{N_{\mathrm{bit}} \cdot \phi \cdot \cos(\theta)}$$

Where N_{SEU} is the total number of Single Event Upset, N_{bit} is the total number of functional bits, ϕ is the ion fluence and θ is angle of incidence of the beam relative to the DUT that, in this experiment, was kept equal to 0. We obtained a cross section equal to $3 \cdot 10^{-10}$ cm^2 and $5 \cdot 10^{-10}$ cm^2 for RUN1 and RUN2 respectively. This slight difference was due to the different number of functional bits and different number of hard errors. Since we have excluded soft breakdown processes and pad influence, we may link this hard error occurrence to a direct MTJ strike.

4.5.3 Test of Write operation

During this test we focused on the most important parameters that characterize the hysteresis loop stability: the coercive field and the offset field. The transition from R_p to R_{ap} allows also to observe TMR variation during this test. Fig. 97 shows for the TMR parameter the same trend noticed for the resistance parameter, where the magnitude of the standard deviation makes the irradiation effect quite negligible. Interestingly, a TMR augmentation for the two lowest quartiles seems to suggest an annealing-like effect on 50% of the devices. Besides, we observe a clear decrease in H_c and a clear increase in H_{off}: for both parameters, the variations exceed one standard deviation so they should be induced during the irradiation experiments as depicted in Fig. 98 and Fig. 99 respectively.

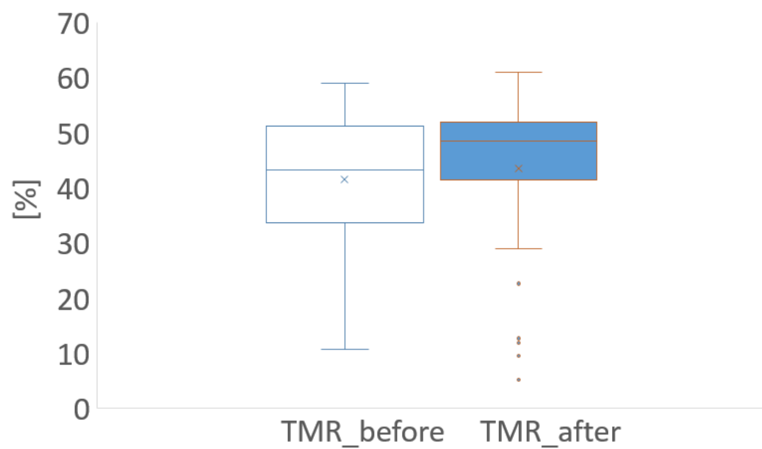

Figure 97: IQR distribution of TMR before and after irradiation.

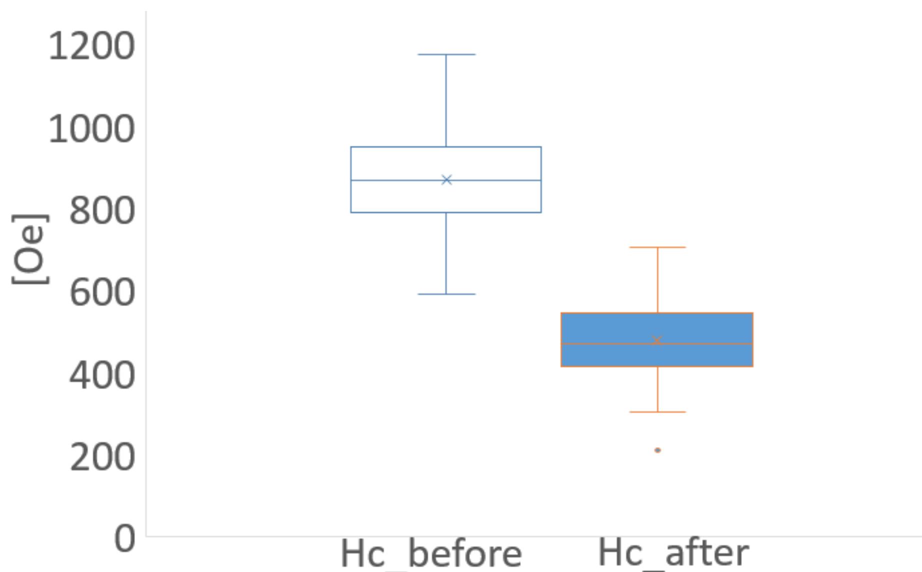

Figure 98: IQR distribution of coercive field before and after irradiation. Data referred to 80 nm diameter junction.

As for the reading test, we wrote the irradiated circuits according to the following

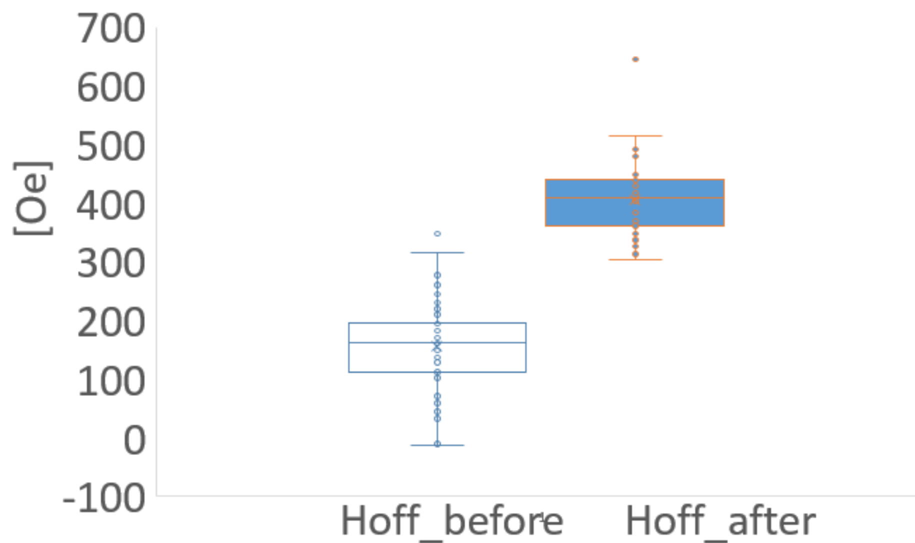

Figure 99: IQR distribution of offset field before and after irradiation. Data referred to 80 nm diameter junction.

protocol, in order to quantify the systematic error contributions:

- a 4-writing cycle which simulates an error in the placements of the magnets that generated the needed field (1mm each time) (Test A^w).
- a 4-writing cycle without moving the probe (Test B^w).
- repetition of test B after one month. (Test C^w)

A problem occurred during Test C^w measurements: a considerable quantity of MTJ which were correctly readable after irradiation (test A^r and B^r) were then not re-writable because they appeared as open circuits from the test machine: this was imputable to a degradation of the metal pads, noticeable by the microscope observation. Indeed, during the measurements, the probe creates holes in the pads which, eventually, result in the impossibility to read/write the MTJ more than approximately 23 times in total (after some adjustments in the position) due to the lack of metal contact. However, the results of these tests are summarized in Table 4.7. They confirmed the systematic error to be irrelevant with respect to the fields variations before and after the irradiation experiment.

A more accurate study on the reported H_c reduction allows us to state that in most of the cases, an hysteresis loop amplitude reduction was due to a remarkable coercive field decrease (in its absolute value) in the transition from anti-parallel to parallel configuration together with an indiscernible variation of the field in the opposite transition. Fig. 100 highlights this occurrence. These variations are characterized by the reduction in the hysteresis loop amplitude and its shift due to the appearance of an uncompensated H_{off} field. It is worth to remember that the STT-MTJ device works under the assumption of having the fundamental ferromagnetic blocks (SAF, reference and free layers) in the

correct alignment, as detailed in the Chapter 1. A substantial misalignment among these magnetizations results in anomalies in the hysteresis loop. Reduced coercivity physically means easier nucleation due to more nucleation sites in the storage layer. Crystalline defects could serve as nucleation sites and reduce the coercivity significantly [129].

According to the approximation in [67], H_c can be defined by:

$$H_c = \alpha H_K - N_{eff} M_s \tag{4.12}$$

Where H_K is the anisotropy field, M_s is the magnetization at the saturation point, α and N_{eff} are microstructural parameters depending on defects and grain alignment H_K. This formula sets H_K as the upper limit of the coercive field value. Since in our measurements M_s did not change we infer that the coercive field lowering should be attributed to H_K reduction. Indeed, an increase of defects at the MgO/FL interfaces reduces the PMA due to its marked sensitivity to general random re-arrangement of atoms and displacement [66]. This is not surprising, since every change in the average atomic distance, globally and locally, alters the orbital overlap of atoms in the lattice, responsible for the PMA phenomenon. These mechanisms could very likely be behind the observed hysteresis loop reduction. Moreover, since the hysteresis loop amplitude appears tight but only the switching field from AP to P configuration is reduced, it is possible to infer that SAF layer degradation occurred favouring an easier switching towards parallel configuration. In this event, a competition between defects creation, interfacial mixing and film thermal stress contributes to degrade the stray field compensation mechanism by promoting, then, the switch from AP to P [54] [45]. Additionally, since part of the PMA originates also in the Co/Pt multi-layer, damages to the SAF contribute to lower the PMA value. This hypothesis is corroborated by the fact that Co is the layer receiving the highest energy deposition as observable in Fig. 71.

Another possible deleterious mechanism could be the Ta diffusion. Actually, because of its high miscibility, Ta is proposed to be replaced by W [19], a material that has also a better thermal conductivity thus can evacuate the heat faster. Since in the stack of the irradiated MTJ there are both W and Ta we can not exclude the occurrence of this phenomenon. On the contrary, we can exclude with certitude that SAF or RL have switched during the irradiation: if this had happened, the hysteresis loop should appear reversed, with AP resistance state at negative field and P resistance state at positive one. In none of our observations such a behaviour was noticed.

During the irradiation test, the final fluence was not very high (i.e. it was not capable of ensuring at least one strike for each MTJ) and the circuit's density was very limited (see Fig. 92 (a)). Therefore we assumed the effects observed in the quasi-totality of irradiated device to be a consequence, somehow, of thermal effects. This hypothesis seems reasonable since reference [41] also proposes that temperature could play a role in the MTJ degrada-

tion under heavy ion irradiation. Thermal spike propagation processes allow us to explain the high percentage of devices that experienced a H_c reduction. Additionally, the heating in the SAF could induce local strains and magneto-elastic effects that degrade magnetic properties. These effects are attributed to differences in the thermal expansion coefficient between multi-layers, and between multi-layers and substrate. They could be driven also by secondary particle production. Indeed, the latter plays an important role since the whole surface has received a strike every 600 nm on average while typical secondary range exceed 1 μm, as already detailed in Fig. 84.

Table 4.7: Max percentile variation of H_{off}, TMR and H_c among the different test

	Test A^w	**Test B^w**	**Test C^w**	**After/Before (mean)**
$\mathbf{H_{off}}$	+9.1%	+1.18%	+3.49%	+146.21%
$\mathbf{H_c}$	+10.06%	+2.62%	+15.03%	-32.83%
TMR	+1.58%	-0.8%	-9.4%	-10%

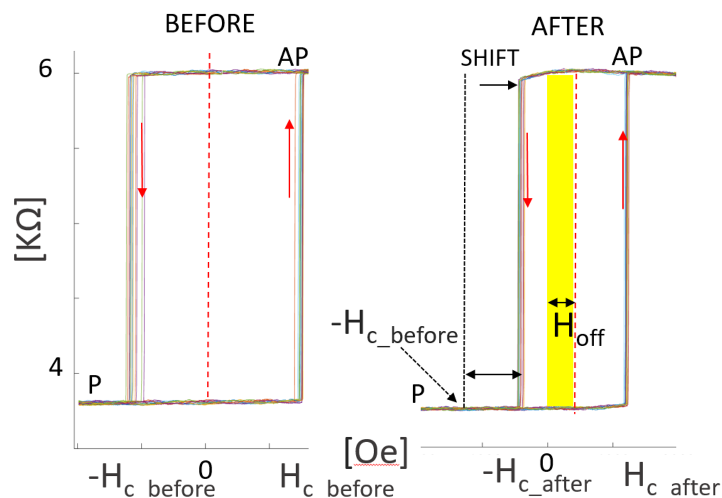

Figure 100: A representative image of the numerous hysteresis loop characterized by a considerable decrease in the AP to P switching field and an imperceptible modification of the field in the P to AP transition.

4.5.4 Annealing of the reference circuit (control-group)

In order to examine the validity of thermal effects hypothesis, an annealing of the MTJs control-group circuit was performed in our Laboratory. Since this control-group has not been exposed to radiation, we aim to observe if changes in the magnetic properties could be induced by a temperature rise below the Curie temperature. The regime of interest is around 200° C, compatible with long-range thermal spike propagation, i.e. emulating temperature experienced in regions tens of nm away from the heavy ion strike point [23].

Testing was performed at 200° C. At this temperature thermal scattering impacts the resistance. Indeed, TMR could be enhanced by cristalline defect annealing, while some magnetic parameters could start experiencing a slight detrimental effects [104].

A 10 minute homogeneous heating was performed on the sample which includes different MTJ sizes, while having exactly the same pattern than the irradiated ones. Plots before and after annealing are reported in Fig. 101 and Fig. 102 for the coercive and offset field values respectively. As expected, the TMR results slightly improved in most of the cases. Interestingly, a similarity in the induced changes by heating and by irradiation is observable. Indeed, plots analysis confirms a general reduction of coercive field due to a remarkable reduction of the switching field from AP to P resistance state. This confirms the P state as favorite due to the unbalanced stray field from the RL that tends to align the FL in the same direction. Device properties are not compromised, but a general drift of H_c and H_{off} is observable as in [43], for a temperature of 350 C. The presence of a small uncompensated H_{off} in the DUT prior to irradiation (as described in section 4.4) may also have played a role in the premature observation of these effects. However, these results confirm the critical role of annealing and explain why so much effort and work are invested in MTJ stack optimization. For example, reference [12] demonstrates that inserting an ultra-thin (0.4 nm) layer of Cu enhances the effective anisotropy of CoPt multilayers: for an annealing temperature of 200C it has reported to be almost doubled. Moreover, the number of CoPt repetition and their thickness play an important role in the SAF thermal stability [43].

In conclusion, it seems reasonable to argue that the effects detected on the MTJ magnetic properties after irradiation are more likely related to heating effect due to thermal spike propagation than to a punctual ion strike.

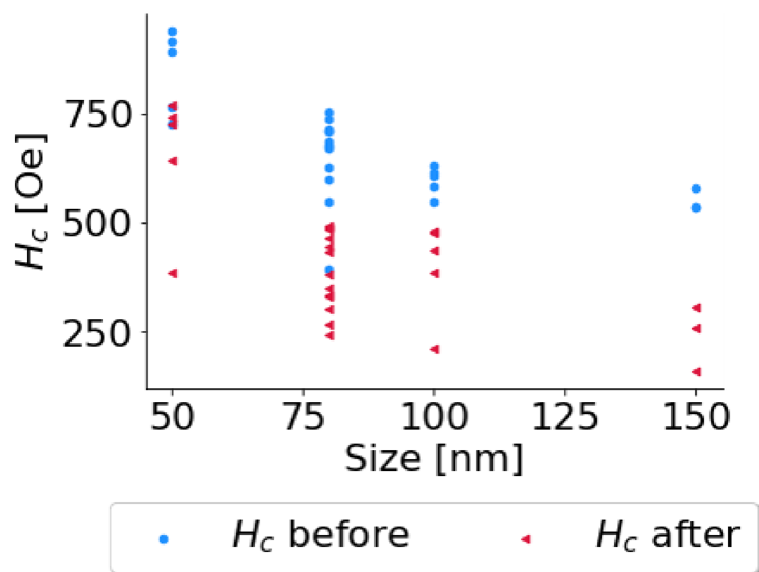

Figure 101: Coercive field parameter before and after temperatures annealing for various MTJs from the control-group.

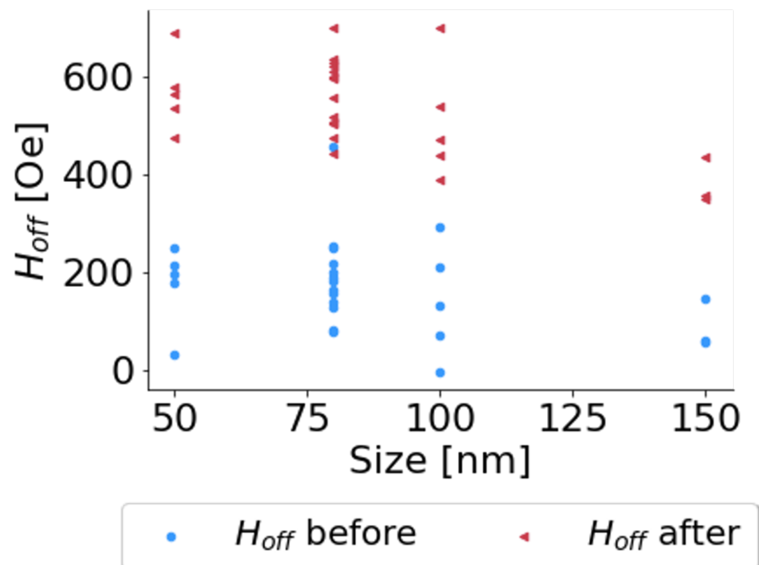

Figure 102: Offset field parameter before and after temperatures annealing for various MTJs from the control-group.

4.6 Conclusion

In this chapter, we propose new interpretations for some traditional radiation-induced parameters, trying to translate them in the Beyond-CMOS paradigm of spintronics.
We show that explaining the STT-MTJ bit flip associated to particle hits with Spin-Transfer Torque switching mechanism in CoFeB is almost impossible. Thermal effects were suggested instead to be responsible of bit flip and MTJ magnetic properties degradation. Thermal spike model was used to estimate the temperature reached during irradiation and its radial extension. This was possible using data such as MTJ LET profile, deposited charge, and secondary ion production, data provided by STT-MTJ model simulation in TRADCARE® environment.
Thermal event upset (TEU) is a proposed new nomenclature to describe an asymmetrical upset, always resulting in logic state '0", that occurs each time the MTJ temperature exceeds the Curie temperature. Thermal stability factor is the other critical parameter, since strictly related to the required retention time and dramatically affected by MTJ size scaling and temperature rise. Moreover, thermally-induced switching probability is estimated as a serious concern since thermal spike model suggests heat waves can propagate for hundreds of nanometers. Therefore after an ion hit, the MTJ temperature could be increased without being directly hit by the incident ion. Even before the occurrence of a TEU, our results show that the main magnetic MTJ properties can be affected even at temperature below T_c. These considerations lead to extend the sensitive volume definition over the entire MTJ stack. In conclusion, this study highlights the need of new STT-MTJ stack solution, specific for harsh environment, to mitigate the deleterious im-

pact of scaling on STT-MTJ thermal stability. Additionally, as the FL CoFeB thickness shrinks, its Curie temperature decreases: inducing a TEU thus becomes even easier and more probable. Therefore, with device scaling multiple TEUs could occur as technology gets denser and neighbour MTJ closer to one another.

The irradiation of the multi-layer structure with 995 MeV $^{124}Xe^{35+}$ions indicates a negligible SEE sensitivity and no detrimental effects of statistical significance on electrical properties. Instead the TMR is slighty increased in the lowest half of the IQR ranges, suggesting an annealing-like effect on the MgO crystallinity.

Concerning the magnetic properties a general reduction in the coercive field involved in the AP to P switching, combined with an increase of the offset field have been detected. Depending on the intensity of these phenomena, write operations stability could be threatened by the observed hysteresis loop degradation due to the reduced stability of the AP state. This drift could likely be symptomatic of degradation mechanisms that take place in the device stack such as thermally activated diffusion of Ru and Ta, the formation of pinholes in the Ru SAF spacer and the miscibility of Co/Pt SAF multi-layer. Indeed, the large quantity of affected MTJs could not be all related to direct ion strike occurrences. Due to the limited fluence reached during the irradiation experiment, and the lack of high density MTJ matrix in the irradiated circuits, another mechanism, most likely a thermal effect, could have determined the observed degradation. This hypothesis seems to be confirmed by the annealing of the MTJ control group that showed analogies in the magnetic properties drift together with a slight improvement of TMR.

Hence, heavy ion irradiation may affect MTJs also by thermally activated and thermal induced effects rather than exclusively by direct ion strike. Magnetic properties modifications occur before electric properties degradation.

These conclusions are limited to MTJ components: future studies will need to include peripheral circuitry to gain insight into overall memory performance.

CHAPTER 5

Proton irradiation effects

5.1 Introduction

This chapter presents proton experimental irradiation campaign on STT and SOT devices. These tests were performed in the same irradiation facility than the previous chapter (UCL) and in the same "static" configuration, which allows us to properly send the circuit without incurring in physical journey restrictions.

To the best of our knowledge there is only one study on the irradiation of PMA-MTJ SOT devices and none on the protons irradiation effects, which is the focus of this study. Indeed in [6] it was observed that gamma ionizing dose up to 1 Mrad(Si) does not alter the magnetic switching behavior, while very high Ta^{1+} ion irradiation (over 10^{12} p/cm^2) modified some magnetic properties.

5.2 Device under test

In this study, we irradiated both SOT and STT devices so that we can make a comparison on the irradiation response of these two technologies. The devices were organized in 2 groups: first group was irradiated with 62 MeV protons to a fluence of 1.2 x 10 ^{11} p/cm^2 (F1), while a fluence of 1.2 x 10^{12} p/cm^2 (F2) was chosen for the second group. The flux was set to the maximum value the facility could provide: 2 x 10^8 p/cm^2/s. Each group of SOT and STT consisted of 25 magnetic elementary memory arrays arranged in 6 column x 9 rows. Each row hosted different MTJ sizes as highlighted in Table 5.1. They were fabricated by a SPINTEC partner to guarantee an industrial process using the most advanced CoFeB-MgO technology.

As depicted Fig. 103 samples have a cross bridge structure of two metal wires for the top and bottom electrodes, which have been used to make three-terminal measurements. Indeed, prior to irradiation a set of measurements were done:

- The resistance and TMR
- The coercive field H_c, i.e. the field value needed to switch the magnetization from one stable state to the other, which in a perfectly symmetrical situation, corresponds to one half of the whole hysteresis loop width. Its value is considered as positive for the P to AP transition, and negative conversely.

Table 5.1: Magneto-electrical parameters of the different investigated samples

Parameter	Symbol	SOT Value range	STT Value range
Critical Diameter [nm]	$\mathcal{CD}$	60-200	60-1000
Tunnel Magnetoresistance [%]	$\mathcal{TMR}$	10-90	15-140
Barrier Thickness [nm]	$\mathcal{T}_{ox}$	0.8-1	1.1-1.3
Channel thickness [nm]	$\mathcal{T}_c$	4	-
Channel width [nm]	$\mathcal{W}_c$	50	-
Channel length [nm]	$\mathcal{L}_c$	180	-
Channel resistivity [Ω cm]	ρ	20	-

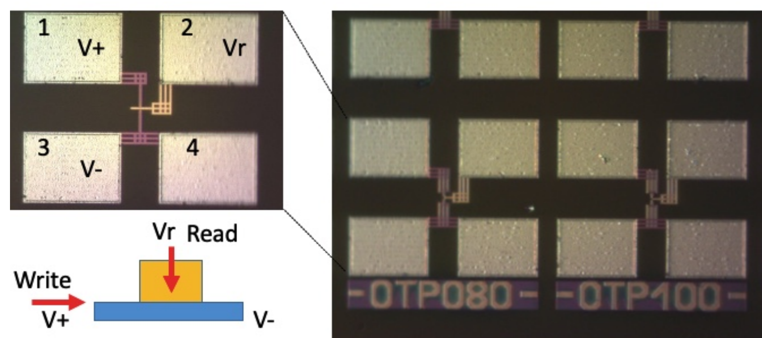

Figure 103: Photomicrograph of the purely magnetic SOT memory. The 4 pads and the MTJ device are highlighted as well as the correspondence with the device scheme.

- The offset field H_{off}, which quantifies the hysteresis loop shift with respect to a symmetrical situation.

Each measurement is the result of a 300 times cycle performance, which were made in partnership with Hprobe, a startup launched by Spintec leader in characterization and testing of MRAM. All the MTJs were set in the parallel state (R_{min}) because in these devices, by construction, the favored (i.e. more stable) configuration is the antiparallel (R_{max}). This is due to choices made at the level of the multi-layer stack to compensate dipolar fields across the device.

The proton beam has a diameter of 8 cm ad and squared shape: it was centered on the the blank circular wafer which hosts the 2 spintronics circuits, as reported in Fig. 104and in Fig. 105. the two support illustrated in these pictures have been screwed onto the vacum chamber support already illustrated in Fig. 89 in the previous chapter.

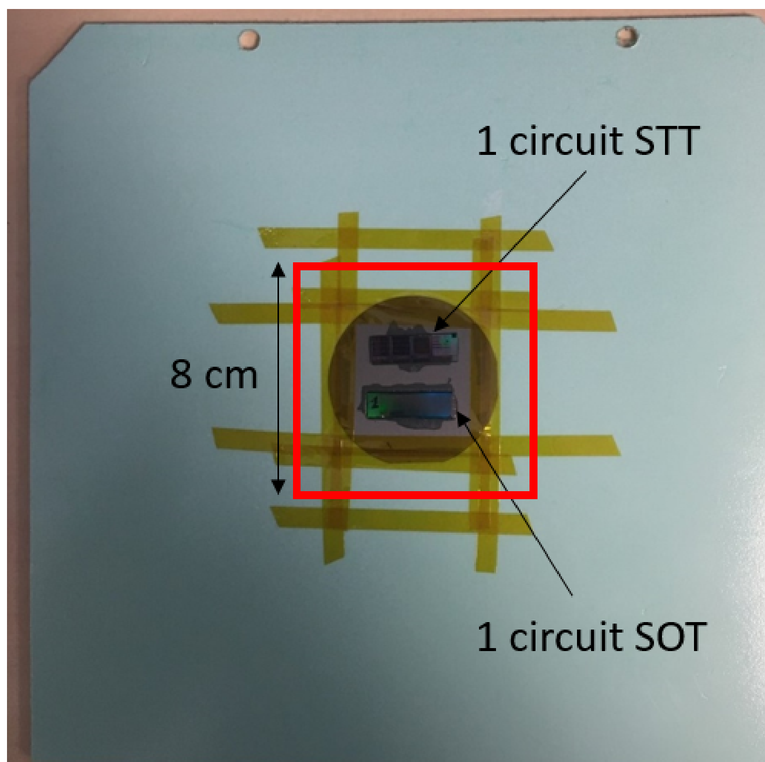

Figure 104: Support irradiated at the fluence F1. The wafer has a diameter of 5 cm, the squared proton beam of 8 cm.

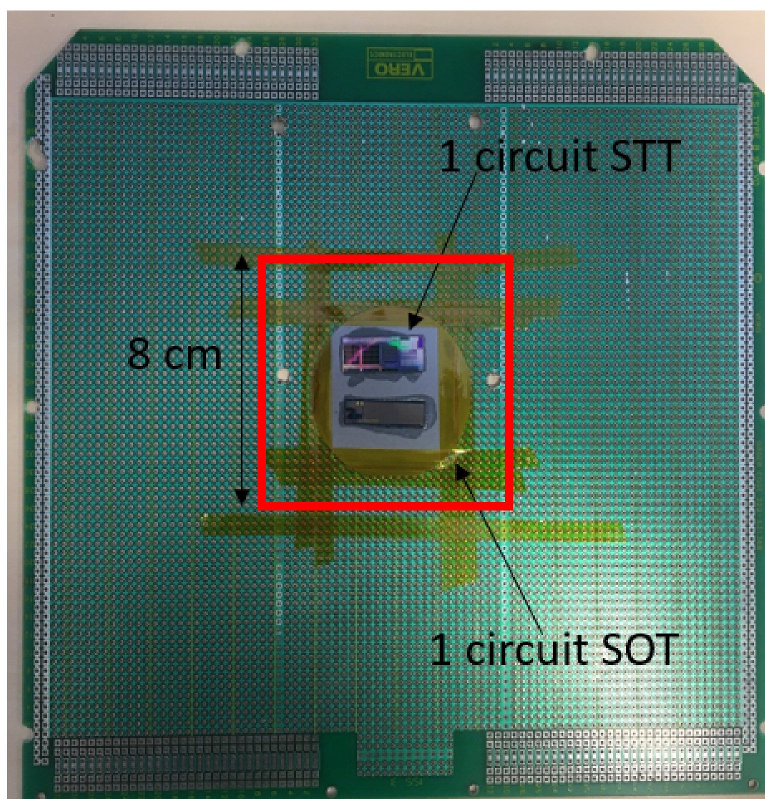

Figure 105: Support irradiated at the fluence F2. The wafer has a diameter of 5 cm, the squared proton beam of 8 cm.

5.3 Experimental result

Devices exposed to the lowest proton fluence do not show any relevant change in their parameters. Then we will drown some considerations on the F2 exposed devices. Fig. 106 and Fig. 107 show the IQR distribution and a one by one representation of the same parameters before and after the irradiation for a 60 nm dimater STT devices. In particular, as highlighted in Fig. 107 the first 20 devices charactrerized by a resistance around 3 KΩ experience no change while the ones with a resistance around 20 KΩ shown an increased resistance after the irradiation. Our knowledge of these devices seems to suggest that a resistance of 3 KΩ is too small expecially if compared with Fig. 108 and Fig. 109 where for a 75 nm MTJ size the range is 4-7 KΩ. However, a resistance higher than 20 KΩ seems to be to large. In conclusion, we do not feel confident to conclude on the 60 nm devices because of the wide range of the before irradiation measurements. However, such a visible variation was not observed in the 75 nm size as already shown neither for higher sizes as Fig. 110 and Fig. 111 reported. Fig. 112 reports resistance inter quartile range (IQR) distributions before (a) and after (b) irradiation at the largest proton fluence for the SOT devices. These evidences suggest that the smaller devices experienced the biggest distribution modifications. However, the overall modification is still negligible.

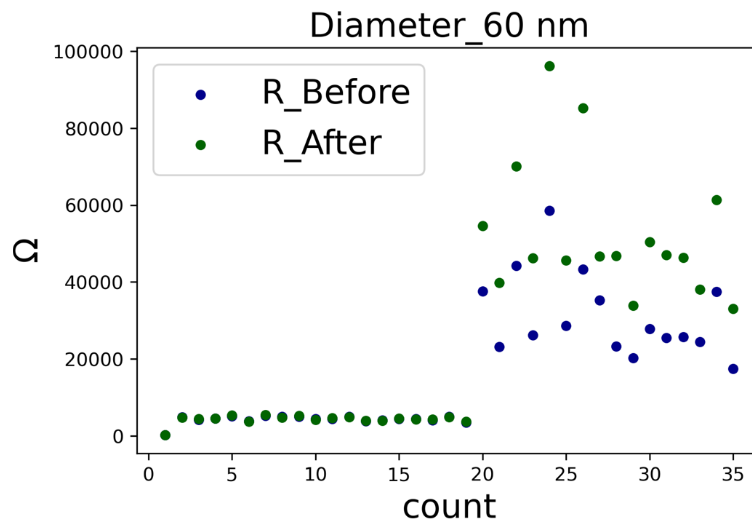

Figure 106: Scattering plot: STT-MTJ Resistance values before and after irradiation.

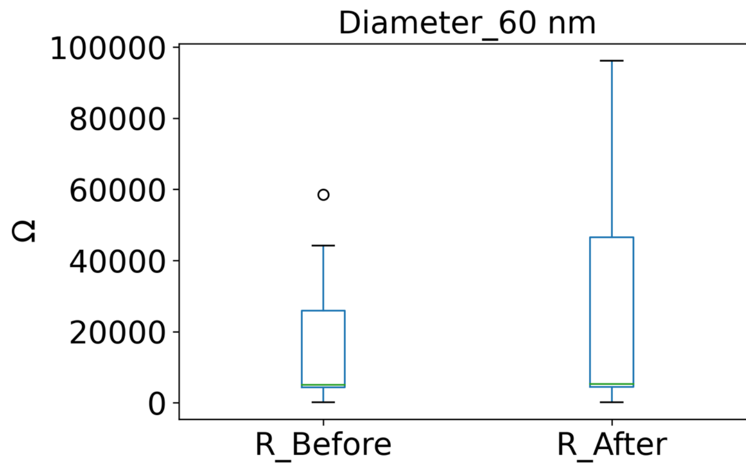

Figure 107: IQR plot: STT-MTJ Resistance values before and after irradiation.

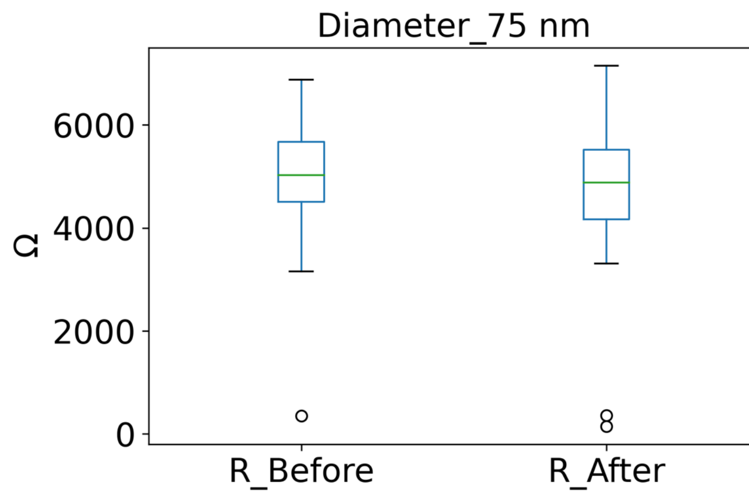

Figure 109: IQR plot: STT-MTJ Resistance values before and after irradiation.

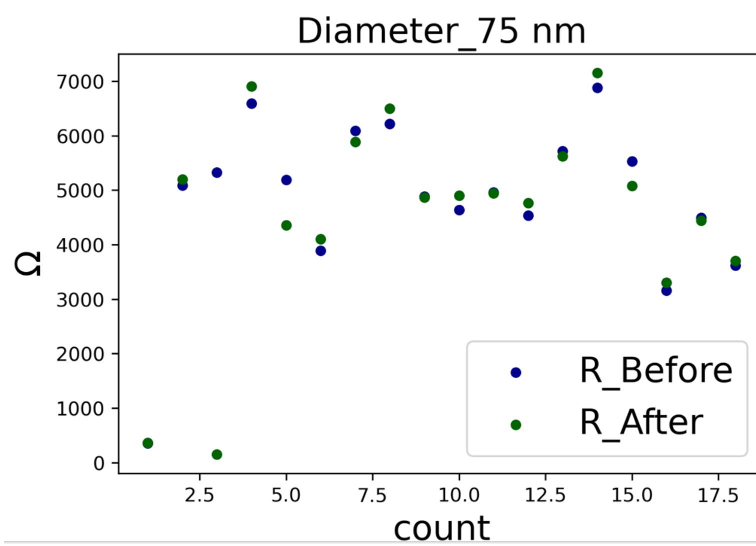

Figure 108: Scattering plot: STT-MTJ Resistance values before and after irradiation

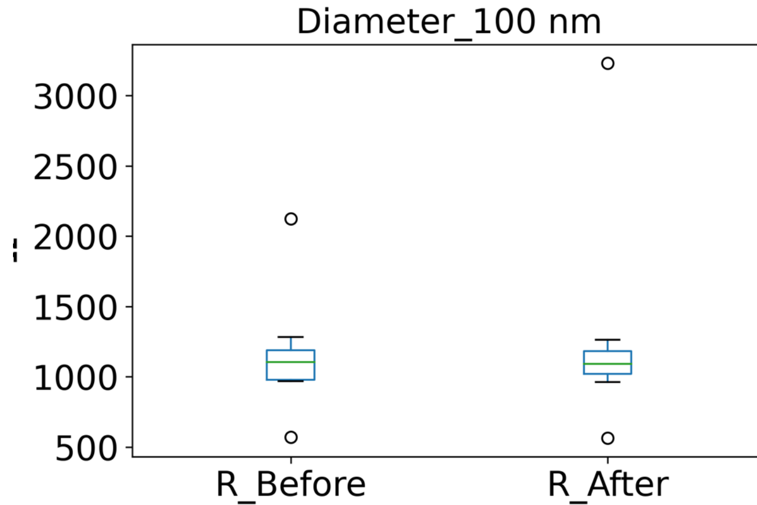

Figure 111: IQR plot: STT-MTJ Resistance values before and after irradiation.

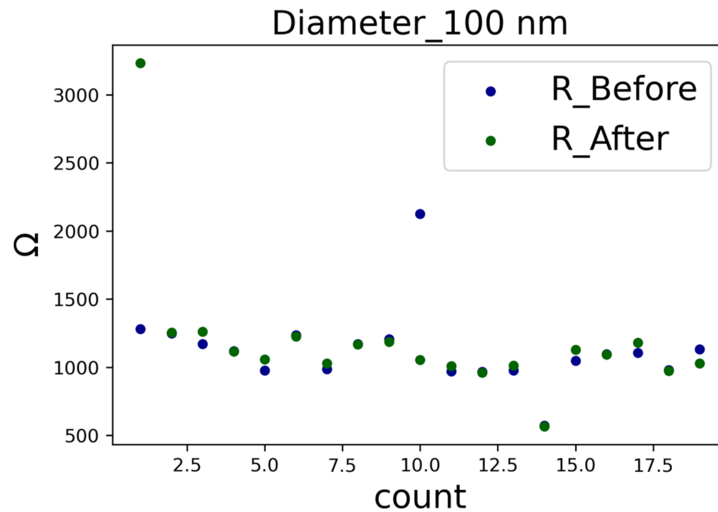

Figure 110: Scattering plot: STT-MTJ Resistance values before and after irradiation

Indeed, our data analysis shows how median value and standard deviation of resistance (Fig. 113 a and b) and TMR (Fig. 113 c and d) are immune to protons irradiation both for SOT and STT- MTJs. On the contrary, as Fig. 114 a and b show, the median value of H_c after irradiation is larger than before both for SOT and STT devices. However, to gain more insights, these data should be analyzed together with the H_{off} ones. Concerning SOT devices, the fact that H_{off} absolute value increased (Fig. 114d) means that, statistically, the majority of the hysteresis loop shifted towards the left. On the contrary, for the STT MTJs, the change of H_{off} sign, from negative to positive values (Fig. 114 c), implies that the P to AP transition now takes place at higher field for most of the devices.

.png .png

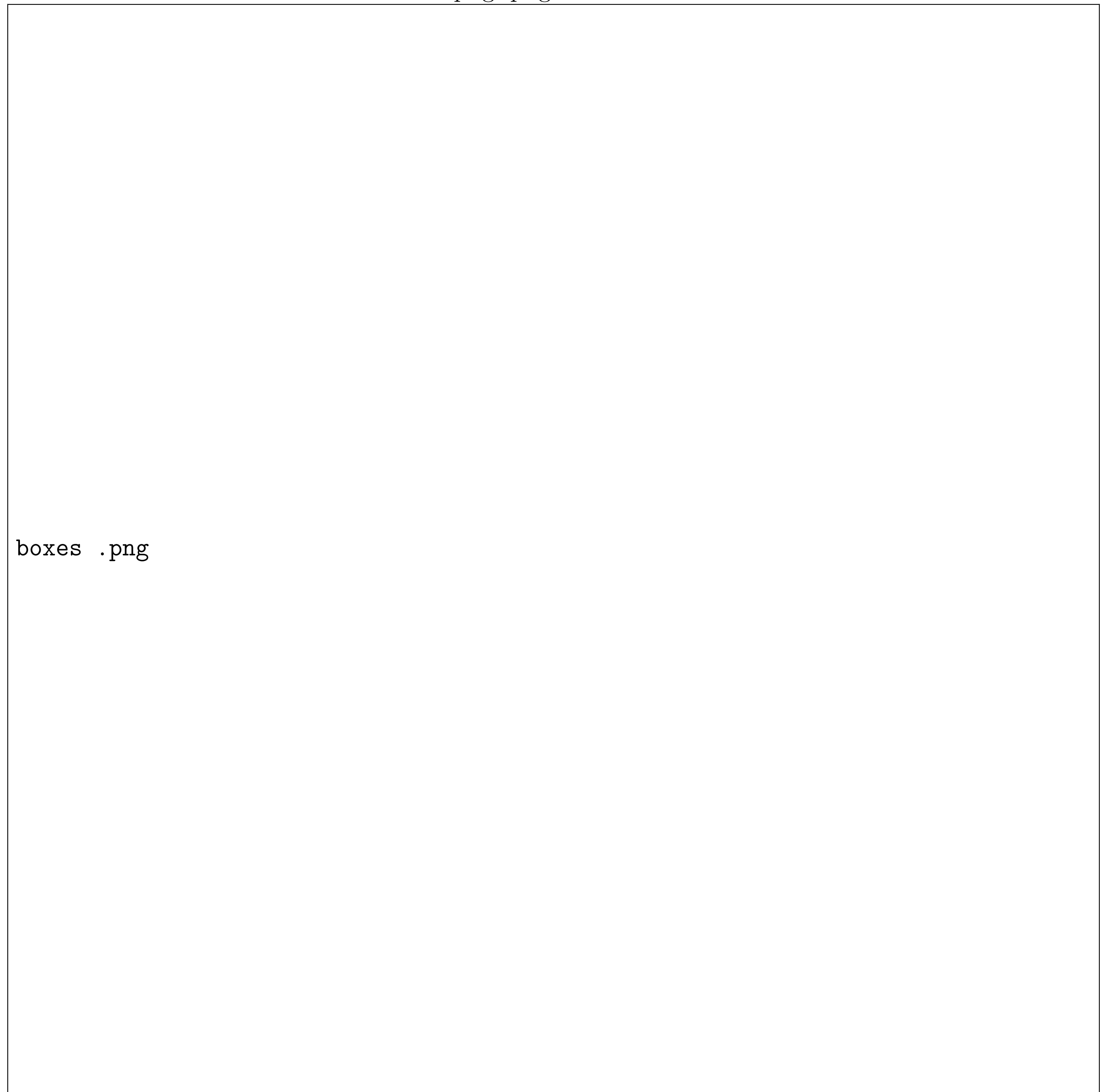

Figure 112: SOT MTJs Resistance variation before (a) and after (b) the irradiation at F2 for different sizes.

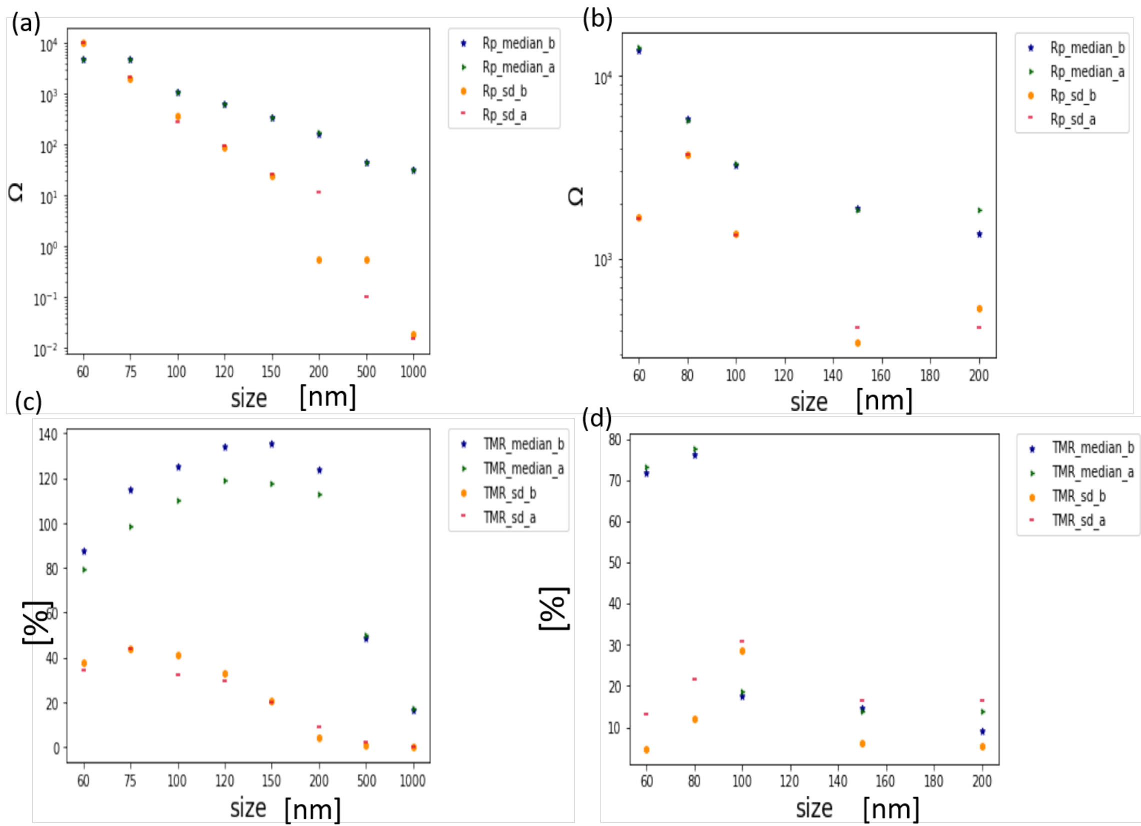

Figure 113: Resistance and TMR median and standard deviation before and after the F2 irradiation (a) and (c) STT devices, (b) and (d) SOT devices

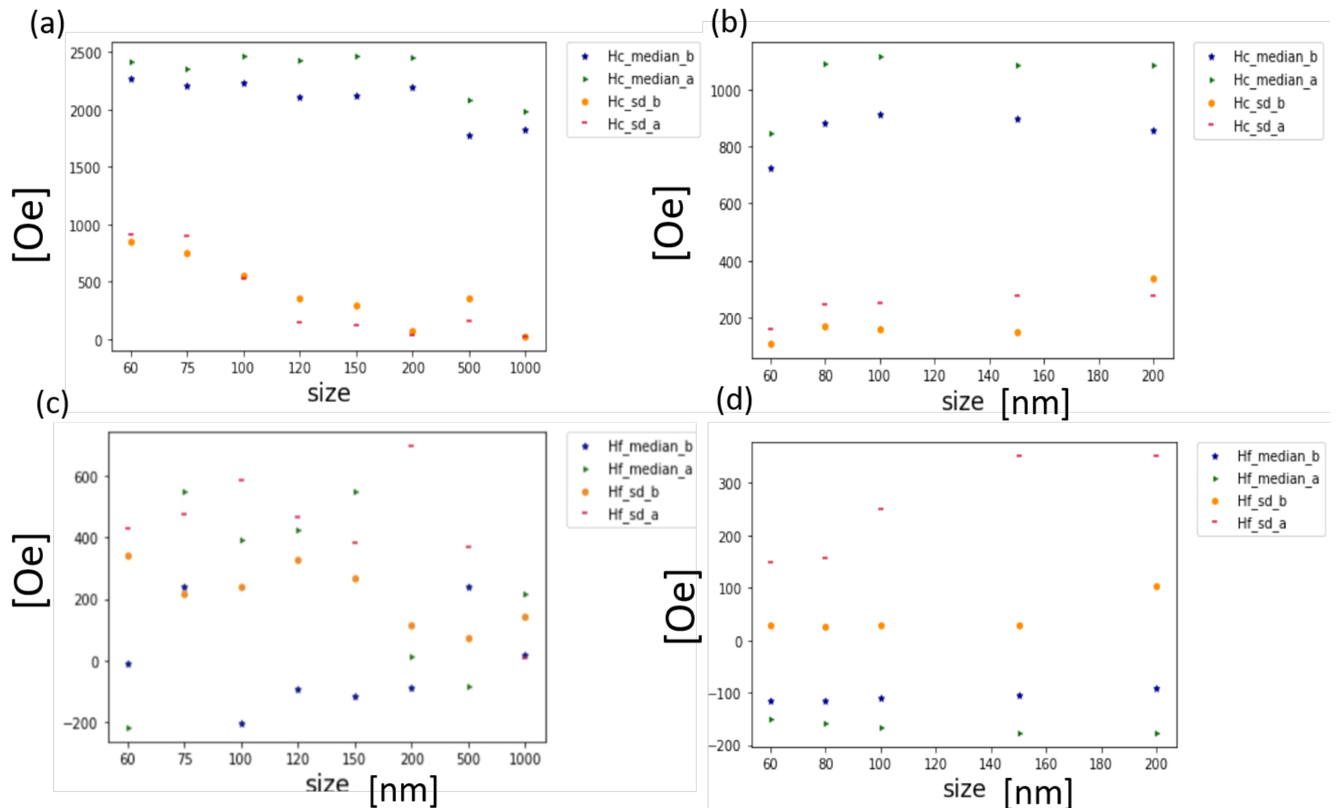

Figure 114: H_c and H_{off} median and standard deviation before and after the F2 irradiation (a) and (c) STT devices, (b) and (d) SOT devices

For the STT-MTJ devices we were also able to obtain indirect measures of other parameters such as the thermal stability factor (Δ) and anisotropy field (H_k). We show here the distribution for the smallest size and the 150 nm size for the latter (Fig. 115 and Fig. 116) and the former (Fig. 117 and Fig. 118) before (subscript "b") and after (subscript "a") the irradiation.

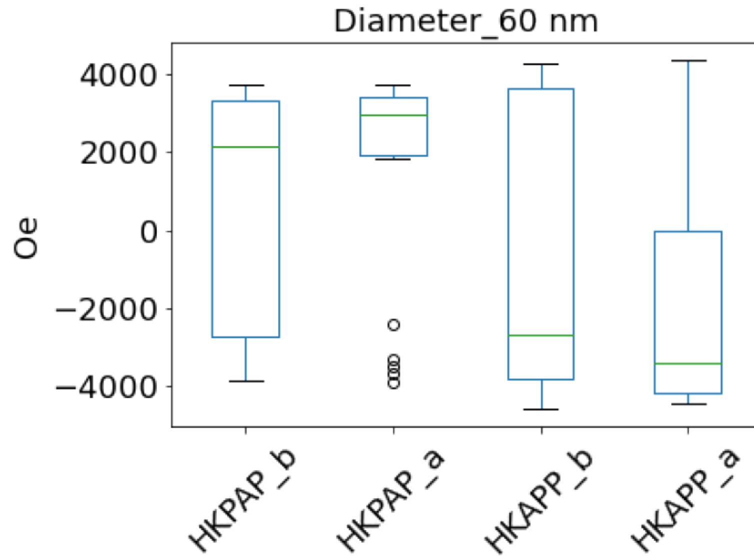

Figure 115: Anisotropy field variation in both sense of the transaction (P→ AP and AP→ P)

.

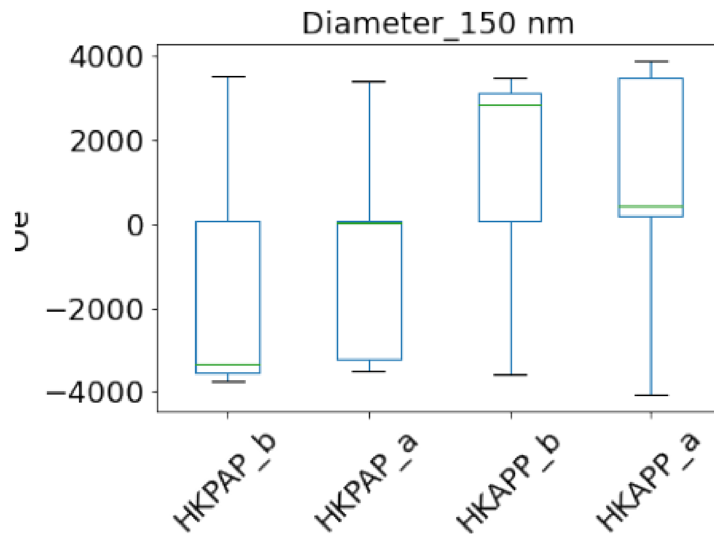

Figure 116: Anisotropy field variation in both sense of the transaction (P→ AP and AP→ P).

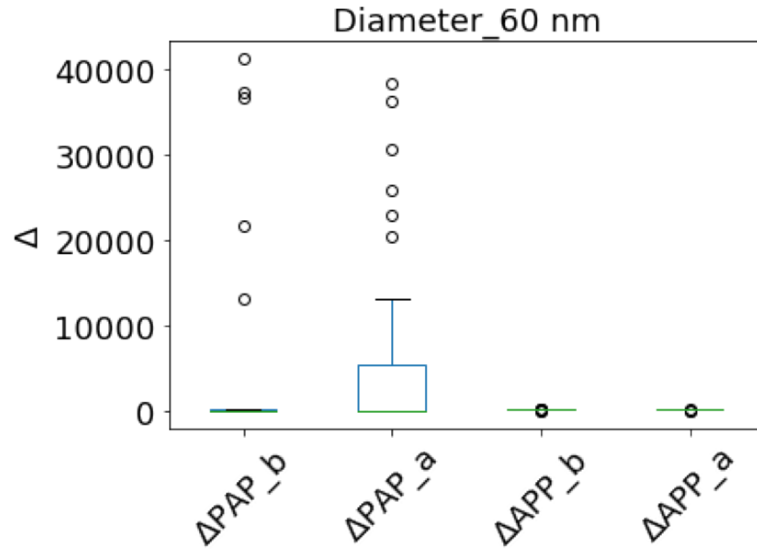

Figure 117: Thermal stability factor in both sense of the transaction (P→ AP and AP→ P).

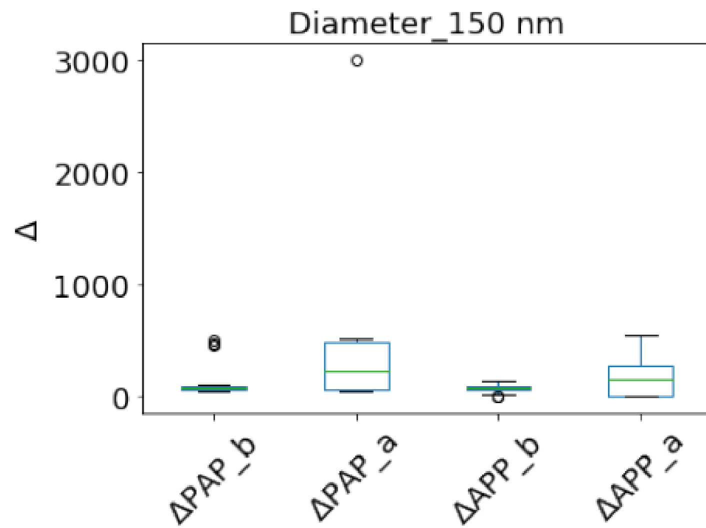

Figure 118: Thermal stability factor in both sense of the transaction (P→ AP and AP→ P).

It is difficult to draw some conclusion, but these data seemed to be in accordance with what we have just observed. Indeed after irradiation the average value of H_k in the AP to P transaction decreased, whereas the P to AP increased.

5.4 Machine Learning

In this section is proposed to use a basic Machine Learning technique to make prediction on the radiation effects over devices with exactly the same MTJ stack but which differ from the irradiated one for example from the size, any other parameters. First of all we plot

the main MTJ parameters before irradiation against the resistance value after irradiation to oversee if there is any clear relation between them. This is shown in Fig. 119 for the TMR, in Fig. 120 for the H_c, in Fig. 121 for the size and in Fig. 122 for the resistance.

For the sake of simplicity we focused on plots which show quite a linear relationship as it is the case of Fig. 122 which represents the resistance before and after irradiation. According to the best practice, we split the data we obtained from the irradiation into a training set and a test set to have a counterpart which indicates the accuracy of the built model. The latter has been built using the Sklearn library in Python coding language and by importing the linear regression model which has been trained on the proper part of data and then tested on the other.

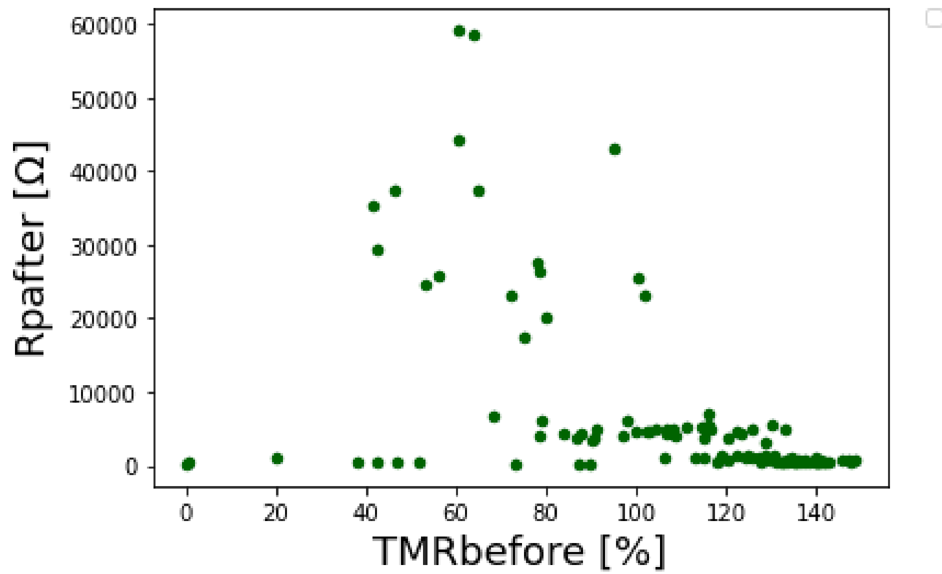

Figure 119: TMR values before irradiation versus resistance values after the irradiation.

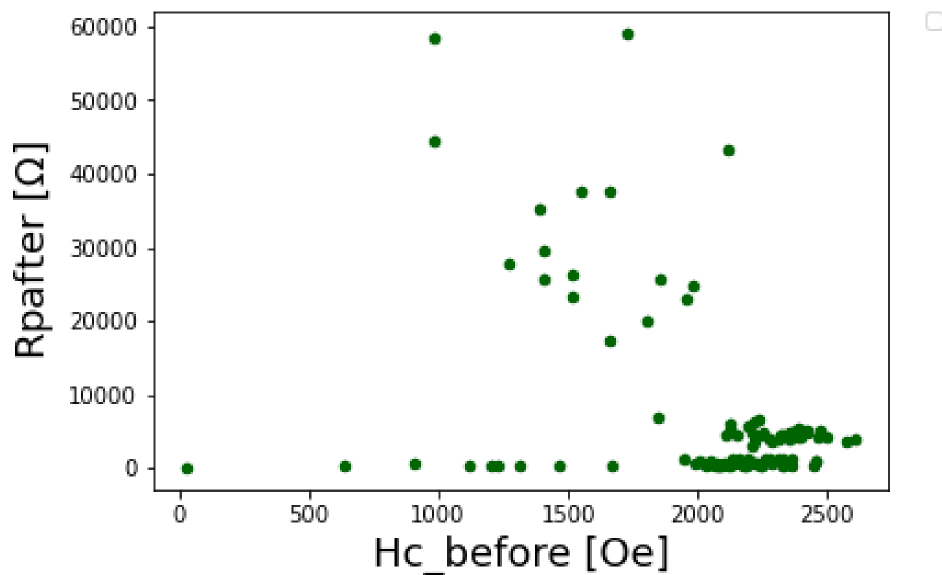

Figure 120: Coercive field values before irradiation versus resistance values after the irradiation.

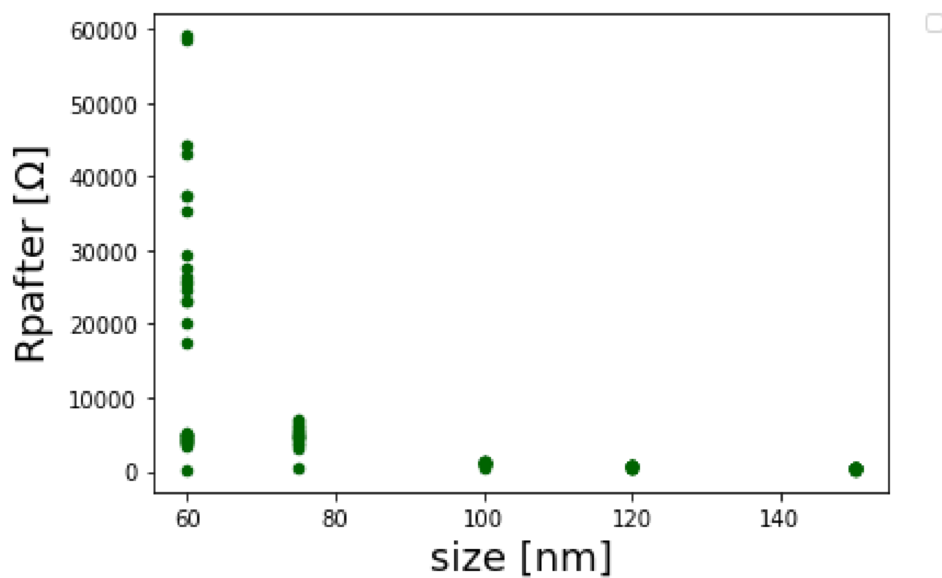

Figure 121: Size values versus resistance values after the irradiation.

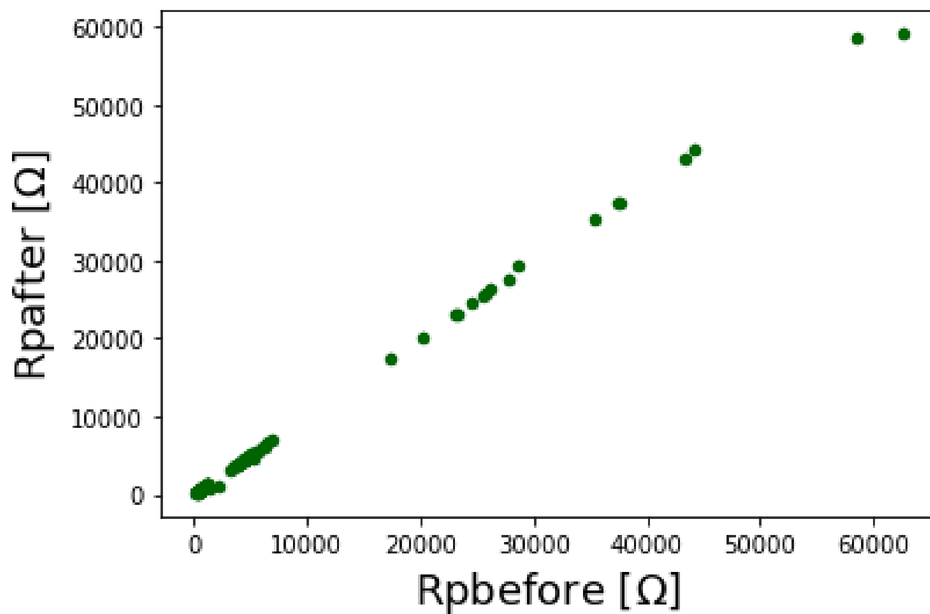

Figure 122: Resistance values after and before irradiation.

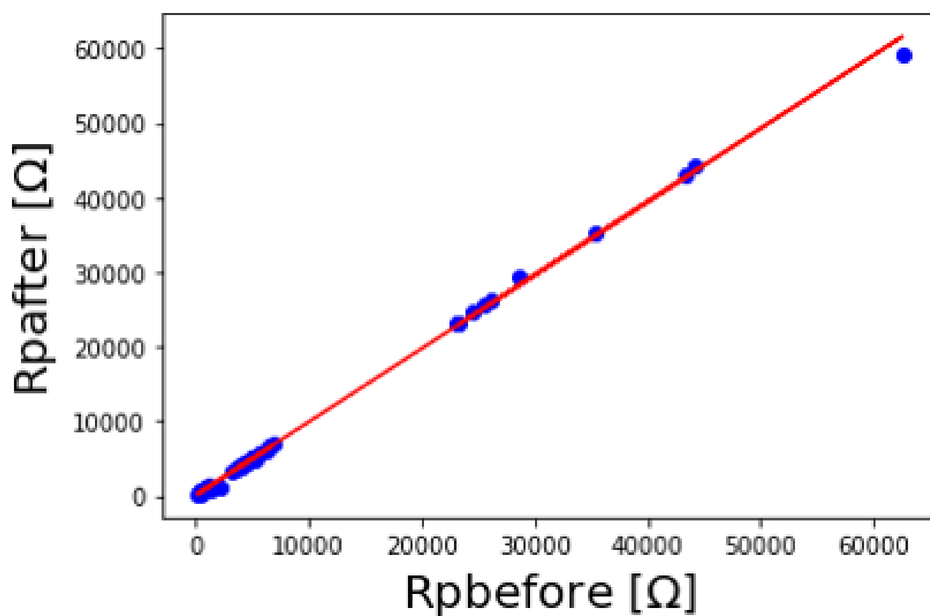

Figure 123: Read line represents the linear model prediction on the values obtained with sklearn regression model library in Python.

The corresponding calculated parameters which give the equation for the red line in Fig. 123 are:

$$R_{\text{pAfter}} = -12 + R_{\text{pBefore}} \tag{5.1}$$

An interesting evaluation will be to find a geometrical transformation of the plot by means of kernel and to see if a multi linear regression model could be build to predict the value of the resistance after in relation to all the other parameters.However this is well beyond

the scope of this section which aimed to open a direction of possible Machine Learning applications in the radiations test.

5.5 Conclusion

Proton irradiation of SOT devices seems to suggested that scaled devices are more sensitive to resistance changes. A comparative study on SOT and STT elementary structures demonstrates electrical properties to be unaffected up to the highest proton fluence used in this campaign, i.e. 1.2 x 10^{12} p/cm^2. Simultaneously, an increase of the coercive field is observed for both the categories of devices. The offset field variations are more noticeable for STT devices, where this parameter changes its sign, than for SOT MTJ. This could be explained as a consequence of the fact that the writing current in SOT devices does not flow into the MTJ, thence any structural changes in the MgO barrier or other layers will affect less the writing process. The latter consideration seems to suggest SOT devices as possible better candidate than STT ones for future space applications.

In the last section we suggested that ML technique could be applied to predict the value of the resistance after irradiation based on known parameters. We are aware that this could work only on exactly the same kind of devices but, taking into account the cost of the irradiation test, testing for example a large part of the devices and predict the behaviour of some other by means of ML could still be an interesting path to be explored. If the data-sets are large enough it could be also interesting to predict heavy ion irradiation response based on the proton ones and vice-versa.

Chapter 6

Conclusion and perspectives

This work aimed to investigate the irradiation response of spintronic devices exposed to radioactive space environment. To this aim, theoretical considerations have been merged with experimental results.

As a first step electrical simulations were used to understand the impact of the various STT and SOT parameters on their robustness to radiation. An hybrid SOT-STT model was proposed to take into account the possibility of switching due to a fault injection in the SOT reading path. These simulations suggest SOT devices to be more robust than STT but at the same time, SOT-CMOS hybrid circuit showed an increased number of sensitive nodes. Then we went on, and we study the possible basic degradation mechanisms that can trigger SEU in STT-MTJ, building a bridge between radiation effects and spintronic theory. We have proposed a sensitive volume definition for the MTJ that includes not only the MgO oxide barrier and both CoFeB layers, but the entire MTJ. Concerning the SEU triggering events in the CoFeB, two switching mechanisms have been identified: Spin-Transfer Torque and thermal activation. The use of thermal spike model compared with the LET data from TRADCARE® bought new insights on the failure mechanism due to particle strikes.

We then performed two experimental irradiation campaigns on purely magnetic spintronic devices: one with heavy ion and the other with proton. In this context, instead of operating in the usual way, i.e. simply programming the devices and reading them after the irradiation to oversee if errors occurred, we have shown that a complete write cycles is also important to determine if and how other important magnetic parameters experience a shift/ drift. This was the case for the coercive field and off set field after heavy ion irradiation. Thanks to the different sizes of devices we also tried to draw some trend on the impact of scaling (both MTJ sizes and the distance from one another), in particular in the light of thermal stability and secondary productions. This opens the door to an important future study perspective: the integration of peripheral circuit needed to read/write the MTJ. This could be translated in the open question: could the secondary particles produced during STT and SOT devices irradiation be a serious threat for CMOS circuitry? Our simulations showed the secondary production range be over 1 μm and their energy reach hundreds of eV. Moreover as in this work we suggested temperature to play an important role, future research directions should investigate different stack composition to enhance MTJ thermal stability especially as the dimensions scaled down.

Proton irradiation campaign was performed on purely magnetic STT and SOT devices, showing a general immunity of both devices. However, by comparing in details SOT and STT devices parameters, the first seemed to be less impact than the second. Further test campaigns on both devices type are planned in the next future: in particular the dynamic test which was impossible to perform due to the COVID-19 pandemic, could bring clearer insights on the parameters evolution during the irradiation. These tests could be performed with different type of irradiation, such as proton, heavy ion and gamma ray. Indeed, since in the real space environment all these particles are present in the same place the best choice will be a mixed radiation test environment. Finally, aware of the high costs of irradiation campaign, we have suggested Machine Learning techniques to be applied to the trained on the large data set of the experimental campaigns to predict the behaviour of similar devices without the need of testing all them in order to optimize costs.

Bibliography

[1] "2013 International Technology Roadmap for Semiconductors". In: (2015). URL: //www.semiconductors.org/resources/2015-international-technology-roadmap-for-semiconductors-itrs/.

[2] N. Adrianjohany et al. "TRADCARE: a multi-physics SEE prediction software using Geant4 toolkit". In: *14th Geant4 Space Users Workshop*. 2019.

[3] G. Prenat et al. "Ultra-Fast and High-Reliability SOT-MRAM: From Cache Replacement to Normally-Off Computing". In: *IEEE Transactions on Multi-Scale Computing Systems* 2.1 (2016), pp. 49–60. DOI: 10.1109/TMSCS.2015.2509963.

[4] I. M. Miron et al. "Perpendicular switching of a single ferromagnetic layer induced by in-plane current injection". In: *Nature* 476 (2011), pp. 189–193.

[5] K. Garello et al. "Spin-Orbit Torque MRAM for ultrafast embedded memories: from fundamentals to large scale technology integration". In: *2019 IEEE 11th International Memory Workshop (IMW)*. 2019, pp. 1–4. DOI: 10.1109/IMW.2019.8739466.

[6] M. Alamdar et al. "Irradiation Effects on Perpendicular Anisotropy Spin Orbit Torque Magnetic Tunnel Junctions". In: *IEEE Transactions on Nuclear Science* (2021). DOI: 10.1109/TNS.2021.3066070.

[7] Nomena Andrianjohany. "Méthodologie de prédiction multi-échelle pour l'évaluation et le durcissement des circuits intégrés complexes face aux événements singuliers d'origine radiative". In: 2018.

[8] D. Apalkov, B. Dieny, and J. M. Slaughter. "Magnetoresistive Random Access Memory". In: *Proceedings of the IEEE* 104.10 (2016), pp. 1796–1830.

[9] N.W. Ashcroft and N.D. Mermin. *Solid State Physics*. Philadelphia: Saunders College, 1976.

[10] H. Aziza et al. "ReRAM ON/OFF resistance ratio degradation due to line resistance combined with device variability in 28nm FDSOI technology". In: *2017 Joint International EUROSOI Workshop and International Conference on Ultimate Integration on Silicon (EUROSOI-ULIS)*. 2017, pp. 35–38. DOI: 10.1109/ULIS.2017.7962594.

[11] Hua BAI et al. "Experimental verification of SEU monitor with heavy ions". In: *2018 International Conference on Radiation Effects of Electronic Devices (ICREED)*. 2018, pp. 1–3. DOI: 10.1109/ICREED.2018.8905089.

[12] S. Bandiera et al. "Enhancement of Perpendicular Magnetic Anisotropy through reduction of Co/Pt interdiffusion in (Co/Pt) multilayers". In: *Applied Physics Letters* 100 (article no. 142410, Mar. 2012).

[13] H. J. Barnaby. "Total-Ionizing-Dose Effects in Modern CMOS Technologies". In: *IEEE Transactions on Nuclear Science* 53.6 (2006), pp. 3103–3121. DOI: 10.1109/TNS.2006.885952.

[14] Giovanni Betti Beneventi. "Characterization and modeling of phase-change memories". PhD thesis. Oct. 2011.

[15] Mark Brongersma, E. Snoeks, and A. Polman. "Temperature dependence of MeV heavy ion irradiation-induced viscous flow in SiO_2". In: *Applied Physics Letters* 71 (Sep. 1997), pp. 1628–1630.

[16] Geoffrey Burr et al. "Access devices for 3D crosspoint memory". In: *Journal of vacuum science technology. B, Microelectronics and nanometer structures: processing, measurement, and phenomena: an official journal of the American Vacuum Society* 32 (July 2014), p. 040802. DOI: 10.1116/1.4889999.

[17] W. Calienes et al. "Bulk and FDSOI SRAM resiliency to radiation effects". In: *2014 IEEE 57th International Midwest Symposium on Circuits and Systems (MWSCAS)*. 2014, pp. 655–658. DOI: 10.1109/MWSCAS.2014.6908500.

[18] Djaafar Chabi et al. "Design and Analysis of Radiation Hardened Sensing Circuits for Spin Transfer Torque Magnetic Memory and Logic". In: *IEEE Transactions on Nuclear Science* 61.6 (Dec. 2014), pp. 3258–3264. ISSN: 1558-1578. DOI: 10.1109/TNS.2014.2370735.

[19] Jyotirmoy Chatterjee et al. "Physicochemical origin of improvement of magnetic and transport properties of STT-MRAM cells using Tungsten on FeCoB storage layer". In: *Applied Physics Letters* 114 (article no. 092407, Mar. 2019). DOI: 10.1063/1.5081912.

[20] Antoine Chavent et al. "Effects of the Heating Current Polarity on the Writing of Thermally Assisted Switching-MRAM". In: *IEEE Transactions on Magnetics* 50.11 (2014), pp. 1–4. DOI: 10.1109/TMAG.2014.2322494.

[21] Murat Cubukcu et al. "Ultra-Fast Perpendicular Spin–Orbit Torque MRAM". In: *IEEE Transactions on Magnetics* 54.4 (2018), pp. 1–4. DOI: 10.1109/TMAG.2017.2772185.

[22] L. Cuchet et al. "Double Magnetic Tunnel Junctions with Perpendicular Anisotropy". In: *2015 IEEE International Magnetics Conference (INTERMAG)*. May 2015, pp. 571–572.

[23] S. L. Daraszewicz and D. M. Duffy. “Extending the inelastic thermal spike model for semiconductors and insulators”. In: *Nuclear Instruments and Methods in Physics Research B* 269.14 (July 2011), pp. 1646–1649. DOI: 10.1016/j.nimb.2010.11.031.

[24] S.L. Daraszewicz and D.M. Duffy. “Extending the inelastic thermal spike model for semiconductors and insulators”. In: *Nuclear Instruments and Methods in Physics Research Section B: Beam Interactions with Materials and Atoms* 269.14 (2011), pp. 1646 –1649. ISSN: 0168-583X. DOI: https://doi.org/10.1016/j.nimb.2010.11.031.

[25] A. Debelle et al. “Combined experimental and computational study of the recrystallization process induced by electronic interactions of swift heavy ions with silicon carbide crystals”. In: *Phys. Rev. B* 86 (10 articel no. 100102, Sep. 2012). DOI: 10.1103/PhysRevB.86.100102.

[26] Bernard Dieny, R.B. Goldfarb, and Kyung-Jin Lee. *Introduction to Magnetic Random-Access Memory*. Hoboken, Wiley-IEEE Press, USA, Nov. 2016, pp. 1–242. DOI: 10.1002/9781119079415.

[27] Bernard Dieny and I. Lucian Prejbeanu. “Magnetic Random-Access Memory”. In: *Introduction to Magnetic Random-Access Memory*. John Wiley & Sons, Ltd, 2016. Chap. 5, pp. 101–164. ISBN: 9781119079415. DOI: 10.1002/9781119079415.ch5. eprint: https://onlinelibrary.wiley.com/doi/pdf/10.1002/9781119079415.ch5. URL: https://onlinelibrary.wiley.com/doi/abs/10.1002/9781119079415.ch5.

[28] *Discovery could help lengthen lifespan of electronic devices*. https://www.sydney.edu.au/news-opinion/news/2021/04/08/discovery-could-help-lengthen-lifespan-of-electronic-devices.html.

[29] M. Durlam et al. “Toggle MRAM: A highly-reliable Non-Volatile Memory”. In: *2007 International Symposium on VLSI Technology, Systems and Applications (VLSI-TSA)*. 2007, pp. 1–2. DOI: 10.1109/VTSA.2007.378942.

[30] M. Fazeli et al. “Feedback Redundancy: A Power Efficient SEU-Tolerant Latch Design for Deep Sub-Micron Technologies”. In: *37th Annual IEEE/IFIP International Conference on Dependable Systems and Networks (DSN’07)*. 37th Annual IEEE/IFIP International Conference on Dependable Systems and Networks (DSN’07). ISSN: 2158-3927. June 2007, pp. 276–285. DOI: 10.1109/DSN.2007.51.

[31] A. Fernandez Fernandez et al. “High-Vacuum Gamma Irradiation Facilities for Synergistic Effects Testing on Optoelectronic Components and Materials”. In: *IEEE Transactions on Nuclear Science* 53.6 (2006), pp. 3726–3730. DOI: 10.1109/TNS.2006.884248.

[32] J. Ferré et al. "Irradiation induced effects on magnetic properties of Pt/Co/Pt ultrathin films". In: *Journal of Magnetism and Magnetic Materials* 198 (June 1999), pp. 191–193. DOI: 10.1016/S0304-8853(98)01084-1.

[33] D.M. Fleetwood, S.T. Pantelides, and Ronald Schrimpf. *Defects in microelectronic materials and devices*. Taylor and Francis Group LLC, Boca Raton, FL, USA Jul. 2009, pp. 1–755.

[34] Vladimir M Fridkin and Stephen Ducharme. "Ferroelectricity at the nanoscale". In: *Physics-Uspekhi* 57.6 (2014), p. 597.

[35] Alessandro Fumarola et al. "Bidirectional Non-Filamentary RRAM as an Analog Neuromorphic Synapse, Part II: Impact of Al/Mo/Pr0.7Ca0.3MnO3 Device Characteristics on Neural Network Training Accuracy". In: *IEEE Journal of the Electron Devices Society* 6 (2018), pp. 169–178. DOI: 10.1109/JEDS.2017.2782184.

[36] Manuel Le Gallo and Abu Sebastian. "An overview of phase-change memory device physics". In: *Journal of Physics D: Applied Physics* 53.21 (2020), p. 213002. DOI: 10.1088/1361-6463/ab7794. URL: https://doi.org/10.1088/1361-6463/ab7794.

[37] P. Gambardella and I. M. Miron. "Current-induced Spin–orbit torques". In: *Philosophical Transactions of the Royal Society A: Mathematical, Physical and Engineering Sciences* 369 (2011), pp. 3175 –3197.

[38] Chen Gang, Gao Bo, and Gong Min. "A dual redundancy radiation-hardened flip—flop based on a C-element in a 65 nm process". In: *Journal of Semiconductors* 34.9, 095012 (2013), p. 095012. DOI: 10.1088/1674-4926/34/9/095012.

[39] G. Gasiot et al. "SER/SEL performances of SRAMs in UTBB FDSOI28 and comparisons with PDSOI and BULK counterparts". In: *2014 IEEE International Reliability Physics Symposium*. 2014, SE.6.1–SE.6.5. DOI: 10.1109/IRPS.2014.6861178.

[40] T. Heijmen, D. Giot, and P. Roche. "Factors that impact the critical charge of memory elements". In: *12th IEEE International On-Line Testing Symposium (IOLTS'06)*. 12th IEEE International On-Line Testing Symposium (IOLTS'06). ISSN: 1942-9401. July 2006, pp. 57–62. DOI: 10.1109/IOLTS.2006.35.

[41] Kazuyuki Hirose et al. "Memory reliability of spintronic materials and devices for disaster-resilient computing against radiation-induced bit flips on the ground". In: *Japanese Journal of Applied Physics* 56 (article no. 0802A5, Aug. 2017). DOI: 10.7567/JJAP.56.0802A5.

[42] H. Honjo et al. "First demonstration of field-free SOT-MRAM with 0.35 ns write speed and 70 thermal stability under 400C thermal tolerance by canted SOT structure and its advanced patterning/SOT channel technology". In: *2019 IEEE International Electron Devices Meeting (IEDM)*. 2019, pp. 28.5.1–28.5.4. DOI: 10.1109/IEDM19573.2019.8993443.

[43] H. Honjo et al. "Origin of variation of shift field via annealing at 400C in a Perpendicular-Anisotropy Magnetic Tunnel Junction with [Co/Pt]-multilayers based synthetic ferrimagnetic reference layer". In: *AIP Advances* 7.5 (article no. 055913, May 2017). DOI: 10.1063/1.4973946.

[44] H. Honjo et al. "Origin of variation of shift field via annealing at 400C in a perpendicular-anisotropy Magnetic Tunnel Junction with [Co/Pt]-multilayers based synthetic ferrimagnetic reference layer". In: *AIP Advances* 7.5 (article no 055913, May 2017). DOI: 10.1063/1.4973946.

[45] Henning Huckfeldt et al. "Modification of the saturation magnetization of exchange bias thin film systems upon light-ion bombardment". In: *Journal of physics. Condensed matter : an Institute of Physics journal* 29.12 (article no. 125801, Mar. 2017), p. 125801. ISSN: 0953-8984. DOI: 10.1088/1361-648x/aa5ad5.

[46] H. Hughes et al. "Radiation Studies of Spin-Transfer Torque Materials and Devices". In: *IEEE Transactions on Nuclear Science* 59.6 (2012), pp. 3027–3033.

[47] Cheol Seong Hwang and Thomas Mikolajick. "11 - Ferroelectric memories". In: *Advances in Non-Volatile Memory and Storage Technology (Second Edition)*. Ed. by Blanka Magyari-Köpe and Yoshio Nishi. Second Edition. Woodhead Publishing Series in Electronic and Optical Materials. Woodhead Publishing, 2019, pp. 393–441. ISBN: 978-0-08-102584-0. DOI: https://doi.org/10.1016/B978-0-08-102584-0.00012-7. URL: https://www.sciencedirect.com/science/article/pii/B9780081025840000127.

[48] S Ikeda et al. "A Perpendicular-Anisotropy CoFeB–MgO Magnetic Tunnel Junction". In: *Nature materials* 9 (2010), pp. 721–4. DOI: 10.1038/nmat2804.

[49] J. D. Ingalls et al. "Total Dose and Heavy Ion Radiation Response of 55 nm Avalanche Technology Spin Transfer Torque MRAM". In: *2019 IEEE Radiation Effects Data Workshop*. 2019, pp. 190–193. DOI: 10.1109/REDW.2019.8906645.

[50] "Introduction to Magnetic Random-Access Memory by Bernard Dieny, Ronald B. Goldfarb, and Kyung-Jin Lee". In: *MRS Bulletin* 43.5 (2018), 389–389. DOI: 10.1557/mrs.2018.114.

[51] J. Iwata-Harms et al. "High-temperature thermal stability driven by magnetization dilution in CoFeB free layers for spin-transfer-torque magnetic random access memory". In: *Scientific Reports* 8 (article no 14409, Sep. 2018).

[52] K. Jabeur et al. "Comparison of Verilog-A compact modelling strategies for spintronic devices". In: *Electronics Letters* 50.19 (Sept. 2014), pp. 1353–1355. ISSN: 0013-5194. DOI: 10.1049/el.2014.1083.

[53] Kotb Jabeur et al. "Compact Modeling of a Magnetic Tunnel Junction Based on Spin Orbit Torque". In: *IEEE Transactions on Magnetics* 50 (2014), pp. 1–8.

[54] Huang Jiancheng et al. "Effect of the stray field profile on the switching characteristics of the free layer in a perpendicular Magnetic Tunnel Junction". In: *Journal of Applied Physics* 117 (article no. 17B721, May 2015). DOI: 10.1063/1.4916037.

[55] Huang Jiancheng et al. "Effect of the stray field profile on the switching characteristics of the free layer in a perpendicular Magnetic Tunnel Junctions". In: (article no 17B721, May 2015).

[56] N Julai, A Yakovlev, and A Bystrov. "Error detection and correction of single event upset (SEU) tolerant latch". In: *2012 IEEE 18th International On-Line Testing Symposium (IOLTS)*. 2012 IEEE 18th International On-Line Testing Symposium (IOLTS). ISSN: 1942-9401. June 2012, pp. 1–6. DOI: 10.1109/IOLTS.2012.6313832.

[57] Norhuzaimin Julai, Lakshmanan Gurusamy, and Shamsiah Suhaili. "The Impact of Soft Error On C-Element with Different Technology". In: *Journal of Telecommunication, Electronic and Computer Engineering (JTEC)* 9.3 (Dec. 7, 2017), pp. 79–83. ISSN: 2289-8131. URL: http://journal.utem.edu.my/index.php/jtec/article/view/3158 (visited on 01/22/2020).

[58] Wang Kang et al. "A radiation hardened hybrid Spintronic/CMOS nonvolatile unit using magnetic tunnel junctions". In: *Journal of Physics D: Applied Physics* 47.40 (Sept. 2014), p. 405003. ISSN: 0022-3727. DOI: 10.1088/0022-3727/47/40/405003. URL: https://doi.org/10.1088%2F0022-3727%2F47%2F40%2F405003 (visited on 01/22/2020).

[59] I. Karpov et al. "Phase change memory parameters: Effects of atomic transformations". In: *2008 9th Annual Non-Volatile Memory Technology Symposium (NVMTS)*. 2008, pp. 1–5. DOI: 10.1109/NVMT.2008.4731187.

[60] R. Katti et al. "Heavy Ion Bit Response and Analysis of 256 Megabit Non-Volatile Spin-Torque-Transfer Magnetoresistive Random Access Memory (STT-MRAM)". In: *2018 Radiation Effects Data Workshop*. Jul. 2018, pp. 321–324. DOI: 10.1109/NSREC.2018.8584321.

[61] R. R. Katti. "Radiation-Induced Errors at Elevated Linear Energy Transfer Levels and Magnetic Error Rate Interactions in Magnetic Tunnel Junctions". In: *2019 IEEE Radiation Effects Data Workshop*. Jul. 2019, pp. 184–189.

[62] D. Kobayashi et al. “Influence of Heavy Ion Irradiation on Perpendicular-Anisotropy CoFeB-MgO Magnetic Tunnel Junctions”. In: *IEEE Transactions on Nuclear Science* 61.4 (Oct. 2014), pp. 1710–1716.

[63] D. Kobayashi et al. “Influence of heavy ion irradiation on perpendicular-anisotropy CoFeB-MgO magnetic tunnel junctions”. In: *2013 14th European Conference on Radiation and Its Effects on Components and Systems (RADECS)*. 2013, pp. 227–231. DOI: 10.1109/RADECS.2013.6937425.

[64] D. Kobayashi et al. “Soft errors in 10-nm-scale Magnetic Tunnel Junctions”. In: *Japanese Journal of Applied Physics* 56 (article no 0802B4, Jun. 2017).

[65] Daisuke Kobayashi et al. “Soft errors in 10-nm-scale Magnetic Tunnel Junctions exposed to high-energy heavy-ion radiation”. In: *Japanese Journal of Applied Physics* 56.8 (article no. 0802B4, Aug. 2017). DOI: 10.7567/JJAP.56.0802B4.

[66] A.Yu. Konobeyev et al. “Evaluation of effective threshold displacement energies and other data required for the calculation of advanced atomic displacement cross-sections”. In: *Nuclear Energy and Technology* 3.3 (Sept. 2017), 169–175. ISSN: 2452-3038. DOI: 10.1016/j.nucet.2017.08.007.

[67] H. Kronmüller, K.-D. Durst, and M. Sagawa. “Analysis of the magnetic hardening mechanism in RE-FeB permanent magnets”. In: *Journal of Magnetism and Magnetic Materials* 74.3 (Oct. 1988), pp. 291 –302. ISSN: 0304-8853. DOI: https://doi.org/10.1016/0304-8853(88)90202-8.

[68] Yahya Lakys et al. “Hardening Techniques for MRAM-Based Nonvolatile Latches and Logic”. In: *IEEE Transactions on Nuclear Science* 59.4 (Aug. 2012), pp. 1136–1141. ISSN: 1558-1578. DOI: 10.1109/TNS.2012.2195677.

[69] R. K. Lawrence and A. T. Kelly. “Single Event Effect Induced Multiple-Cell Upsets in a Commercial 90 nm CMOS Digital Technology”. In: *IEEE Transactions on Nuclear Science* 55.6 (2008), pp. 3367–3374. ISSN: 1558-1578. DOI: 10.1109/TNS.2008.2005981.

[70] Kyoung-Min Lee et al. “Temperature dependence of the interfacial magnetic anisotropy in W/CoFeB/MgO”. In: *AIP Advances* 7 (article no. 065107, Jun. 2017). DOI: 10.1063/1.4985720.

[71] Seung Eun Lee, Tae Hun Shim, and Jea Gun Park. “Perpendicular Magnetic Tunnel Junction (p-MTJ) spin-valves designed with a top $Co_2Fe_6B_2$ free layer and a nanoscale-thick Tungsten bridging and capping layer”. English. In: *NPG Asia Materials* 8.11 (article no. e324, Nov. 2016). ISSN: 1884-4049. DOI: 10.1038/am.2016.162.

[72] Seung-Eun Lee, Yasutaka Takemura, and Jea-Gun Park. "Effect of double MgO Tunneling Barrier on thermal stability and TMR ratio for perpendicular MTJ Spin-Valve with Tungsten layers". In: *Applied Physics Letters* 109 (article no.182405, Oct. 2016). DOI: 10.1063/1.4967172.

[73] S. Lequeux et al. "Thermal robustness of magnetic tunnel junctions with perpendicular shape anisotropy". In: *Nanoscale* 12 (11 2020), pp. 6378–6384. DOI: 10.1039/C9NR10366J. URL: http://dx.doi.org/10.1039/C9NR10366J.

[74] Steven Lequeux et al. "Thermal robustness of Magnetic Tunnel Junctions". In: (Feb. 2020), pp. 6378–6384.

[75] Luqiao et al. Liu. "Spin-Torque Switching with the Giant Spin Hall Effect of Tantalum". In: *Science (New York, N.Y.)* 336 (May 2012), pp. 555–8. DOI: 10.1126/science.1218197.

[76] R. Liu et al. "Single Event Transient and TID Study in 28 nm UTBB FDSOI Technology". In: *IEEE Transactions on Nuclear Science* 64.1 (2017), pp. 113–118. ISSN: 1558-1578. DOI: 10.1109/TNS.2016.2627015.

[77] Nicolas Locatelli and Vincent Cros. "Basic Spintronic Transport Phenomena". In: *Introduction to Magnetic Random-Access Memory*. John Wiley & Sons, Ltd, 2016. Chap. 1, pp. 1–28. ISBN: 9781119079415. DOI: 10.1002/9781119079415.ch1. eprint: https://onlinelibrary.wiley.com/doi/pdf/10.1002/9781119079415.ch1. URL: https://onlinelibrary.wiley.com/doi/abs/10.1002/9781119079415.ch1.

[78] Nicolas Locatelli, Liza Herrera Diez, and Thomas Mikolajick. "Chapter 4 - Magnetic and ferroelectric memories". In: *Memristive Devices for Brain-Inspired Computing*. Ed. by Sabina Spiga et al. Woodhead Publishing Series in Electronic and Optical Materials. Woodhead Publishing, 2020, pp. 97–134. ISBN: 978-0-08-102782-0. DOI: https://doi.org/10.1016/B978-0-08-102782-0.00004-6. URL: https://www.sciencedirect.com/science/article/pii/B9780081027820000046.

[79] Jeremy Lopes et al. "An SEU tolerant MRAM based non-volatile asynchronous circuit design". In: *2016 16th European Conference on Radiation and Its Effects on Components and Systems (RADECS)*. 2016 16th European Conference on Radiation and Its Effects on Components and Systems (RADECS). Sept. 2016, pp. 257–260. DOI: 10.1109/RADECS.2016.8093151.

[80] Jiwei Lu et al. "Radiation effects on the magnetism and the spin dependent transport in magnetic materials and nanostructures for spintronic applications". In: *Journal of Materials Research* 30.9 (Feb. 2015), 1430–1439. DOI: 10.1557/jmr.2014.413.

[81] R. et al. M. “Shared-Write-Channel-Based Device for High-Density Spin-Orbit-Torque Magnetic Random-Access Memory”. In: 15 (2 2021), p. 024063.

[82] “Magneto Resistive RAM (MRAM) Market Analysis By Type (Toggle, Spin-Transfer Torque), By Application (Consumer Electronics, Robotics, Automotive, Enterprise Storage, Aerospace), By Region, And Segment Forecasts, 2018 - 2025”. In: (Apr. 2017). URL: `https://www.grandviewresearch.com/industry-analysis/magneto-resistive-ram-random-access-memory-mram-market`.

[83] Sara Majetich, Tianlong Wen, and Olin Mefford. “Magnetic Nanoparticles”. In: *MRS bulletin / Materials Research Society* 38 (Nov. 2013), pp. 899–903. DOI: `10.1557/mrs.2013.230`.

[84] Mark Mark. “Basic Spintronic Transport Phenomena”. In: *Magnetoelectronics*. Elsevier, 2004. ISBN: 9781119079415.

[85] LW Massengill. “SEU modeling and prediction techniques”. In: *IEEE NSREC Short Course*. Vol. 3. 1993, pp. 1–93.

[86] Rie Matsumoto et al. “Quantitative Analysis of Coherent and Incoherent Tunneling Currents in MgO-Based Epitaxial Magnetic Tunnel Junctions”. In: *Japanese Journal of Applied Physics* 50.6 (article no 063003, Jun. 2011). DOI: `10.1143/jjap.50.063003`.

[87] F B McLean and T R Oldham. “Basic mechanisms of radiation effects in electronic materials and devices. Final report, September 1986-September 1987”. In: (). URL: `https://www.osti.gov/biblio/5646360`.

[88] N.K. Minor and T. Klemmer. “Magnetic and structural properties of FeCoB thin films”. In: *IEEE Transactions on Magnetics* 37 (Aug. 2001), pp. 2302 –2304. DOI: `10.1109/20.951154`.

[89] Y. Monnet, M. Renaudin, and R. Leveugle. “Hardening techniques against transient faults for asynchronous circuits”. In: *11th IEEE International On-Line Testing Symposium*. 2005, pp. 129–134. DOI: `10.1109/IOLTS.2005.30`.

[90] Gordon E. Moore. “Cramming more components onto integrated circuits”. In: *Electronics* 38.8 (1965).

[91] David E. Muller. “Theory of asynchronous circuits”. In: Urbana, Illinois: University of Illinois, Graduate College, Digital Computer Laboratory, 1955.

[92] Riccardo Musenich et al. “The Limits of Space Radiation Magnetic Shielding: An Updated Analysis”. In: *IEEE Transactions on Applied Superconductivity* 28.3 (2018), pp. 1–5. DOI: `10.1109/TASC.2017.2785805`.

[93] K. Nishioka et al. "Novel Quad interface MTJ technology and its first demonstration with high thermal stability and switching efficiency for STT-MRAM beyond 2Xnm". In: *2019 Symposium on VLSI Technology*. Jul. 2019, T120–T121.

[94] *Numem to supply its STT-MRAM to a NASA AI core project*. https://www.mram-info.com/numem-supply-its-low-density-stt-mram-nasa-ai-core-project.

[95] C. Park et al. "Temperature Dependence of Critical Device Parameters in 1 Gb Perpendicular Magnetic Tunnel Junction Arrays for STT-MRAM". In: *IEEE Transactions on Magnetics* 53.2 (article no. 3400104, Feb. 2017). DOI: 10.1109/TMAG.2016.2615816.

[96] June-Young Park et al. "Effects of proton and ion beam radiation on magnetic tunnel junctions". In: *Thin Solid Films* (article no 137432, Sep. 2019).

[97] Min Hyuk Park et al. "Ferroelectricity and Antiferroelectricity of Doped Thin HfO2-Based Films". In: *Advanced Materials* 27.11 (2015), pp. 1811–1831. DOI: https://doi.org/10.1002/adma.201404531. eprint: https://onlinelibrary.wiley.com/doi/pdf/10.1002/adma.201404531. URL: https://onlinelibrary.wiley.com/doi/abs/10.1002/adma.201404531.

[98] Nicolas Perrissin et al. "A highly thermally stable sub-20 nm Magnetic Random-Access Memory based on perpendicular shape anisotropy". In: *Nanoscale* 10.25 (article no 12187, May 2018). DOI: 10.1039/C8NR01365A.

[99] Pierre Pourrouquet et al. "FASTRAD 3.2: Radiation Shielding Tool with a New Monte Carlo Module". In: *2011 IEEE Radiation Effects Data Workshop*. 2011.

[100] Ioan Prejbeanu et al. "Thermally assisted MRAM". In: *Journal of Physics Condensed Matter* 20 (Apr. 2007). DOI: 10.1088/0953-8984/19/16/165218.

[101] Eline Raymenants et al. "Chain of Magnetic Tunnel Junctions as a Spintronic Memristor". In: *Journal of Applied Physics* 124 (article no. 152116, Oct. 2018). DOI: 10.1063/1.5042431.

[102] P. Roche et al. "Determination of key parameters for SEU occurrence using 3-D full cell SRAM simulations". In: *IEEE Transactions on Nuclear Science* 46.6 (1999), pp. 1354–1362. ISSN: 1558-1578. DOI: 10.1109/23.819093.

[103] S. Sakhare et al. "Enablement of STT-MRAM as last level cache for the high performance computing domain at the 5nm node". In: *2018 IEEE International Electron Devices Meeting (IEDM)*. 2018, pp. 18.3.1–18.3.4. DOI: 10.1109/IEDM.2018.8614637.

[104] L. Schnitzspan et al. “Impact of Annealing Temperature on Tunneling Magnetoresistance Multilayer Stacks”. In: *IEEE Magnetics Letters* 11 (article no 4503705, Jun. 2020). DOI: 10.1109/LMAG.2020.3005381.

[105] J. R. Schwank, M. R. Shaneyfelt, and P. E. Dodd. “Radiation Hardness Assurance Testing of Microelectronic Devices and Integrated Circuits: Radiation Environments, Physical Mechanisms, and Foundations for Hardness Assurance”. In: *IEEE Transactions on Nuclear Science* 60.3 (2013), pp. 2074–2100. ISSN: 1558-1578. DOI: 10.1109/TNS.2013.2254722.

[106] N. Seifert. “Soft Error Rates of Hardened Sequentials utilizing Local Redundancy”. In: *2008 14th IEEE International On-Line Testing Symposium*. 2008, pp. 49–50. DOI: 10.1109/IOLTS.2008.61.

[107] N. Seifert et al. “On the radiation-induced soft error performance of hardened sequential elements in advanced bulk CMOS technologies”. In: *2010 IEEE International Reliability Physics Symposium*. 2010, pp. 188–197. DOI: 10.1109/IRPS.2010.5488831.

[108] Lembit Sihver et al. “Simulations of the MTR-R and MTR experiments at ISS, and shielding properties using PHITS”. In: Apr. 2009, pp. 1 –8. DOI: 10.1109/AERO.2009.4839360.

[109] M. M. C. Souza et al. “Metallic Mg insertion in rf deposited MgO barrier”. In: *Journal of Applied Physics* 107.9 (Apr. 20, 2010), p. 09C702. ISSN: 0021-8979. DOI: 10.1063/1.3355995. URL: https://aip.scitation.org/doi/full/10.1063/1.3355995 (visited on 01/22/2020).

[110] G.R. Srinivasan, P.C. Murley, and H.K. Tang. “Accurate, predictive modeling of soft error rate due to cosmic rays and chip alpha radiation”. In: *Proceedings of 1994 IEEE International Reliability Physics Symposium*. Proceedings of 1994 IEEE International Reliability Physics Symposium. Apr. 1994, pp. 12–16. DOI: 10.1109/RELPHY.1994.307864.

[111] J.R. Srour, C.J. Marshall, and P.W. Marshall. “Review of displacement damage effects in silicon devices”. In: *IEEE Transactions on Nuclear Science* 50.3 (2003), pp. 653–670. DOI: 10.1109/TNS.2003.813197.

[112] Roger E. Stoller et al. “On the Use of SRIM for Computing Radiation Damage Exposure”. In: *Nuclear Instruments and Methods in Physics Research. Section B, Beam Interactions with Materials and Atoms* (). ISSN: 0168-583X. DOI: 10.1016/j.nimb.2013.05.008. URL: https://www.osti.gov/biblio/1132718.

[113] D. Suess et al. “Calculation of coercivity of magnetic nanostructures at finite temperatures”. In: *Physical Review B* 84 (article no 224421, Dec. 2011). DOI: 10.1103/PhysRevB.84.224421.

[114] I. Sveklo et al. “Modification of Magnetic Properties of Pt/Co/Pt Films by Ga + Ion Irradiation: Focused versus Uniform Irradiation”. In: *Acta Physica Polonica A* 133 (May, 2018), pp. 1215–1226. DOI: 10.12693/APhysPolA.133.1215.

[115] G. Szenes. “Ion-velocity-dependent track formation in yttrium iron garnet: A thermal-spike analysis”. In: *Phys. Rev. B* 52 (9 1995), pp. 6154–6157. DOI: 10.1103/PhysRevB.52.6154.

[116] Saied Tehrani. “Status and Outlook of MRAM Memory Technology (Invited)”. In: *2006 International Electron Devices Meeting*. 2006, pp. 1–4. DOI: 10.1109/IEDM.2006.346850.

[117] B. M. S. Teixeira et al. “Stabilization of the easy-cone magnetic state in free layers of Magnetic Tunnel Junctions”. In: *Phys. Rev. B* 100 (18 article no 184405, Nov. 2019). DOI: 10.1103/PhysRevB.100.184405.

[118] Bruno Teixeira et al. “Ar + ion irradiation of magnetic tunnel junction multilayers: impact on the magnetic and electrical properties”. In: *Journal of Physics D: Applied Physics* (article no. 455003, Jul. 2020). DOI: 10.1088/1361-6463/aba38c.

[119] M. Toulemonde et al. “Atomic and cluster ion bombardment in the electronic stopping power regime: A thermal spike description”. In: *Nuclear Instruments and Methods in Physics Research Section B: Beam Interactions with Materials and Atoms* 112.1 (1996), pp. 26 –29. ISSN: 0168-583X. DOI: https://doi.org/10.1016/0168-583X(95)01129-3.

[120] Simon Van Beek et al. “Thermal stability analysis and modelling of advanced perpendicular Magnetic Tunnel Junctions”. In: *AIP Advances* 8 (article no. 055909, May 2018). DOI: 10.1063/1.5007690.

[121] Bi Wang et al. “Radiation impact of swift heavy ion beams on double-interface CoFeB/MgO Magnetic Tunnel Junctions”. In: *Applied Physics Letters* 116 (article no. 172401 Apr. 2020). DOI: 10.1063/1.5145124.

[122] D. Wright and M. Kelsey. “The Geant4 Bertini Cascade”. In: *Nuclear Instruments and Methods in Physics Research Section A Accelerators Spectrometers Detectors and Associated Equipment* 804 (2015), pp. 175–188. DOI: 10.1016/j.nima.2015.09.058.

[123] M. A. Xapsos, P. M. O’Neill, and T. P. O’Brien. “Near-Earth Space Radiation Models”. In: *IEEE Transactions on Nuclear Science* 60.3 (2013), pp. 1691–1705. ISSN: 1558-1578. DOI: 10.1109/TNS.2012.2225846.

[124] Tech. Rep. Yole Development. “Emerging Non-Volatile Memory”. In: (2018). URL: http://www.yole.fr/Emerging_NVM_Memory_Activities_Webcasts.aspx#.XMbGzzAzapo.

[125] T. Yoshida, K. Kobayashi, and J. Furuta. “Total Ionizing Dose Effects by alpha irradiation on circuit performance and SEU tolerance in thin BOX FDSOI process”. In: *2019 IEEE 25th International Symposium on On-Line Testing and Robust System Design (IOLTS)*. 2019, pp. 236–238. DOI: 10.1109/IOLTS.2019.8854439.

[126] Z. M. Zeng et al. “Effect of resistance-area product on spin-transfer switching in MgO-based magnetic tunnel junction memory cells”. In: *Applied Physics Letters* 98.7 (Feb. 14, 2011), p. 072512. ISSN: 0003-6951. DOI: 10.1063/1.3556615. URL: https://aip.scitation.org/doi/10.1063/1.3556615 (visited on 01/22/2020).

[127] Deming Zhang et al. “A novel SEU-tolerant MRAM latch circuit based on C-element”. In: *2014 12th IEEE International Conference on Solid-State and Integrated Circuit Technology (ICSICT)*. 2014 12th IEEE International Conference on Solid-State and Integrated Circuit Technology (ICSICT). Oct. 2014, pp. 852–854. DOI: 10.1109/ICSICT.2014.7021415.

[128] Yue Zhang et al. “Compact Modeling of Perpendicular-Anisotropy CoFeB/MgO Magnetic Tunnel Junctions”. In: *IEEE Transactions on Electron Devices* 59.3 (Mar. 2012), pp. 819–826. ISSN: 1557-9646. DOI: 10.1109/TED.2011.2178416.

[129] G. P. Zhao et al. “Nucleation or pinning: Dominant coercivity mechanism in exchange-coupled permanent/composite magnets”. In: *Computational Materials Science* 44 (Nov. 2008), pp. 122–126.

[130] L. Zhu et al. “Spin-Orbit Torque Induced Magnetization Switching In Co/Pt Multilayer-based Synthetic Antiferromagnets.” In: *2018 IEEE International Magnetics Conference (INTERMAG)*. 2018, pp. 1–1. DOI: 10.1109/INTMAG.2018.8508775.

Appendix A

Publications

Journal papers:

- **Odilia Coi** et al. "Spin-Transfer Torque Magnetic Tunnel Junction for Single Event Effects mitigation in IC design", *Transactions on Nuclear Science*, vol. 67, no. 7, pp. 1674-1681, July 2020, doi: 10.1109/TNS.2020.3002649.
- **Odilia Coi** et al. "Heavy ion Irradiation effects on advanced Perpendicular Anisotropy Spin-Transfer Torque Magnetic Tunnel Junction", *Transactions on Nuclear Science* vol. 68, no. 5, pp. 588-596, May 2021, doi: 10.1109/TNS.2021.3071257
- **Odilia Coi** et al. "SEU Mechanisms In Spintronic Devices: Critical Parameters and Basic Effects", Radiations and its effects on Components and Systems,*Transactions on Nuclear Science* available on IEEEXplore early access 10.1109/TNS.2021.3080080.

Conferences with proceedings:

- **Odilia Coi** et al."Proton irradiation effects on Spin Orbit-Torque and Spin Transfer-Torque Magnetic Tunnel Junctions", Radiations and its effects on Components and Systems (RADECS 2021), 13-17 September 2021, Vienna, Austria.
- **Odilia Coi** et al. "Laser and Heavy ion Irradiation effects on advanced Perpendicular Anisotropy Spin-Transfer Torque Magnetic Tunnel Junction", Nuclear & Space Radiation Effects Conference (NSREC 2020), Virtual Conference, December 2020.
- **Odilia Coi** et al. "SEU Mechanisms In Spintronic Devices: Critical Parameters and Basic Effects", Radiations and its effects on Components and Systems (RADECS 2020), Virtual Conference, October 2020.
- **Odilia Coi** et al. "Self Robust Non-Volatile C- element for single Event Upset enhanced tolerance", Radiations and its effects on Components and Systems (RADECS 2019), Montpellier, France 16-20 September 2019.
- **Odilia Coi** et al. "Exploring the Potential of Magnetic Tunnel Junction in Radiation Hardening circuit design", Grenoble NewSpace Week, (GNSW 2019), Grenoble, France, 14-17 May 2019, p.94.

- **Odilia Coi** et al. "A novel SRAM- STT-MRAM hybrid cache implementation improving cache performance", International Symposium on Nanoscale Architectures, (NANOARCH 2017), Newport, RI, USA, July 25-26, 2017,IEEE pp.39-44.
Doi : 10.1109/NANOARCH.2017.8053704.

- Sophiane Senni, Tibeau Delobelle, **Odilia Coi** et al. "Embedded systems to high performance computing using STT-MRAM", Design and Test in Europe (DATE 2017), Lausanne, Switzerland, Mars 27-31, 2017, IEEE pp. 536-541.
Doi: 10.23919/DATE.2017.7927046.

Posters:

- **Odilia Coi** et al. "Multi Bit Upset detection and correction based on Non-Volatile C-element", International Electronic Devices Meeting, MRAM poster session, (IEDM 2018), San Francisco, USA, 3-5 December 2018. HAL Id : hal-01982795.

- **Odilia Coi** et al. "Self Robust Non-Volatile C-element for single Event Upset enhanced tolerance", Group de Recherche System on Chip, Systèmes embarqués et Objets Connectés, (GDR 2019) Montpellier France, 19-21 June 2019 (GDR) 2019.

- **Odilia Coi** et al. "Non-Volatile C-element for single Event Upset tolerance", Journées Nationales du Réseau Doctoral en Micro-nanoélectronique , (JNRDM 2019), Montpellier, France, 2-4 June 2019. HAL Id : lirmm-02366116.